



THE UNIVERSITY OF QUEENSLAND  
A U S T R A L I A

**Trajectory Optimisation of a Partially-Reusable  
Rocket-Scramjet-Rocket Small Satellite Launch System**

Sholto O. Forbes-Spyratos

B.Eng. (Mechanical and Aerospace) (Hons. I) & B.Sc. (Physics)

A thesis submitted for the degree of Doctor of Philosophy at  
The University of Queensland in 2018

School of Mechanical Engineering

*Centre for Hypersonics*



---

## **Abstract**

---

## **Declaration by author**

This thesis is composed of my original work, and contains no material previously published or written by another person except where due reference has been made in the text. I have clearly stated the contribution by others to jointly-authored works that I have included in my thesis.

I have clearly stated the contribution of others to my thesis as a whole, including statistical assistance, survey design, data analysis, significant technical procedures, professional editorial advice, and any other original research work used or reported in my thesis. The content of my thesis is the result of work I have carried out since the commencement of my research higher degree candidature and does not include a substantial part of work that has been submitted to qualify for the award of any other degree or diploma in any university or other tertiary institution. I have clearly stated which parts of my thesis, if any, have been submitted to qualify for another award.

I acknowledge that an electronic copy of my thesis must be lodged with the University Library and, subject to the policy and procedures of The University of Queensland, the thesis be made available for research and study in accordance with the Copyright Act 1968 unless a period of embargo has been approved by the Dean of the Graduate School.

I acknowledge that copyright of all material contained in my thesis resides with the copyright holder(s) of that material. Where appropriate I have obtained copyright permission from the copyright holder to reproduce material in this thesis.

---

## Publications during candidature

### Journal papers

Sholto O. Forbes-Spyratos, Michael P. Kearney, Michael K. Smart, and Ingo H. Jahn. “Trajectory Design of a Rocket-Scramjet-Rocket Multi-Stage Launch System”. In: *Journal of Spacecraft and Rockets - Under Consideration* TBD (2018)

### Conference papers

S.O. Forbes-Spyratos, M.P. Kearney, M.K. Smart, and I.H. Jahn. “Trajectory design of a rocket-scramjet-rocket multi-stage launch system”. In: *21st AIAA International Space Planes and Hypersonics Technologies Conference, Hypersonics 2017*. Xiamen, China, 2017. ISBN: 9781624104633

## Publications included in this thesis

This thesis comprises partly of publications, as allowed by University of Queensland Policy PPL 4.60.07. The papers that have been included have all been published in peer reviewed journals at the time of submission.

make this table more compact

Sholto O. Forbes-Spyratos, Michael P. Kearney, Michael K. Smart, and Ingo H. Jahn. “Trajectory Design of a Rocket-Scramjet-Rocket Multi-Stage Launch System”. In: *Journal of Spacecraft and Rockets - Under Consideration* TBD (2018)

Contributor	Contribution
Sholto O. Forbes-Spyratos	Performed simulations (%)
	Analysis of results (%)
	Wrote and edited paper (%)
Ingo H. Jahn	Analysis of results (%)
Michael P. Kearney	Analysis of results (%)
Michael K. Smart	Analysis of results (%)
	Wrote and edited paper (%)

---

## **Contributions by Others to the Thesis**

Except for the contributions by others to publications above, there are no contributions by others to this thesis.

## **Statement of Parts of the Thesis Submitted to Qualify for the Award of Another Degree**

None.

---

## Acknowledgements

---

## **Keywords**

keyword, keyword, keyword, keyword, keyword

## **Australian and New Zealand Standard Research Classification (ANZSRC)**

ANZSRC code: 090107 Hypersonic Propulsion and Hypersonic Aerodynamics, 20%

ANZSRC code: 090106 Flight Dynamics, 20%

ANZSRC code: 090108, Satellite, Space Vehicle and Missile Design and Testing, 20%

ANZSRC code: 090104 Aircraft Performance and Flight Control Systems , 20%

ANZSRC code: 010303 Optimisation , 20%

## **Fields of Research (FoR) Classification**

FoR code: 0901, Aerospace Engineering, 100%

---

# CONTENTS

<b>List of figures</b>	<b>xvi</b>
<b>List of tables</b>	<b>xvii</b>
<b>1 Introduction</b>	<b>1</b>
1.1 Research aims . . . . .	3
1.2 Thesis Outline and Contributions . . . . .	5
<b>2 Literature review</b>	<b>7</b>
2.1 Scramjets . . . . .	7
2.2 Reusable Rocket-Powered Satellite Launch Systems . . . . .	9
2.3 Small Satellite Launchers . . . . .	10
2.4 Airbreathing Access-to-Space Systems . . . . .	14
2.4.1 Small Airbreathing Launchers . . . . .	15
2.5 Airbreathing Launch Vehicle Ascent Trajectories . . . . .	16
2.5.1 Single-Stage Vehicles . . . . .	18
2.5.2 Multi-Stage Vehicles . . . . .	18
2.6 Hypersonic Vehicle Fly-Back Trajectories . . . . .	20
2.7 The University of Queensland's Rocket-Scramjet-Rocket Launch System . . . . .	22
2.7.1 Scramjet Engine Model . . . . .	23
2.7.2 The Trajectory of the SPARTAN . . . . .	24
2.7.3 The Third Stage Rocket . . . . .	25
2.7.4 Exoatmospheric Rocket Engines . . . . .	25
2.8 Optimal Control . . . . .	29
2.8.1 Shooting Methods . . . . .	30

## CONTENTS

---

2.8.2	Collocation Methods . . . . .	31
2.9	Available Optimal Control Solvers . . . . .	34
2.10	Aerodynamic Analysis . . . . .	35
2.10.1	CART3D . . . . .	37
2.10.2	Missile DATCOM . . . . .	38
<b>3</b>	<b>Launch Vehicle Design and Simulation</b>	<b>41</b>
3.1	Second Stage Scramjet . . . . .	44
3.1.1	The SPARTAN Accelerator . . . . .	44
3.1.2	Propulsion . . . . .	45
3.1.3	The Aerodynamics of the SPARTAN . . . . .	48
3.2	First Stage Rocket . . . . .	56
3.2.1	Aerodynamics Including First Stage . . . . .	57
3.3	Third Stage Rocket - Baseline . . . . .	58
3.3.1	Heat Shield Sizing . . . . .	61
3.3.2	Fuel Tank Sizing . . . . .	62
3.3.3	The Aerodynamics of the Third Stage Rocket . . . . .	62
<b>4</b>	<b>LODESTAR</b>	<b>65</b>
4.1	Optimal Control Problem Structure . . . . .	66
4.1.1	GPOPS-2 Example - Brachistochrone Problem . . . . .	68
4.2	Rocket-Scramjet-Rocket Trajectory Optimisation . . . . .	69
4.2.1	Dynamic Model . . . . .	71
4.2.2	Trajectory Connection Points . . . . .	72
4.2.3	III. Second Stage Ascent Trajectory . . . . .	75
4.2.4	IV. Second Stage Return Trajectory . . . . .	76
4.2.5	V. Third Stage Powered Ascent . . . . .	77
4.2.6	VI. Third Stage Unpowered Ascent . . . . .	78
4.2.7	VII. Hohmann Transfer . . . . .	78
4.3	Optimality Conditions . . . . .	79
<b>5</b>	<b>Optimised Ascent Trajectory</b>	<b>83</b>
5.0.1	Optimisation Methodology . . . . .	84
5.1	Current Methodology . . . . .	84
5.2	Optimised Ascent Trajectory Results . . . . .	87
5.2.1	First Stage Evaluation - q=50kpa Second Stage Separation . . . . .	88
5.2.2	Second Stage Evaluation . . . . .	89
5.2.3	Third Stage Evaluation . . . . .	96

<b>6 Optimised Trajectory Including Fly-Back</b>	<b>99</b>
6.1 Combined SPARTAN Ascent-Descent & Third Stage Example . . . . .	100
6.2 Fly-Back Trajectory Analysis . . . . .	103
6.2.1 Optimised Trajectory . . . . .	104
6.2.2 Sensitivity Analysis . . . . .	107
6.2.3 Conclusion . . . . .	107
<b>7 Conclusions</b>	<b>109</b>
7.1 Recommendations for future work . . . . .	109
<b>Library</b>	<b>111</b>
<b>A Trajectory results</b>	<b>123</b>
<b>B CART3D Results</b>	<b>125</b>
B.1 Engine-On Plume Check . . . . .	125
B.2 CART3D Results . . . . .	125



---

## LIST OF FIGURES

1.1	The scramjet-powered second stage of the SPARTAN[9]. . . . .	3
2.1	A simple schematic of a scramjet engine[47]. . . . .	8
2.2	Characteristic performance for airbreathing and rocket engines with Mach number[41]. . . . .	8
2.3	Comparison of Blue Origin and SpaceX partially-reusable launch systems with existing and historic launch systems[70]. . . . .	10
2.4	The trajectory of the Falcon Heavy[88]. . . . .	11
2.5	The trajectory of the Ariane featuring Adeline[126]. . . . .	12
2.6	The airbreathing vehicle flight corridor [113]. . . . .	14
2.7	The SKYLON spaceplane [130]. . . . .	15
2.8	An example of an airbreathing ascent trajectory of the Maglifter RBCC/Rocket launch vehicle[82]. This trajectory shows a constant dynamic pressure section during fanramjet mode[82]. . . . .	17
2.9	. . . . .	18
2.10	Powell . . . . .	18
2.11	. . . . .	19
2.12	Wilhite . . . . .	19
2.13	a) Airbreathing b) Airbreathing/Rocket . . . . .	19
2.14	The trajectory of the launch system developed by Tsuchiya and Mori [129] . . . . .	19
2.15	. . . . .	20
2.16	The trajectory of the launch system developed by Mehta and Bowles [75]. . . . .	20
2.17	The optimised maximum range trajectory of a hypersonic vehicle[17]. . . . .	22
2.18	An early design of the socket-scramjet-rocket launch system incorporating the SPARTAN [54]. . . . .	23
2.19	The C-RESTM10 propulsion database, specific impulse. . . . .	24

## LIST OF FIGURES

---

2.20	The flight trajectory of the SPARTAN . . . . .	26
2.21	The elevons of the SPARTAN[94]. . . . .	27
2.22	The third stage rocket of the rocket-scramjet-rocket launch system[94]. . . . .	27
2.23	A comparison of single shooting and multiple shooting[61]. . . . .	31
2.24	Examples of h and p collocation methods[61]. . . . .	32
2.25	Comparison of optimisation techniques[17]. A hypersonic vehicle is optimised for maximum range. The hp-adaptive method can be observed to have produced the most optimal result. . . . .	33
2.26	The Skylon spaceplane, simulated using CART3D at Mach 12.189, $\alpha = 7.512^\circ$ [74]. Cell distribution produced by mesh adaptation is shown. . . . .	37
2.27	Comparisons of CART3D with experimental data and the FUN3D Navier-Stokes CFD solver. P1, P2 and P3 indicate pressure tap locations. Modified from Sagerman et al.[108]. . . . .	38
3.1	The launch process of the rocket-scramjet-rocket launch system, presented in simplified form. . . . .	42
3.2	The rocket-scramjet-rocket launch system, top view, showing the SPARTAN and first stage. . . . .	43
3.3	The rocket-scramjet-rocket launch system, side view, showing the SPARTAN and fuel tanks, along with the third and first stages. . . . .	44
3.4	The locations of conditions relevant to C-REST engine simulation. . . . .	45
3.5	Flow conditions after the conical shock generated by the vehicle nose cone. Figure a) shows the Mach number, b) shows the pressure ratio, and c) shows the temperature ratio following the conical shock. . . . .	46
3.6	Specific impulse of the CRESTM10 engines with input temperature and Mach number. Available data points are indicated. . . . .	47
3.7	Operable equivalence ratio of the CRESTM10 engines with input temperature and Mach number. Available data points are indicated. . . . .	48
3.8	SPARTAN model showing control surfaces. <i>Dimensions will be included.</i> . . . . .	50
3.9	The forces on the SPARTAN during flight. . . . .	50
3.10	Flap deflection required for trim of the SPARTAN. Negative up. <i>These images will be modified when the final aerodynamics are calculated. The colourmap will be modified to have the same range across figures.</i> . . . . .	52
3.11	Process for generating aerodynamic databases. . . . .	53
3.12	Surface triangulation of the Baseline SPARTAN. <i>This image will be recoloured.</i> . . . . .	54
3.13	Pointwise view of the SPARTAN showing engine outlet boundaries. . . . .	54

3.14 Engine-on CART3D simulation at Mach 7, 6° angle of attack, and 24km altitude. <i>The quality of these images will be improved.</i>	55
3.15 Trimmed aerodynamic coefficients with the C-REST engines powered on. Coefficients correspond to a reference area of 62.77m <sup>2</sup> .	56
3.16 CART3D flow result for the SPARTAN, at Mach 7, 6° angle of attack.	57
3.17 Trimmed aerodynamic Characteristics of the SPARTAN with C-REST engine powered off. Coefficients correspond to a reference area of 62.77m <sup>2</sup> .	58
3.18 Unstarted scramjet engines at mach 3, 2° angle of attack.	59
3.19 CART3D result for the SPARTAN and first stage vehicles at Mach 2, -1° angle of attack.	59
3.20 Aerodynamic characteristics of the SPARTAN including the first stage rocket.	60
3.21 The third stage rocket, showing major internal features. <i>Labels to be added.</i>	60
3.22 Variation in coefficient of thrust with area ratio [122].	61
3.23 Aerodynamic characteristics of the baseline third stage rocket, for a reference area of 0.95m <sup>2</sup> .	64
3.24 Thrust vector force balance.	64
4.1 General work flow of the pseudospectral solver.	66
4.2 The solution to the brachistochrone problem, solved in GPOPS-2[CITATIONXX].	69
4.3 The process of the rocket-scramjet-rocket trajectory optimisation.	70
4.4 The Earth-fixed components of the geodetic rotational coordinate system.	71
4.5 The vehicle-based components of the coordinate system.	72
4.6 Illustration of the segmented launch profile.	73
4.7 The Hohmann transfer manoeuvre.	78
5.1 Payload mass results with variation in rocket stage release point for $v = 2875\text{m/s}$ , heading angle = 1.78 rad and latitude = -0.136 rad.	85
5.2 First stage trajectory, optimised for minimum fuel mass and a release point of 50kPa.	89
5.3 Trajectory path of the 2 <sup>nd</sup> stage SPARTAN vehicle flying at 50kPa constant dynamic pressure, with 1.5° third stage release angle.	89
5.4 Trajectory data for 50kPa constant dynamic pressure trajectory, with 1.5° third stage release angle.	90
5.5 Vehicle performance data for 50kPa constant dynamic pressure trajectory, with 1.5° third stage release angle. Note: Flap deflection is positive down.	90
5.6 Maximum payload trajectory path of the 2 <sup>nd</sup> stage SPARTAN vehicle when limited to 50kPa dynamic pressure.	91
5.7 Trajectory data for 50kpa dynamic pressure limited trajectory.	91
5.8 Vehicle performance data for 50kpa dynamic pressure limited trajectory. Note: Flap deflection is positive down.	92

## LIST OF FIGURES

---

5.9	Comparison of 45kPa / 55kpa dynamic pressure limited trajectory paths for maximum payload to orbit. . . . .	93
5.10	Comparison of trajectory data for 45kPa / 55kpa dynamic pressure limited trajectories. . . . .	94
5.11	Comparison of vehicle performance data for 45kPa / 55kpa dynamic pressure limited trajectories. . . . .	94
5.12	Comparison of trajectory paths for 100% and 110% drag cases for a 50kPa dynamic pressure limited maximum payload trajectory. . . . .	95
5.13	Comparison of $v$ and $I_{sp,net}$ for 100% and 110% drag cases for a 50kPa dynamic pressure limited maximum payload trajectory. . . . .	95
5.14	Third stage rocket trajectory simulated from the end of the 50kPa constant dynamic pressure SPARTAN trajectory, released at an angle of $1.50^\circ$ , velocity of 2905m/s, and altitude of 33.17km. . . . .	96
5.15	Third stage rocket trajectory simulated from the end of the 50kPa dynamic pressure limited maximum payload SPARTAN trajectory, released at an angle of $2.91^\circ$ , velocity of 2881m/s, and altitude of 34.49km. . . . .	97
6.1	The flight path of the SPARTAN ascent. . . . .	100
6.2	Aerodynamic parameters of the SPARTAN ascent. . . . .	101
6.3	Vehicle parameters of the SPARTAN ascent. . . . .	101
6.4	The flight path of the SPARTAN fly-back. . . . .	102
6.5	Vehicle parameters of the SPARTAN fly-back. . . . .	102
6.6	Aerodynamic and propulsion parameters of the SPARTAN fly-back. . . . .	103
6.7	The ground track of the ascent and fly-back of the SPARTAN. . . . .	103
6.8	Ground track of the optimised fly-back of the SPARTAN vehicle. . . . .	104
6.9	Trajectory data for the fly-back of the SPARTAN vehicle. Optimised for minimum fuel usage using LODESTAR. . . . .	105
6.10	Comparison of optimal trajectories with $\pm 10\%$ $C_D$ variance. . . . .	108
6.11	Comparison of optimal trajectories with $\pm 10\%$ $I_{SP}$ variance. . . . .	108
B.1	. . . . .	126
B.2	Mesh generated by CART3D around the SPARTAN and first stage vehicles. . . . .	126
B.3	CART3D flow result for the SPARTAN, at Mach 1.1, $6^\circ$ angle of attack. . . . .	126
B.4	CART3D flow result for the SPARTAN, at Mach 3, $6^\circ$ angle of attack. . . . .	127

---

## LIST OF TABLES

2.1	Summary of small satellite launchers, operational and in development. . . . .	13
2.2	Comparison of upper stage rocket engines, sourced from the Encyclopedia Astronautica reference website[134]. . . . .	28
2.3	Summary of programs capable of pseudospectral optimisation. . . . .	35
3.1	Mass breakdown of the modified SPARTAN vehicle. . . . .	44
3.2	First Stage Engine Properties [CITATIONXX]. . . . .	57
3.3	Third stage heat shield breakdown. . . . .	62
3.4	Third stage fuel distribution. . . . .	63
4.1	Segment coupling conditions for combined trajectory optimisation. . . . .	74
4.2	Optimisation setup of the first stage phase. The other tables in this section will be modified to conform to this one. But I am currently unsure whether this table layout is clear. . . . .	75
5.1	Summary of Simulation Results . . . . .	88



---

---

# CHAPTER 1

---

## INTRODUCTION

In recent years, the space sector has seen a significant shift in the paradigm of space launch system design. The sector has moved towards privatisation, with new and innovative launch systems competing to offer the most cost-efficient and reliable launches. The sector has also seen a split between those who produce large satellite launchers and those who produce small satellite launchers. For large payload launchers, reusability is a major focus in the design of new launch systems, with the purpose of making a launch system cost efficient over multiple launches. For small payload launchers, reusability is more complex than for large launchers, as the additional systems necessary for reusability add a larger fraction of system mass, and require a proportionally larger fuel mass. Consequently, the focus of small launch system design is currently on producing expendable launch systems as cheaply and efficiently as possible, using state of the art technologies such as 3D printing to expedite the process and minimise cost[81]. However, if reusability is able to be successfully integrated into small launch system design, it has the potential to increase the cost efficiency and launch flexibility, potentially opening up the small satellite market significantly.

A potential candidate for integrating reusability into small satellite launch systems is the use of airbreathing engines[63, 116]. Airbreathing engines produce higher specific impulse than rockets, and require far less propellant to be carried on-board a launch vehicle[113]. The higher efficiency and reduced propellant mass of airbreathing vehicles allows the additional mass of the systems necessary for reusability to be mitigated[25]. An airbreathing vehicle can be designed in a similar fashion to a conventional aircraft, with wings, stabilisers and ailerons[111]. A vehicle designed in this fashion has a high lift-to-drag ratio, and good manoeuvrability, allowing for a return flight which uses minimal fuel.

The primary airbreathing engines in consideration for launch vehicles are ramjet and scramjet engines[48]. These engines offer good efficiency and have operational regimes which allow them to effectively accelerate a launch vehicle over a range of Mach numbers. Ramjets and scramjets rely on

the high velocity of the aircraft to compress the flow of air entering the engine before combustion. Ramjets slow the air to subsonic speeds before combustion and are limited to operation at low Mach numbers, whereas scramjets keep the flow supersonic throughout, and operate within the hypersonic regime, above Mach 5. The limited operational regimes of these engines, and the necessity for atmospheric flight, means that a launch system cannot be solely powered by airbreathing engines. Rocket power is necessary for at least the exoatmospheric portion of the trajectory. As a result, the designs of airbreathing launch systems are necessarily partially-airbreathing, usually separated into multiple stages to increase weight efficiency[116]. If a scramjet engine is used, rocket power is also desirable for accelerating scramjet accelerator to minimum operational speed, as the alternative is using turbojets and ramjets sequentially[116], which is weight and cost intensive.

The design of the trajectory of a partially-airbreathing launch system is extremely important to its performance. The airbreathing engines of a ramjet or scramjet-powered stage require high dynamic pressure to operate effectively, and airbreathing stages are generally designed for high lift-to-drag. Conversely, rocket-powered stages produce more thrust at higher altitude, and are generally designed for weight and cost efficiency. For these launch systems, the various stages and engines involved during launch require trade-offs in engine efficiency and thrust generation, stage mass, and vehicle aerodynamics. These factors require the launch trajectory of the system to be thoroughly simulated and optimised, to ensure that the launch vehicle is operating effectively.

Calculating a suitable trajectory for a space launch system is an integral part of the preliminary vehicle and mission design process. A trajectory must be calculated which allows the launch system to achieve its objectives of placing a payload into orbit, while recovering any reusable stages. Ideally, the calculated trajectory will achieve the maximum possible payload-to-orbit, while adhering to the structural, heating and propulsive limitations of the vehicle. Calculating the optimal trajectory profile for a launch system typically requires the use of optimal control theory. Optimal control theory is a general set of techniques which find a control law to maximise a given metric of a system[12, 98]. For a launch vehicle, optimal control allows the best possible payload-to-orbit to be calculated in simulations during design. Optimal control theory allows a trajectory to be calculated in which the flight path of each individual vehicle is considered simultaneously to produce a maximum-payload trajectory[12]. Optimal control is able to produce an optimised trajectory which satisfies the specific structural and flight constraints of the vehicle being simulated, allowing the physical limitations of the vehicle, such as heating and structural loading limits, to be imposed[12]. These constraints also allow any necessary mission conditions to be established, such as reaching orbital velocity and achieving fly-back. An optimal trajectory calculated for multiple launch vehicle stages simultaneously, without predispositions, can offer valuable insights into the performance of a launch vehicle, and drive future design decisions. This concurrent optimisation of multiple stages is particularly important for launch systems incorporating airbreathing engines, where the performance of each stage is significantly different.

This study applies optimal control theory to a three stage rocket-scramjet-rocket launch system being developed by The University of Queensland. The second stage of this system is a scramjet-powered accelerator, designated The SPARTAN[93]. This launch system is designed to be partially reusable, with at least the second stage scramjet vehicle flying back to the initial launch site, as well as possibly the first stage booster, although this is beyond the scope of this study. In previous studies it has been assumed that by maximising the performance of the SPARTAN, that the performance of the launch system is also maximised. The trajectory of the launch system has been designed around the SPARTAN flying at its maximum dynamic pressure, and all other trajectory stages have conformed to this assumption. However, these studies did not consider the interaction between stages, or the fly-back of the SPARTAN. This study will develop trajectory planning tools for partially-airbreathing launch systems, and calculate an optimised launch trajectory for the rocket-scramjet-rocket system incorporating the SPARTAN. This optimised trajectory will be calculated with the aim of producing an optimal trajectory profile which may be applied to any multi-stage rocket-airbreathing-rocket system for delivering small satellites to Earth orbit.



Figure 1.1: The scramjet-powered second stage of the SPARTAN[9].

## 1.1 Research aims

The aim of this work is to design the trajectory of a rocket-scramjet-rocket small satellite launch system. The purpose of this optimised trajectory is to maximise the payload-to-orbit capabilities of the launch system, thereby also maximising the cost efficiency of the system. The optimal trajectory will be utilised to assess the feasibility of return flight, as well as to determine the impact of key vehicle design parameters on the performance of the launch system.

These aims will be achieved through the following objectives:

## CHAPTER 1. INTRODUCTION

---

1. *Develop a detailed design and aerodynamic simulation for a rocket-scramjet-rocket launch system*

For an optimal trajectory to be calculated, a detailed launch system design and robust aerodynamic simulation are required. This design must be representative of a standard rocket-scramjet-rocket launch system for the optimal trajectory results to be generally applicable.

2. *Determine the maximum payload-to-orbit trajectory for the rocket-scramjet-rocket launch system using optimal control, with and without fly-back.*

The trajectory of a multi-stage rocket-scramjet-rocket system is sensitive to a multitude of factors. Optimal control techniques allow a maximum-payload trajectory to be calculated with few assumptions as to the general shape of the trajectory. Optimising the ascent of the launch system ensures that the maximum payload-to-orbit is attained. The inclusion of the fly-back of the scramjet stage in the trajectory optimisation allows the impact of the fly-back to be minimised.

3. *Develop insight into how key design parameters of SPARTAN interact with the optimised trajectory.*

The optimal trajectory shape and maximum payload-to-orbit are dependent on the design of the launch system. Assessing the sensitivity of the optimised trajectory shape and payload-to-orbit to key aerodynamic and propulsive properties allows the relative impacts of various design parameters to be calculated and contrasted.

4. *Establish the effect of the 3rd stage design on overall system performance.*

The relative sizing and geometry of the stages in a launch system can have a large effect on the payload cost efficiency of the system. Optimising the trajectory for multiple configurations shows how the maximum payload-to-orbit varies compared to the proportional size of the expendable stages of the launch system.

## 1.2 Thesis Outline and Contributions

### Chapter 2 - Literature Review

A review of literature related to the various aspects of this study is presented. The theory behind scramjet propulsion is outlined, followed by a background of reusable and small satellite launch systems. A review of the trajectories of partially-airbreathing launch systems is presented, comparing the optimised trajectories of various conceptual vehicles. An overview of optimal control theory is presented, with particular emphasis on the pseudospectral method of optimal control, which is employed within this study. Lastly, an overview of the optimal control and aerodynamic solvers which are used in this study is presented.

### Chapter 3 - Launch Vehicle Baseline Design

The design, aerodynamics and engine models of all three stages are detailed. The SPARTAN scramjet-powered stage is presented first, followed by the first and third stages, due to the external scramjet vehicle design being taken from prior work. The design of each stage is presented, followed by the propulsion model used, and finally the simulated aerodynamic characteristics.

### Chapter 4 - LODESTAR

The method used for the simulation and optimisation of the trajectory is detailed, including the creation of the trajectory analysis program, LODESTAR, which has been created for this study. The specifics of the optimal control methodology used are presented, along with relevant examples. The simulation methodology is detailed, along with the construction of the optimal control simulation. The specific set-up of the optimal control program is detailed for each trajectory stage, specifying the costs and constraints which drive the optimal control solver. Finally, the methods for validating the final solutions are specified.

### Chapter 5 - Optimised Ascent Trajectory

The ascent of the SPARTAN and third stage rocket are optimised using LODESTAR, for maximum payload-to-orbit. The first stage rocket is optimised to the first-second stage separation point, for minimum fuel usage. The optimal trajectory is analysed. It is found that a pull-up at the end of the scramjet stage trajectory significantly improves payload-to-orbit. The sensitivity of the optimal trajectory to variation of key vehicle design parameters is studied. Optimised trajectories are calculated, and the trends in maximised payload-to-orbit and optimal trajectory shape are analysed to study the relative impact of the design parameters of the SPARTAN.

## **Chapter 6 - Optimised Trajectory Including Fly-Back**

The trajectory of the launch system is optimised for maximum payload-to-orbit, including the fly-back of the SPARTAN to its initial launch location. It is found to be necessary to reignite the scramjet engines during the return flight of the SPARTAN to achieve fly-back. The SPARTAN is found to bank during acceleration to lessen the fuel consumed during the return flight. In a similar fashion to Chapter 5, The effects of key vehicle parameters on the optimised trajectory are studied. The sensitivity of the optimised trajectory and payload-to-orbit are analysed, with emphasis on how the fly-back trajectory is affected by the varied vehicle parameters.

## **Chapter 7 - Design and Optimisation of the Third Stage Rocket**

The correlations between key design parameters of the third stage rocket and the optimised trajectory of the launch system are investigated. The design of the third stage rocket is varied, along with corresponding changes to the internal design of the SPARTAN. Optimised trajectories are generated for each design configuration. The trends in optimised payload-to-orbit are analysed, along with the corresponding variations in the optimal trajectory shape, in order to maximise the benefit of the optimised launch trajectory. An optimal design for the third stage rocket is suggested.

## **Conclusions**

The body of this thesis concludes by summarising the most significant findings from this work. Recommendations for future work are made.

---

---

## CHAPTER 2

---

### LITERATURE REVIEW

This chapter examines the relevant literature associated with the different aspects of the work conducted as part of this thesis. A brief overview of the theory behind scramjet engines is presented, followed by surveys of the current state of small satellite and reusable launch systems. Next, various conceptual airbreathing launch systems are presented, along with the trajectories and return flights which have been simulated for these systems, with particular emphasis on whether the trajectories were optimised or not. The SPARTAN scramjet-powered accelerator is detailed, followed by a review of the design of the third stage rocket. The theory behind optimal control methods is presented, followed by a survey into currently available optimal control solvers. Lastly, an overview of various aerodynamic modelling methods with emphasis on applicability to preliminary design is detailed.

## 2.1 Scramjets

A Scramjet, or supersonic combustion ramjet, is an airbreathing engine design which combusts air at supersonic speeds and is capable of high Mach number operation. Across their operating range, scramjets offer much higher specific impulse than rockets, the only other propulsion system capable of operating efficiently at hypersonic speeds[13, 21]. Scramjets compress air without moving parts, using geometry changes within the engine [22], as well as on the forebody of the vehicle to create inlet shocks which provide the compression required for combustion[114]. After combustion, the combustion products are expanded through a thrust nozzle, shown in Figure 2.1. This is similar in operation to a ramjet engine, though a scramjet does not generate a normal shock, allowing supersonic air to enter the combustor. Maintaining supersonic speeds throughout the engine allows scramjets to operate efficiently at Mach numbers of 5 and greater. Scramjets were proposed in the 1940's [23] and found to be capable of positive net thrust in 1993 [86] but have yet to be developed to a level which

would allow for commercial application. Though scramjets are still in-development, the potential advantages which they offer over rockets for certain applications are driving their development in a number of institutions[24].

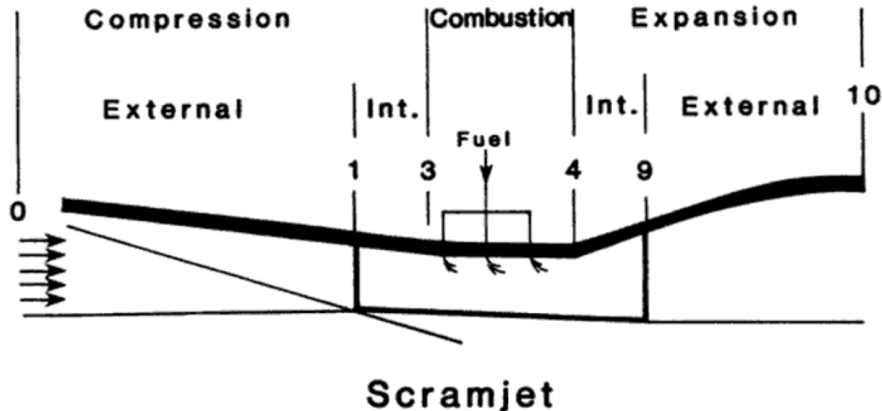


Figure 2.1: A simple schematic of a scramjet engine[47].

Scramjet engines are suitable for a number of applications where sustained flight or acceleration is desired at high Mach numbers. The high efficiency of scramjet engines means that significantly less propellant is used during flight compared to rocket engines, and consequently, that a much smaller fraction of a scramjet-powered vehicle consists of fuel mass[25]. The small fuel mass fraction of a vehicle powered by scramjet engines mitigates the mass of the vehicle systems, allowing features such as wings, control surfaces, landing gear, and passenger transport capabilities to be included in the vehicle design[25].

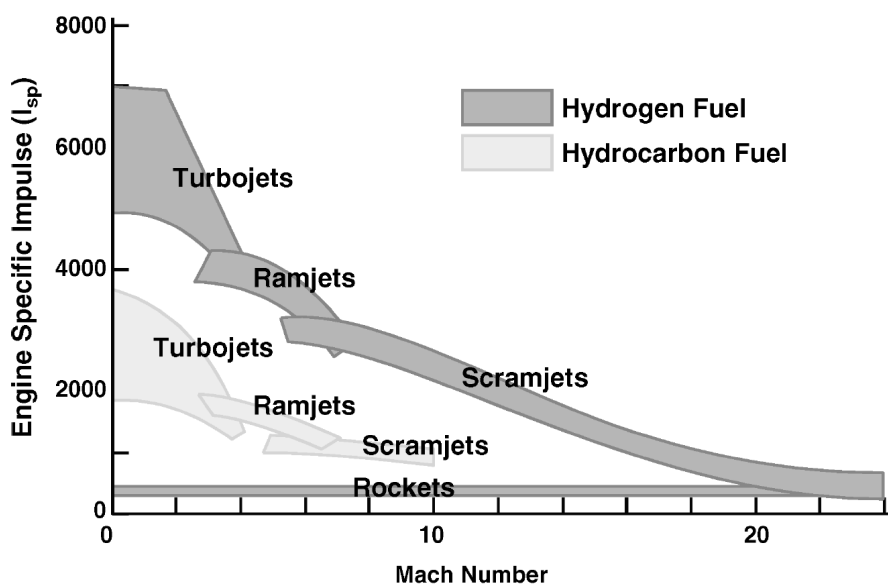


Figure 2.2: Characteristic performance for airbreathing and rocket engines with Mach number[41].

Theoretically, the operable range of scramjets is wide[112]; the specific impulse of a scramjet decreases with velocity, until it is equal to rockets around Mach 19[41], as shown in Figure 2.2. However, in practical designs, the operating range for a scramjet engine is far more limited. For a fixed geometry scramjet, the operable region is constrained by the geometries of the forebody of the vehicle, the inlet, and the combustor of the scramjet engine[113]. The Mach number range of a scramjet engine varies by design, but Mach number ranges of 5-10[91], 7-11[27] and 6-10[15] have been suggested as appropriate operable regimes for scramjet-powered launch vehicles. The operable range of scramjet engines can be improved with mechanisms to vary the geometry of the inlet during flight[26]. However, the systems necessary for variable geometry inlets add weight and complexity to the scramjet engine, and can be detrimental to overall system performance[113].

## 2.2 Reusable Rocket-Powered Satellite Launch Systems

Launch system technologies have progressed rapidly over the last 60 years. From the early vehicles based on intercontinental ballistic missile technology such as the Thor based launch systems, capable of launching 40-400kg to LEO in the 1960s, to the more modern Atlas V based systems of the 2000s capable of launching 9750-18500kg to LEO[62]. The materials, propulsion technology, aerodynamics and guidance algorithms have all improved significantly, enabling rockets to become more efficient, cheaper to produce, and more reliable. As the demand for satellite launches grows, and the cost of development of launchers becomes cheaper, the potential for profiting from space launches increases. This has driven a large portion of the space flight industry to move towards privatisation, with a heavy focus on reusable technology.

Reusable launch technology has been possible for many years, in the form of the space shuttle. However, the space shuttle was weighed down by large launch costs and operational complexity, and was not a commercial success[69]. Recently, reusable launchers have become the focus of many of the largest private launch companies, as reusability becomes more achievable due to technological advances[40, 76]. The SpaceX Falcon 9 and Falcon Heavy have been demonstrated on multiple occasions, landing booster stages successfully, and re-flying reused boosters multiple times[40]. In the near future the Blue Origin New Glenn is planned[40], with potentially the Airbus Adeline to follow (to be used on the Ariane 6)[4]. The Falcon and New Glenn rockets are shown in Figure 2.3, and the trajectories of the Falcon Heavy and Adeline are shown in Figures 2.4 and 2.5.

The aim of reusing launch vehicles is to reduce the cost-over-time of the reused components drastically, which subsequently allows the cost of individual launches to be reduced[99]. Reducing costs lowers the barrier of entry for space launches, potentially improving the diversity of space-based enterprises. Reusing launch system components also allows faster turnaround times for launches, as refurbishment of stages is much faster than manufacturing stages from scratch. Reduced turnaround times are key for improving mission scheduling, allowing satellites to be launched sooner, on a more

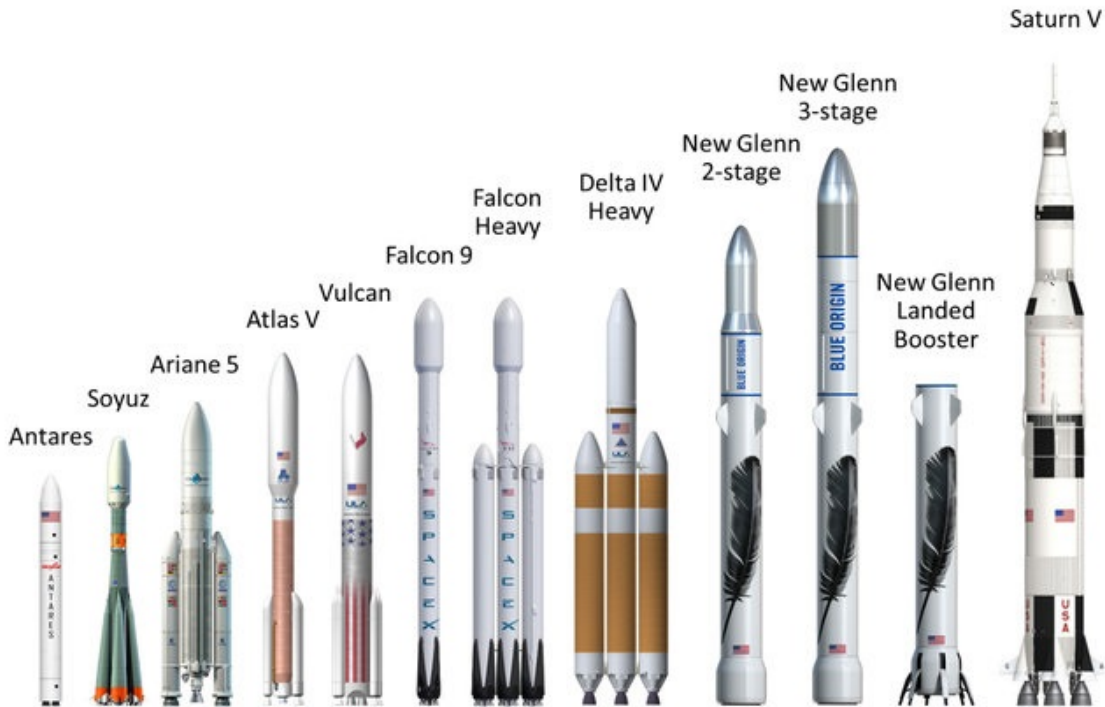


Figure 2.3: Comparison of Blue Origin and SpaceX partially-reusable launch systems with existing and historic launch systems[70].

flexible time frame.

For a launch vehicle to be reusable, it must necessarily have the ability to come back to Earth safely, without damage to major system components. This return flight requires the addition of system components which allow the reusable stage to fly to a specified landing point. Control surfaces[18], structural components[109], additional fuel[109], and in the case of the Adeline, additional engines[4], must be incorporated within a reusable launch vehicle design. The additional weight that these components contribute further increases the fuel and structural mass necessary to initially accelerate the reusable stage. The impact of reusability on the mass and cost of the vehicle is minimised when the velocity at the initiation of the return trajectory is decreased. Because of this mass increase on any stage which is to be designed to be reusable, most current reusable launch vehicle designs include only reusable first stages, with later stages being expendable.

## 2.3 Small Satellite Launchers

The vast improvements in computational technologies in recent years have allowed satellites to decrease in size and cost to a large degree. These factors have lowered the barrier of entry into small satellite manufacturing significantly, driving a surge in the demand for small satellite launches. Many private and public companies are currently developing small satellite launchers which will allow small

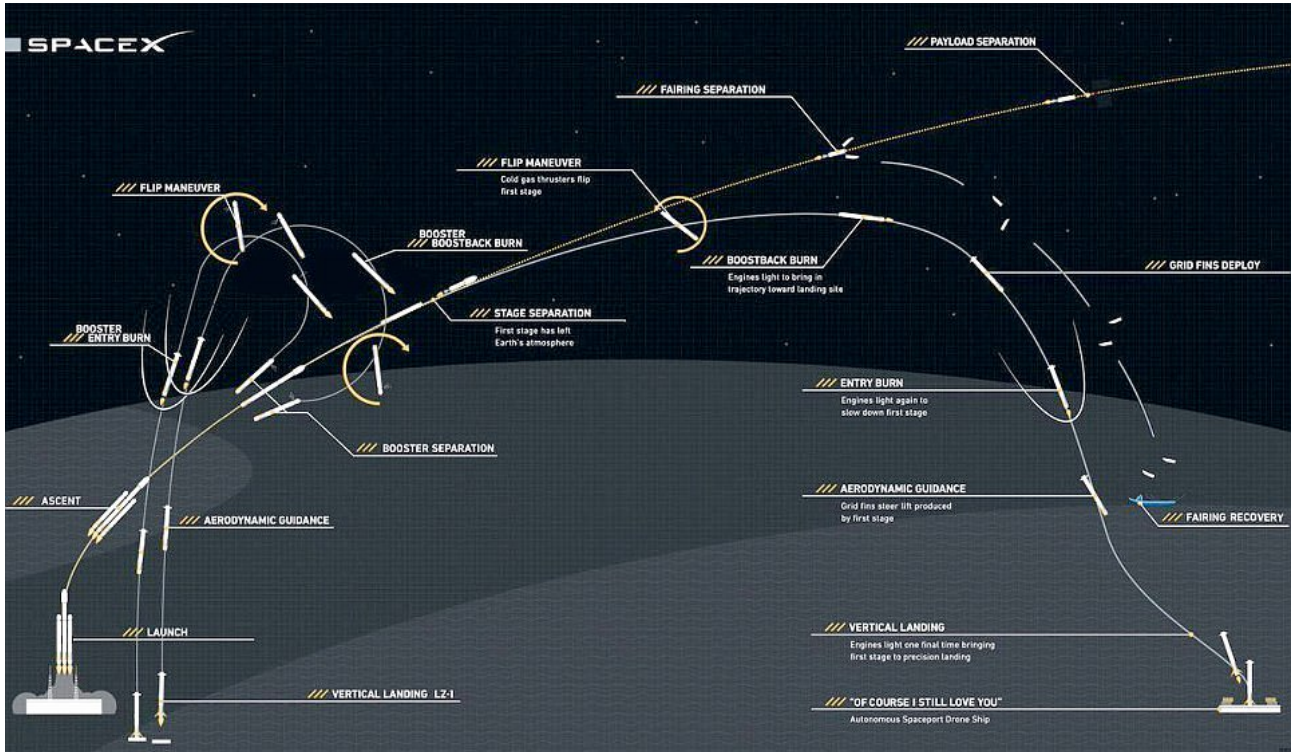


Figure 2.4: The trajectory of the Falcon Heavy[88].

satellites to be launched into bespoke orbits on schedules determined by the customer. A summary of the small satellite launchers currently in active development is shown in Table 2.1. Many of these launchers are projected to be available within the next few years, and will offer cost-per-kg comparable to piggybacking on larger launches.

The majority of the small satellite launchers in development are expendable[81]. These expendable small satellite launch systems aim to reduce costs by creating a launch system which is as cost-efficient as possible to produce and launch[81]. This generally entails making use of conventional, well-tested designs, combined with state of the art manufacturing techniques, such as 3-D printing[43, 81]. This method allows for rapid development, although it has an intrinsic cost limit due to the requirement of manufacturing a new launch system for each launch.

Reusable small satellite launchers have higher initial costs-per-vehicle, but also have the potential for large advantages in the long term[94]. Reusable small satellite launchers have the potential for lower cost-per-launch than expendable systems, with increased launch flexibility[94]. One of the most promising methods of reusability for small launchers is the addition of airbreathing engines[117].

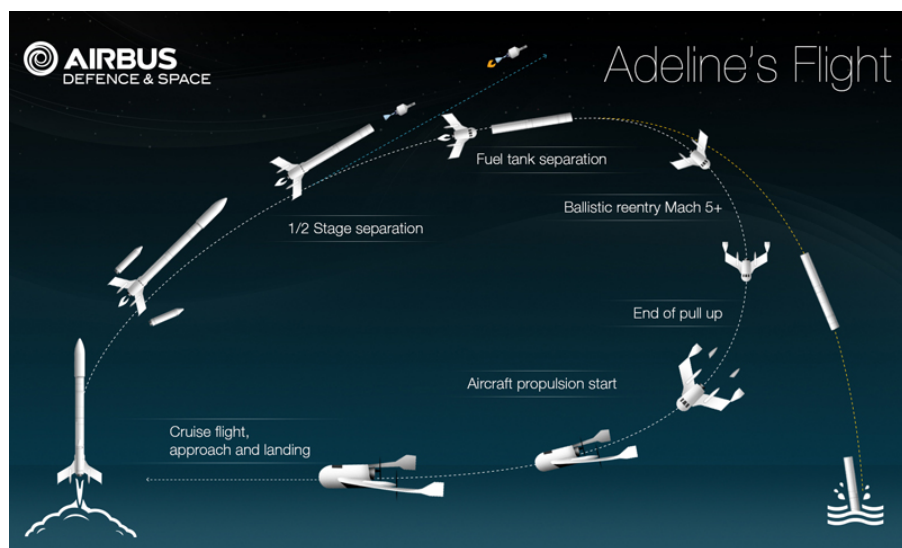


Figure 2.5: The trajectory of the Ariane featuring Adeline[126].

<b>Launcher</b>	<b>Company</b>	<b>Country</b>	<b>Payload Capacity</b>	<b>Cost/Kg (USD)</b>	<b>Availability</b>	<b>Stages &amp; Propulsion</b>	<b>Reusability</b>
Electron [102]	RocketLab	NZ/USA	150Kg to SSO	\$32,600	Available	Rocket-rocket	No
Lynx [2]	XCOR	USA	-	-	-	rocket-rocket	First stage
LauncherOne [132]	Virgin Orbit	UK	300kg to SSO	\$33,000	-	Aircraft-rocket-rocket	Aircraft
Bloostar [139]	Zero2Infinity	Spain	100kg to SSO	\$40,000	-	Balloon-rocket-rocket-rocket	No
XS-1 [84]	Boeing	USA	-	-	-	-	First Stage
Eris [43]	Gilmour Space Technologies	Aus/SG	380kg to LEO	\$23,000-38,000	Q4 2020		No
Black Arrow 2 [51]	Horizon	UK	350kg to SSO	-	2019	Rocket-rocket	No
Haas 2CA [7]	ARCA	USA	100Kg to LEO	\$10,000	2018	Rocket	No
Intrepid-1 [103]	Rocket Crafters	USA	376kg to SSO	\$23,936	Q1 2019	Rocket-rocket	No
KZ-1A [67]	CASIC	China	250kg to SSO	-	-	Rocket-rocket	No
500R [83]	Orbital Access	UK	500kg to SSO	-	-	Aircraft-Rocket	Fully Reusable
Vector-H [131]	Vector Space Systems	USA	160kg to LEO	\$21,875	2018	rocket-rocket-(third rocket optional)	No
SMILE [68]	NLR	EU	50kg	<\$50,000	-	-	-

Table 2.1: Summary of small satellite launchers, operational and in development.

## 2.4 Airbreathing Access-to-Space Systems

The addition of airbreathing stages to a satellite launch system to allow for partial or full reusability of a launch system has been investigated for a number of years by multiple institutions[15, 45, 75, 89, 94, 101, 128–130, 136, 138]. The reduced fuel usage of airbreathing engines allows for the inclusion of systems which enable fly-back and landing of the stage in a similar manner to a conventional aircraft, potentially offering multi-launch re-use with increased launch flexibility and decreased costs[94]. However, the addition of airbreathing engines to a launch system introduces significant design challenges, and no airbreathing access to space systems have yet been developed.

The technological challenges present for an airbreathing launch system stem from the inherent limitations of jet engines. Turbojets, ramjets and scramjets all operate across different Mach number regimes, and require atmospheric flight to operate[117]. This means that within an airbreathing access-to-space system, a combination of various airbreathing engines and/or rockets must be used during launch. Figure 2.6 shows the operating corridor for an example launch system using turbojet, scramjet, and rocket engines, indicating the point at which engine transition occurs, as well as the lower dynamic pressure limit on engine operation and the upper dynamic pressure limit on the aircraft structure. This operational corridor imposes unique constraints on the design of airbreathing launch systems and their trajectories. An airbreathing access to space system must be capable of resisting high structural and thermal loads, as well as being able to sustain atmospheric flight for long periods, necessitating a high lift-to-drag ratio.

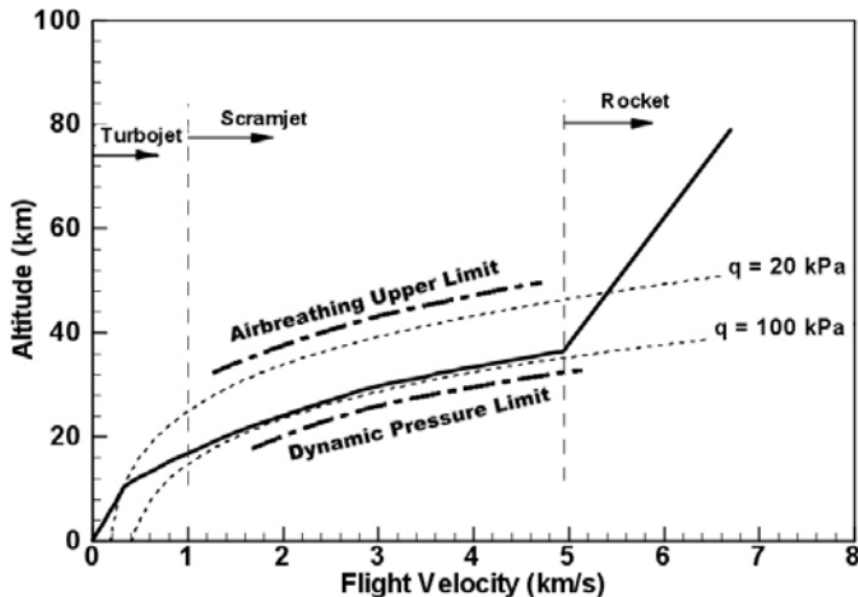


Figure 2.6: The airbreathing vehicle flight corridor [113].

Airbreathing access-to-space systems have been investigated in various forms including; single stage[15, 89, 101, 128, 130, 136, 138], dual stage [45, 75, 129] and tri stage [94] designs. A single

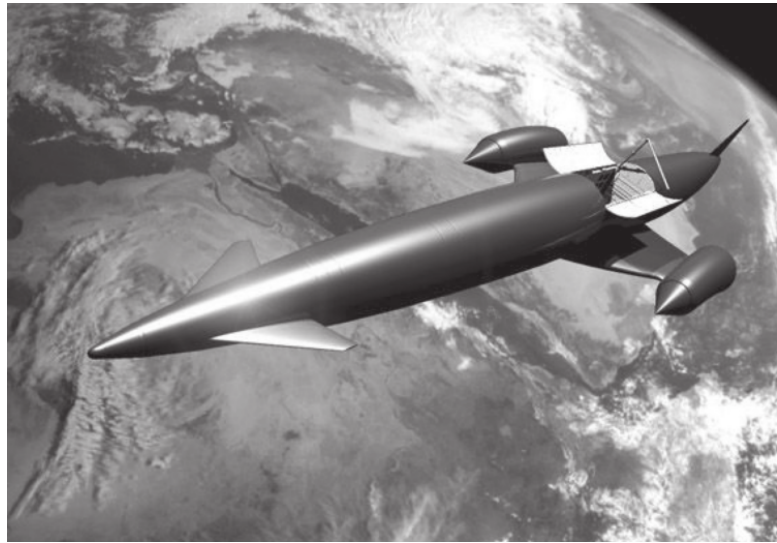


Figure 2.7: The SKYLON spaceplane [130].

stage design has the advantage of being fully contained within one vehicle, which is convenient for reusability and return trajectories however it has been suggested by Smart & Tetlow [117] that these designs suffer from severe limitations as they must contain multiple engines which add mass at later stages of the trajectory and decrease the efficiency of the vehicle. Smart & Tetlow suggest that multistage systems offer significant improvements in payload mass fractions, and have the advantage of using airbreathing stages only within their operable range. Dual stage designs have been investigated in some detail using the 'spaceplane' concept by Mehta & Bowles [75] using life cycle cost analysis in order to take flexibility and reusability into account. Mehta & Bowles conclude that a two stage design is the optimal configuration for reusable hypersonic space access systems, however this study is only based on comparison with single stage to orbit systems, and it is more useful to consider their conclusions as an endorsement of multi stage airbreathing designs in general. They find that multi stage vehicles have higher potential for payload than single stage to orbit (SSTO) systems and have less propellant requirements, partly due to a greater atmospheric cruise capability.

### 2.4.1 Small Airbreathing Launchers

The use of airbreathing engines has particular applicability to small launch systems. As discussed in section 2.3, incorporating reusability into rocket-powered small satellite launchers is complex, due to the high mass fraction of the systems necessary for re-use at small scales. The use of airbreathing engines may allow a small launch system to incorporate reusable elements without excessive mass penalties. Smart & Tetlow[117] have found that the addition of a scramjet-powered stage may enable the development of a partially reusable small satellite launch system in the near future. Simulations carried out for three stage systems utilising scramjet and rocket engines for small payload delivery show favourable payload mass fractions with a reusable scramjet stage [117]. Scramjet

powered vehicles may also offer the ability to put small payloads into orbit with greatly increased flexibility and launch window when compared to similarly sized rocket systems. This has been assessed in a study by Flaherty[37] comparing the United States Air Force's Reusable Military Launch System all-rocket launch vehicle RMLS102 against the Alliant Techsystems rocket/scramjet launch system ATK-RBCC. These vehicles are similarly sized and comparisons were made for payloads launched to rendezvous with satellites in randomly generated orbits[37]. These vehicles were compared using the range of orbital trajectories that each vehicle was able to rendezvous with within one day, determined by launch vehicle range[37]. The vehicles were compared by their ability to reach a range of trajectories intercept locations in limited time, and the ATK-RBCC vehicle was found to be able to cover at least 1.7 times area of the rocket-powered vehicle[37], in a large part due to the airbreathing vehicle's ability to fly fuel efficiently over long distances. This means in general that a partially scramjet powered accelerator is able to fulfil the specific delivery needs of small payloads over a wider range of orbits within smaller time periods when compared to a fully rocket powered accelerator. This can be advantageous for time critical and orbit dependant payloads which have specific mission requirements to be met.

## **2.5 Airbreathing Launch Vehicle Ascent Trajectories**

The trajectory of an airbreathing launch vehicle is more complex than that of a fully rocket-powered launch system. A airbreathing launch system trajectory must be designed around a number of factors:

- The requirement for the airbreathing stages to fly in-atmosphere
- The variable efficiency of the airbreathing engines
- The relative efficiency of the different types of engines within the system
- The aerodynamic performance of each vehicle or engine-mode of the system
- The structural limitations of the system

A simple way to design the trajectory of an airbreathing launch system is to constrain the flight of the high speed airbreathing section to a constant dynamic pressure[59, 82, 92, 96, 138]. Constant dynamic pressure trajectories can be advantageous for an airbreathing accelerator due to the trade-off between structural loading and engine performance[82]. As dynamic pressure increases so does the structural loading on the vehicle, however the performance of a ramjet or scramjet engine is directly reliant on dynamic pressure[82]. A constant dynamic pressure trajectory is viewed as being an acceptable compromise between these two factors. Figure 2.8 shows an example of a constant dynamic pressure trajectory flown by an airbreathing vehicle.

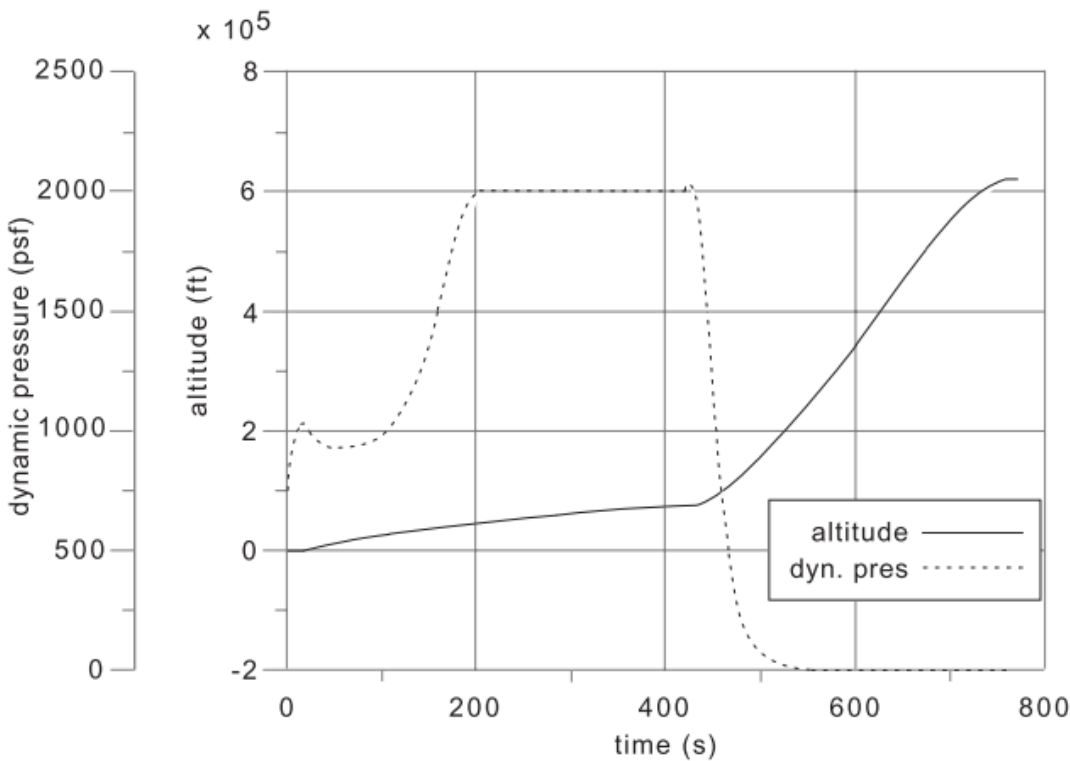


Figure 2.8: An example of an airbreathing ascent trajectory of the Maglifter RBCC/Rocket launch vehicle[82]. This trajectory shows a constant dynamic pressure section during fan-ramjet mode[82].

Although a constant dynamic pressure trajectory is likely to produce high efficiency flight for the high speed airbreathing portion of an ascent trajectory, there are a variety of factors that must be considered in designing the trajectory of a launch system. For example, a constant dynamic pressure flight may produce suboptimal conditions for the switch from airbreathing engines to rocket power for exoatmospheric flight. For a constant dynamic pressure trajectory the transition to rocket power will occur at a very low trajectory angle and altitude[94]. It may be more optimal overall for the vehicle to fly at less than maximum dynamic pressure for a time during airbreathing engine operation, allowing the trajectory angle and altitude to be raised before the rocket engines are powered-on, increasing the efficiency of the rocket engines and reducing the dynamic pressure experienced by the rocket stage[75, 129, 136]. The consideration of all stages and propulsion methods when designing the trajectory of a launch vehicle can produce a more optimal trajectory, which maximises the performance of the launch system, eg. increasing payload-to-orbit, or increasing the range of orbits attainable by the launch vehicle.

### 2.5.1 Single-Stage Vehicles

Optimal trajectories have previously been developed for launch systems integrating airbreathing and rocket propulsion within single-stage-to-orbit (SSTO) vehicles[15, 72, 87, 89, 101, 128, 138]. These optimal trajectory studies found unanimously that a pull-up manoeuvre before the end of the airbreathing engine cut-off was the optimal flight path for the SSTO airbreathing-rocket vehicles being investigated. A pull-up was found to be optimal for vehicles where the rocket engines are not ignited until circularization altitude [72, 89], vehicles where the rocket engine is ignited immediately after airbreathing engine cut-off [87, 101, 128] as well as for vehicles which operate in combined scramjet-rocket mode[15, 138]. For SSTO vehicles a pull-up manoeuvre is a simple trade-off between the altitude at airbreathing engine cut-off and the velocity achievable at cut-off. Due to the entire vehicle being lifted into orbit, this becomes a relatively simple problem of engine efficiency. The airbreathing engine is used for its high efficiency, until the dynamic pressure drops below the operable limit of the airbreathing engine, or until the thrust provided by the airbreathing engine is significantly counteracted by the effects of drag and gravity.

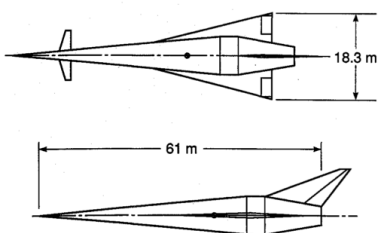


Figure 2.9

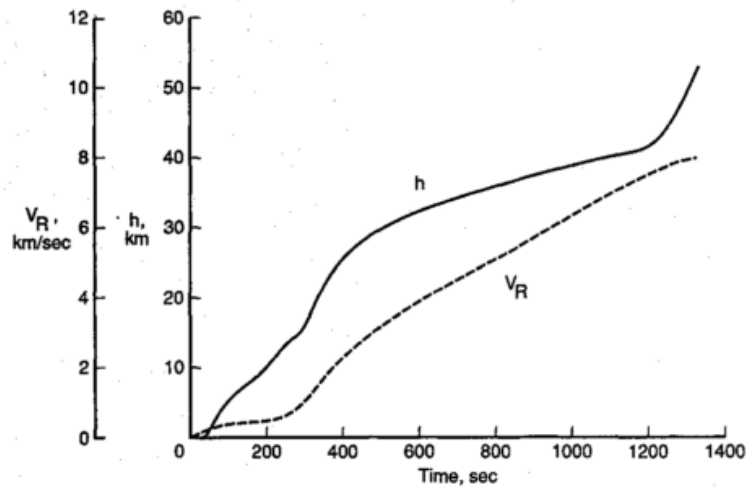


Figure 2.10: Powell

### 2.5.2 Multi-Stage Vehicles

For a multi-stage to orbit vehicle, calculating the optimal trajectory for maximum payload flight is significantly more difficult. A multi-stage vehicle has one or more stage transition points, where the vehicle separates a component which is discarded or reused later, and does not continue to orbit. At a stage transition point there is a large change in the mass and aerodynamics of the launch system. This change in flight dynamics makes finding the optimal stage transition point more complicated. To find the optimal separation point there is a trade-off between:

- The high efficiency of the scramjet engines

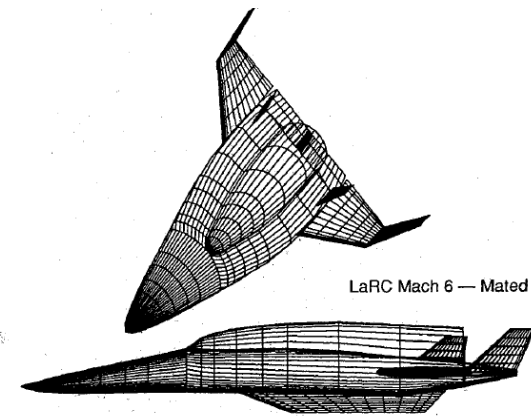


Figure 2.11

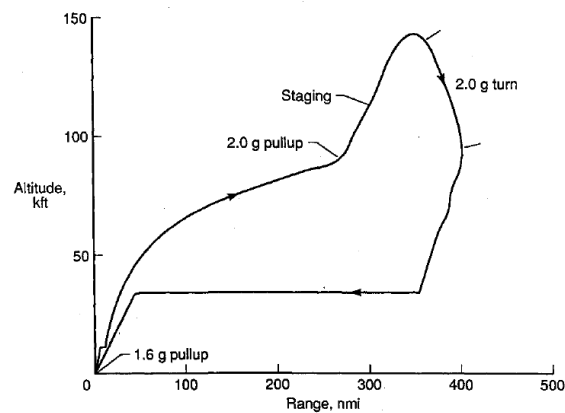


Figure 2.12: Wilhite

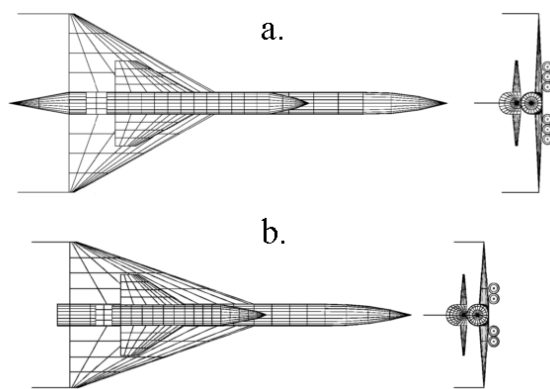


Figure 2.13: a) Airbreathing b) Airbreath-

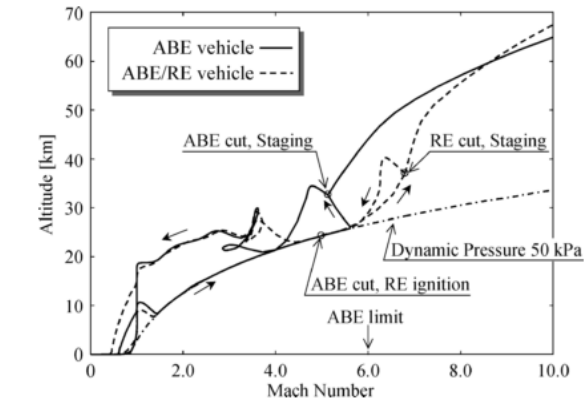


Figure 2.14: The trajectory of the launch system developed by Tsuchiya and Mori [129]

- The thrust produced by the scramjet engines
- The potential thrust of the rocket engines
- The energy necessary to increase the altitude of the scramjet stage
- The aerodynamic efficiency when performing the required direction change

All of these factors must be considered in order to generate an optimal trajectory.

There has been a number of studies which have identified a pull-up manoeuvre as being advantageous for a multi-stage system [75, 129, 136]. However, in these studies a pull-up manoeuvre has been specified in order to decrease the dynamic pressure of the vehicle at airbreathing-rocket stage separation. In the studies by Tsuchiya et al.[129] and Wilhite et al.[136], decreased dynamic pressure is necessary for the successful operation of the orbital rocket stages, of the systems under investigation. In these studies the airbreathing stages pull-up to the maximum allowable dynamic pressure for the rocket-powered orbital stages. When the orbital stages are able to operate, stage separation



Figure 2.15

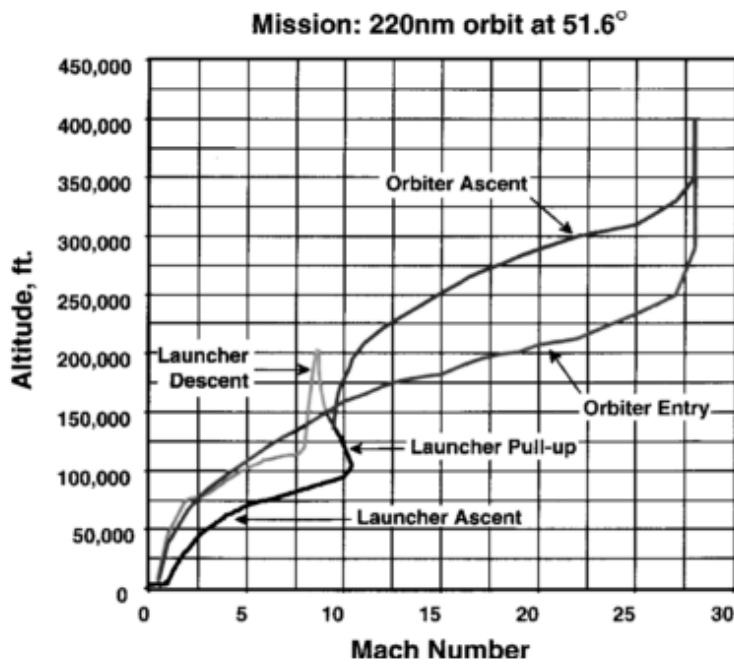


Figure 2.16: The trajectory of the launch system developed by Mehta and Bowles [75].

occurs. These pull-up manoeuvres demonstrate the advantages of a pull-up for the operation of the orbital stages, allowing the aerodynamic and thermal loading on the vehicle to be reduced. However these pull-up manoeuvres are not performed as part of optimal trajectories, instead they are designed to ensure that the performance constraints of the systems are met. Mehta & Bowles [75] prescribe a 2g pull-up at flight conditions of Mach 10, 95000 ft for an airbreathing stage in order to "lower dynamic pressures and to achieve the optimal launching flight path angle for the orbiter vehicle". This indicates that a pull-up manoeuvre before airbreathing-rocket transition is considered the optimal trajectory, however this study does not optimise the shape or magnitude of the pull-up manoeuvre, only considering the increased performance of the rocket vehicle.

## 2.6 Hypersonic Vehicle Fly-Back Trajectories

The fly-back of an airbreathing launch vehicle is a crucial component of the trajectory. The ability to land a reusable launch vehicle safely in the intended location is a key requirement, and if this fly-back can transport the launch vehicle back to the initial launch location, then transport costs and turnaround times can be significantly reduced.

There are three main methods that have been studied for potential hypersonic vehicle return; glide-back, cruise-back and boost-back. Glide-back involves the hypersonic vehicle returning to base and landing entirely using its aerodynamics. This requires sufficient lift to sustain the hypersonic vehicle

over the entire return range, as well as the controllability to land the hypersonic vehicle in level flight. For a hypersonic trajectory a fully glide-back return flight is most likely unobtainable. This is due to the large downrange distance flown, and the large initial velocity at the beginning of the fly-back trajectory, when the vehicle is oriented away from the landing site. Multiple studies have investigated the maximum staging velocity allowable for the glide-back flight of a booster. In these studies, the maximum separation velocity for glide-back to be feasible has been found to be between Mach 3-4 at 30km-120km downrange distance, with higher initial velocities or longer downrange distances requiring fly-back under power[49, 123].

Cruise-back involves the inclusion of subsonic engines, which are used to power the fly-back of the hypersonic vehicle until landing similar to a conventional aircraft. These engines may be included solely for the fly-back[49], or used in the acceleration phase for low velocity acceleration[75, 123, 136]. The addition of subsonic engines powering a constant velocity cruise-back phase allows the accelerator to return to base with a similar trajectory to that of traditional aircraft, allowing the velocity and altitude of the accelerator to be precisely controlled. However, the addition of subsonic engines necessary for cruise-back increases the mass of the vehicle significantly, leading to decreased mass efficiency and increased design complexity[49].

A preferable mode of powered fly-back is to use the existing hypersonic airbreathing engines during the return trajectory in a boost-back trajectory. Using the existing airbreathing engines allows for range to be added to a return trajectory, without the inclusion of additional engines. The hypersonic airbreathing engines can be operated at appropriate times during the fly-back, when they will be most impactful on the return trajectory range. However, the hypersonic airbreathing engines may only be used within their operating region, and vary in thrust and efficiency dependent on flight conditions. Hypersonic airbreathing engines have maximum efficiency at low Mach numbers[94], with the thrust produced depending on the dynamic pressure and inlet conditions, which vary with the trajectory path and angle of attack of the vehicle. This added complexity requires the use of trajectory optimisation methods to find the most efficient flight path for return to the launch site, and to ensure that the return of the vehicle under its own power is viable.

The possibility of an airbreathing vehicle reigniting high speed airbreathing engines for short periods has been investigated by Tsuchiya and Mori [129]. Tsuchiya and Mori investigate two conceptual launch vehicles; a vehicle powered solely by airbreathing propulsion returning after separation of an orbital stage at Mach 5.1, and an airbreathing/rocket vehicle returning after a separation at Mach 6.8[129]. Both vehicles use the high speed airbreathing engines during return flight. The optimal launch and return trajectories for these vehicles are shown in Figure 2.14. Both vehicles ignite the airbreathing engines at around Mach 3.5 for several tens of seconds to extend the range of the fly-back manoeuvres. After this, the vehicles descend and land at the launch site. These boosters fly to a downrange distance of 600-625km from the launch site, and less than 5% of the vehicles initial propellant was required to return the vehicles to the initial launch sites[129].

If powered fly-back is necessary, the additional fuel weight used during this phase can negatively impact on the potential performance of a launch system. Optimising the fly-back trajectory of the reusable stages of a launch vehicle can decrease the amount of fuel used, and minimise the impact of the return phase. The problem of optimising the fly-back of a launch vehicle for minimum fuel is analogous to maximising the range possible on a small amount of fuel, with manoeuvring. The maximum range trajectory of a hypersonic vehicle operating at high altitudes has been shown to be a 'skipping' trajectory, where the altitude of the vehicle is repeatedly raised and lowered[17, 29, 77, 127]. A skipping trajectory has been shown to be range optimal for hypersonic vehicles able to skip out of the atmosphere [77], as well as vehicles flying entirely within the atmosphere[29, 77, 123, 127]. A skipping trajectory has also been shown to be optimal for an airbreathing hypersonic vehicle thrusting throughout the trajectory[17]. This optimised trajectory is shown in Figure 2.17. The range optimal operation of the scramjet engine is shown to be repeated ignitions at the trough of each skip[17]. The scramjets are ignited as the vehicle climbs after the trough, as the Mach number decreases to the minimum operable conditions of the scramjet engines[17]. Minimising the Mach number during operation in this way maximises the efficiency of the scramjet engines[17].

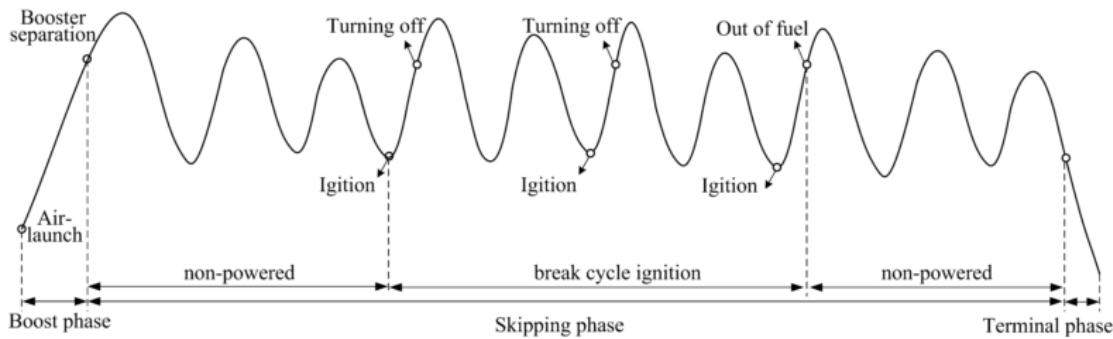


Figure 2.17: The optimised maximum range trajectory of a hypersonic vehicle[17].

## 2.7 The University of Queensland's Rocket-Scramjet-Rocket Launch System

The three stage, partially reusable, access to space system under development at The University of Queensland utilises the SPARTAN[54] scramjet powered vehicle as the reusable second stage, shown in Figure 2.18. This system is considered in this study as a representative model for three stage, air-breathing access to space system designs. This launch system is designed for small payload deliveries to orbit and will in the future utilise a fly-back rocket booster to accelerate the SPARTAN stage to minimum Mach number required for stable burn, at which point separation occurs and the second stage uses a scramjet engine to accelerate to between approximately Mach 5-9. The first and second

## 2.7. THE UNIVERSITY OF QUEENSLAND'S ROCKET-SCRAMJET-ROCKET LAUNCH SYSTEM

stages are to be reusable, the first stage via conversion into a propeller powered drone, and the second stage through either a glide or extra scramjet powered flight to a suitable landing site. The third stage

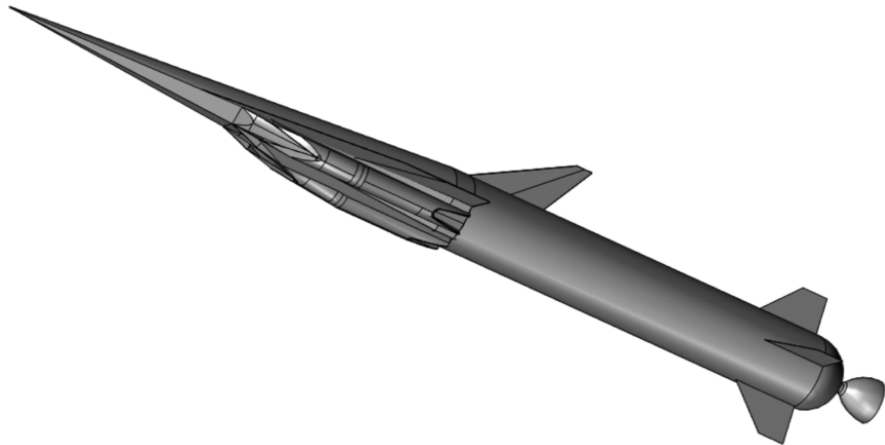


Figure 2.18: An early design of the socket-scramjet-rocket launch system incorporating the SPARTAN [54].

will be a disposable rocket stage, which will then deliver the payload to orbit, exiting the atmosphere and performing a Hohmann transfer. Preliminary designs of the SPARTAN have been completed, with the shape of the SPARTAN optimised for payload delivery to heliosynchronous orbit. Studies have indicated that the expendable third stage makes up only 8.8% of the mass of the launch system, and that if the SPARTAN and first stage rockets are able to be reused, approximately 90% of the launch system mass would be reusable[94].

### 2.7.1 Scramjet Engine Model

To deliver a payload to orbit, the SPARTAN uses four Rectangular-to-Elliptical Shape Transition (REST) scramjet engines, with inlets configured to allow installation on a conical forebody (C-REST). The C-REST engines which the SPARTAN uses have been configured to fly between Mach 5 and 10, this type of engine is known as a C-RESTM10 engine[94]. The REST engine has been shown experimentally to operate successfully at off design conditions by Smart & Ruf[115].

A C-RESTM10 propulsion database has been used in previous studies to model the scramjet engines of the SPARTAN[94]. This database has been created through separate modelling of the compression within the inlet, combustion within the combustor, and expansion through the internal nozzle[90]. The inlet compression was modelled by performance curved based on a set of CFD solutions[90]. These performance curves were used to obtain the flow conditions at the end of the inlet. The combustor was modelled using quasi-one-dimentional cycle analysis, assuming a combustion efficiency of 80%[90]. Lastly, the properties at the end of the combustor were expanded assuming a nozzle efficiency of 90%[90]. The C-RESTM10 is designed for operation at  $M_0 = 10$ , and the con-

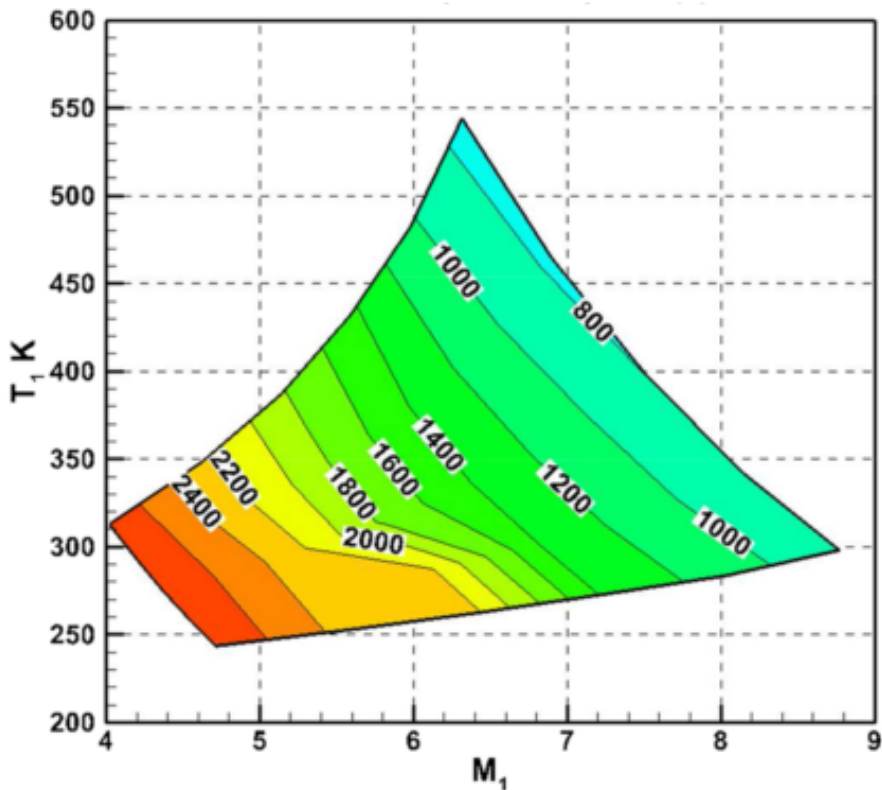


Figure 2.19: The C-RESTM10 propulsion database, specific impulse.

traction ratio and combustor divergence are not optimal for operation at low Mach numbers. At low Mach numbers, an equivalence ratio of 1 may cause the flow to choke and unstart. Consequently, an equivalence ratio of less than 1 was set at low Mach numbers, in order to avoid unstart[90]. At these Mach numbers, the C-REST engines are operating in dual-mode[90].

### 2.7.2 The Trajectory of the SPARTAN

To date, studies of the SPARTAN have assumed a constant dynamic pressure trajectory[94]. Past studies of the SPARTAN vehicle have assumed that a fly-back to launch site is possible after third stage separation[94]. However, this fly-back has not yet been simulated.

Figure 2.20 shows the trajectory of the SPARTAN, simulated in three degrees of freedom to fly close to a constant 50kPa dynamic pressure, using a pole-placement angle of attack controller[94]. The ascent trajectory of the SPARTAN begins at Mach 5.1, and terminates at Mach 9.46, when the hydrogen fuel is exhausted[94]. The net specific impulse of the SPARTAN varies from 1694s at the beginning of the trajectory, to 377s by the time the fuel is depleted[94]. This significant decrease in efficiency means that by the end of the trajectory, the net efficiency of the SPARTAN is approximately that of a rocket[94].

The SPARTAN is trimmed throughout the trajectory by ailerons on the wing, shown in Figure

## 2.7. THE UNIVERSITY OF QUEENSLAND'S ROCKET-SCRAMJET-ROCKET LAUNCH SYSTEM

---

[2.21](#). These elevons were sized through variation of the width,  $b_E$ , to have an area equal to 15% of the area of the wing, and to have a cord length,  $c_E$ , of 15% of the cord length of the wing[94]. Over the flight of the SPARTAN, the flap deflection changes from  $-0.8^\circ$  to  $3.0^\circ$ [94]. The drag contribution of the flap varies from 1.2% to 3.5%, and the lift contribution from -4.0% to 4.2%[94].

This trajectory enables delivery of a 307.1kg payload to low earth orbit[94]. This is a payload mass fraction of 1.17%, which compares well with existing expendable launch systems of similar size, with the advantage of being designed for reusability[94]. This trajectory was designed around the SPARTAN flying a constant dynamic pressure trajectory, with the first and third stage trajectories confirming to this constraint. It has been suggested that for the design of this launch system to be improved, a an optimised trajectory is necessary[94].

### 2.7.3 The Third Stage Rocket

The third stage rocket of the rocket-scramjet-rocket launch system consists of a rocket motor, fuel tanks, structure, payload and a thermal protection system[94], shown in Figure 2.22. The third stage rocket separates from the SPARTAN at the end of its trajectory, and performs a pull-up manoeuvre to exit the atmosphere. Once the density of the atmosphere is low enough, the thermal protection system separated from the vehicle for mass efficiency, and once exoatmospheric, the third stage performs a Hohmann transfer to reach the desired orbit. The third stage has to this point been designed to be powered by the Pratt & Whitney RL-10-3A[94], and has exhibited good performance when powered by this engine. However, the RL-10-3A is a pump-fed engine, and is likely to be prohibitively expensive for a small launch system.

### 2.7.4 Exoatmospheric Rocket Engines

The third stage requires a rocket engine with sufficient thrust to accelerate out of the atmosphere, and a diameter small enough to allow the rocket to fit within the fuselage of the SPARTAN. The major factors when choosing a rocket engine are efficiency and thrust-to-weight ratio, as well as cost. It is desirable to use a rocket engine which has already been developed and flight tested, to reduce the costs and potential complications of engine development. Table 2.2 shows a comparison study of small sized upper stage rocket engines which are currently in use, or have been used, for commercial space flight. The cost of these engines is not generally published, however, pressure fed engines cost significantly less than pump-fed engines, due to the cost of the turbopump and the associated complexity of a pump-fed system.

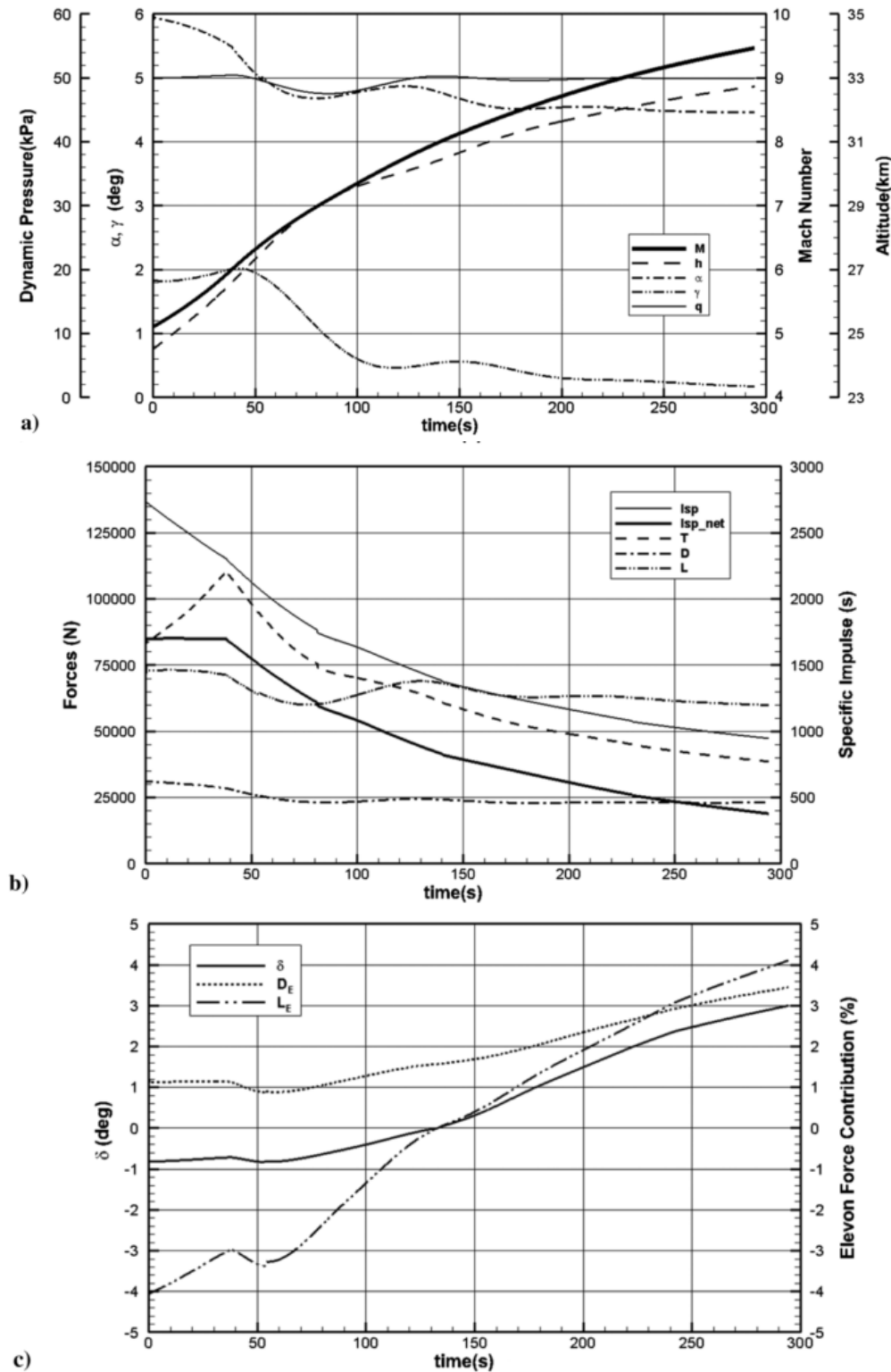


Figure 2.20: The flight trajectory of the SPARTAN

## 2.7. THE UNIVERSITY OF QUEENSLAND'S ROCKET-SCRAMJET-ROCKET LAUNCH SYSTEM

---

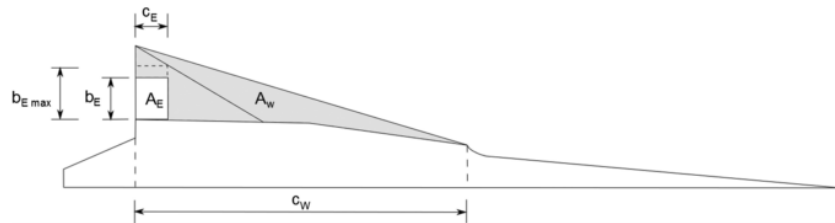


Figure 2.21: The elevons of the SPARTAN[94].

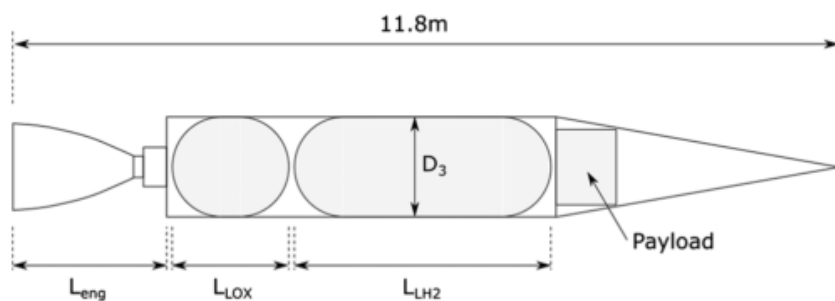


Figure 2.22: The third stage rocket of the rocket-scramjet-rocket launch system[94].

Engine	Fuel Supply	Fuel	Thrust	Isp	Mass	Diameter	Length	Thrust Vector Capability
Rl-10A-3A	Pump-Fed	LOX/LH <sub>2</sub>	73.4kN	444s	141kg	1.01m	1.78m	Yes, Unknown limits
Aestus II	Pump-fed	MMH/NTO	46kN	337.5s	148		2.2m	6°
RS-72	Pump-fed	MMH/NTO	55.4kN	338s	154kg		2.286	6°
ATE	Pump-fed	MMH/NTO	20kN	345s	57.9kg	0.38m	1.4m	15°
AJ10-118K	Pressure-fed	A-50/NTO	43.3kN	320.5s	124.5kg	1.53m	2.7m	Fixed
Kestrel	Pressure-fed	LOX/Kerosene	30.7kN	317s	52kg	1.1m	1.9m	Yes, Unknown limits
Aestus	Pressure-fed	MMH/NTO	27.5kN	320s	110kg	1.27m	2.2m	4° & 4° by mechanical adjustment
OMS	Pressure-fed	MMH/NTO	26.7kN	316s	118kg	1.168m	1.956m	8°

Table 2.2: Comparison of upper stage rocket engines, sourced from the Encyclopedia Astronautica reference website[134].

## 2.8 Optimal Control

Calculating the optimal trajectory of a launch system with multiple stages and multiple modes of propulsion is a complex process. Defining the trajectory of a launch system purely from vehicle analysis is unlikely to yield a trajectory which maximises the performance of the system. A simulation method is required which is able to calculate a trajectory path which maximises the performance of the launch system, while taking into account the aerodynamic and propulsive properties of each stage and propulsion mode. Optimal control theory is used in situations where an optimal trajectory path must be found with little prior knowledge of the shape of the trajectory. Optimal control theory has been widely used in aerospace applications, including being used to optimise the launch of hypersonic launch vehicles[CITATIONSXX].

For an optimisation of a complex trajectory there are a variety of optimal control methods that are useful for specific problem types. These are separated into two categories: direct and indirect solution methods. Indirect methods are based on the calculus of variations or minimum principle model, and generally result in high accuracy solutions to optimisation problems [16]. However indirect models suffer from the drawbacks of small radii of convergence and the fact that the equations to be solved often exhibit strong nonlinearity and discontinuities. This means that indirect methods will not be solvable unless the problem is very well defined with a minimum of nonlinearity, making indirect methods unsuitable for many complex optimisation problems, such as aerospace vehicle simulations which can exhibit strong nonlinear behaviour and have a wide solution space.

Direct methods transform an optimisation problem into a nonlinear programming (NLP) problem which can be solved computationally [120]. NLP solvers solve the optimisation problem defined as [10]:

$$\text{Minimise} \quad f(x) \quad (2.1)$$

$$\text{Subject to} \quad g_i(x) \leq 0 \quad \text{for } i = 1, \dots, m \quad (2.2)$$

$$\text{and} \quad h_j(x) = 0 \quad \text{for } j = 1, \dots, n \quad (2.3)$$

An optimisation problem that has been discretised in this form can thus be solved using any of a variety of NLP solvers. One of the most effective methods of solving twice differentiable NLP problems is sequential quadratic programming (SQP) [14] for which there is a variety of commercial solvers available such as NPSOL, SNOPT and packages within MATLAB.

In order for these packages to be able to solve an optimisation problem it must be presented in discretised form, and as such must be transformed using approximation techniques. The task of approximating a continuous optimisation problem in discrete NLP solvable form is not simple. SQP

solvers can very easily run into convergence issues when provided with an optimisation problem which has not been well defined. Also, any approximation must be carried out with care that the accuracy of the solution is not compromised. There are multiple ways to approximate a continuous optimisation problem directly as an NLP problem, the most common of which are shooting and collocation methods. The choice of discretisation method can affect the stability and accuracy of the solution as well as the solution time of the problem.

### **2.8.1 Shooting Methods**

Shooting methods in optimal control are forward-time methods of discretisation. Shooting methods explicitly enforce the dynamics of the system, and update the free conditions and system controls to move towards an optimal solution from an initial guess. Shooting methods are generally simple to apply, and require little specialised knowledge to use once they have been implemented.

#### **The Single Shooting Method**

The oldest and simplest method of approximating continuous optimisation problems as NLP problems is the direct single shooting method. Direct single shooting discretises the control function over the solution space, and solves this directly as an NLP by integrating the vehicle dynamics, or state variables, along the trajectory at each trajectory guess[12, 35, 61, 98]. Single shooting is simple to apply and has been used since the 1970s for rocket trajectory optimisation [55]. Single shooting methods suffer from nonlinearity problems, ie. an optimisation problem solved using the single shooting method will potentially struggle to solve if the problem exhibits even small nonlinearities, due to being unable to converge to an optimal solution. This makes the single shooting method unsuitable for complex problems such as a scramjet model, as there are many nonlinear factors inherent in atmosphere and airbreathing engine modelling.

#### **The Multiple Shooting Method**

Direct multiple shooting solves some of the instabilities of the single shooting method by splitting the trajectory into multiple shooting arcs, and collocating these at specific time points[12, 35, 61, 98]. This creates a system of discontinuities, illustrated in Figure 2.23, which are gradually removed by the solver algorithm until the trajectory is continuous. These discontinuities allow greater flexibility for the solver than is afforded by the single shooting method.

The multiple shooting method has greatly improved convergence compared to the single shooting method, removing much of the susceptibility to instabilities resulting from nonlinear effects. However, the multiple shooting approach still suffers from a relatively small radius of convergence and slow computation times. Radius of convergence is extremely important to this study as the optimal

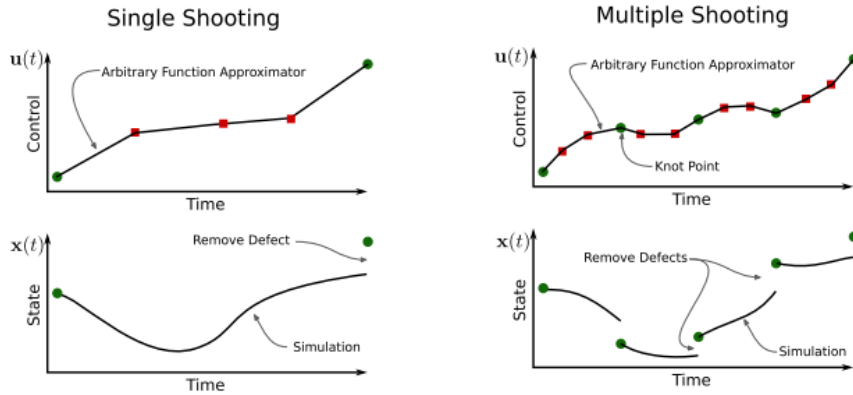


Figure 2.23: A comparison of single shooting and multiple shooting[61].

solution cannot be approximated to a great degree of accuracy, and as such multiple shooting was deemed inappropriate for this study. It was desired to find a method with a global radius of convergence to apply to the optimisation problem being considered.

## 2.8.2 Collocation Methods

Collocation methods are arguably the most powerful methods for solving optimal control problems[98]. Collocation methods are simultaneous methods, where both the states and controls are approximated using a specific form of functional[61, 98]. In these methods, the dynamics of the system are not explicitly enforced, but instead are constrained at specified points along the trajectory, called collocation points, or nodes[61]. This means that the derivative of the state functions become a constraint within the NLP, being equated to the polynomial approximation functions by the solver algorithm. Collocation methods provide larger radius of convergence, greater robustness, and smaller computational times compared to multiple shooting[35]. However, the solution accuracy of collocation methods is less than that of multiple shooting methods[35], although this can be improved through the choice of basis functions used for collocation[98].

Collocation methods can be represented in two ways; h and p schemes[61]. p schemes, or global methods, represent the entire trajectory as high order polynomials, and converge by increasing the order of these polynomial[61]. This method works well if the underlying solution is smooth, however, if there are discontinuities present, a P scheme will fail[61]. h schemes separate the trajectory into a series of medium order polynomials, stitched together at set points using defect constraints, similarly to the multiple shooting method[61, 98, 105]. These joining points are called knot points[61, 105]. A comparison between h and p methods is shown in Figure 2.24.

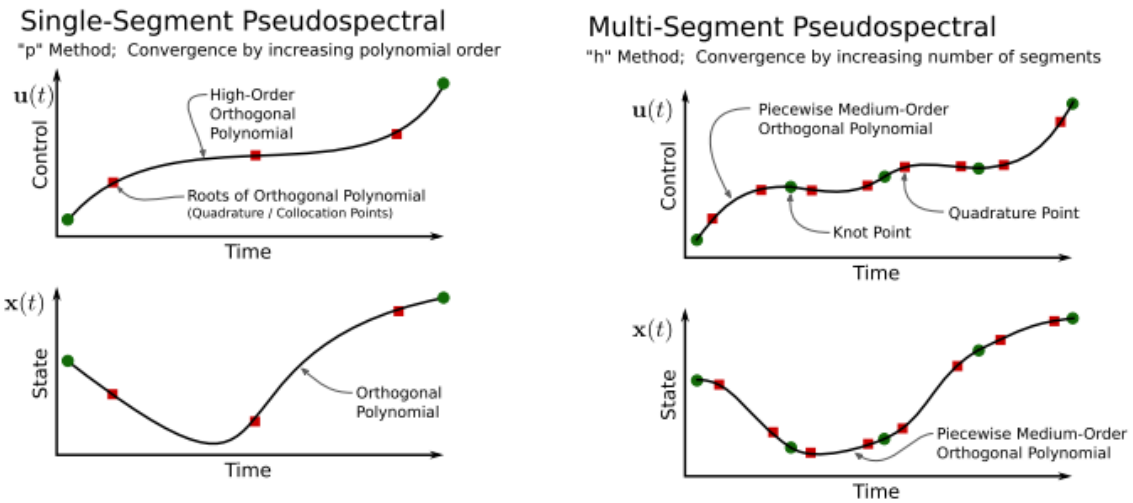


Figure 2.24: Examples of h and p collocation methods[61].

### The Pseudospectral Method

The most accurate and effective type of collocation methods use orthogonal polynomials to approximate the state and control functionals[32]. In trajectory optimisation, this type of collocation is referred to as the pseudospectral method[61]. The pseudospectral method was first introduced in 1972 by Kreiss & Oliger [66] as an efficient way to compute meteorology and oceanography problems. The pseudospectral method has recently garnered a large amount of attention for its ability to rapidly and accurately solve a wide variety of optimal control problems. The pseudospectral method employs the use of orthogonal polynomials such as Legendre or Chebychev polynomials to approximate the state and control functions at a specific set of collocation points[32, 53, 61, 98]. When a solution is well behaved and smooth, the pseudospectral method converges at an exponential rate, with a high accuracy known as spectral accuracy[28, 105].

There are multiple types of pseudospectral methods, distinguished by the polynomial and collocation points used. Usually, these polynomials are Chebyshev or Lagrange polynomials[32, 98], and the collocation points are the roots of a Legendre polynomial[42]. Chebyshev polynomials have been used since the introduction of pseudospectral methods in optimal control, but have been superseded in many cases by Lagrange polynomials, which offer simpler collocation conditions[98]. There are many possible types of collocation nodes, although there are three most commonly used sets; Legendre-Gauss (LG); Legendre-Gauss-Radau (LGR); and Legendre-Gauss-Lobatto (LGL)[42, 98]. The choice of collocation type determines how the roots of the problem are calculated, and changes the formulation of the problem slightly[42]. Practically, there is very little difference between these node sets [42].

The pseudospectral method is usually employed as a p method, where a global polynomial is used, and convergence is achieved by increasing the order of this polynomial[98]. Recently, hp-adaptive

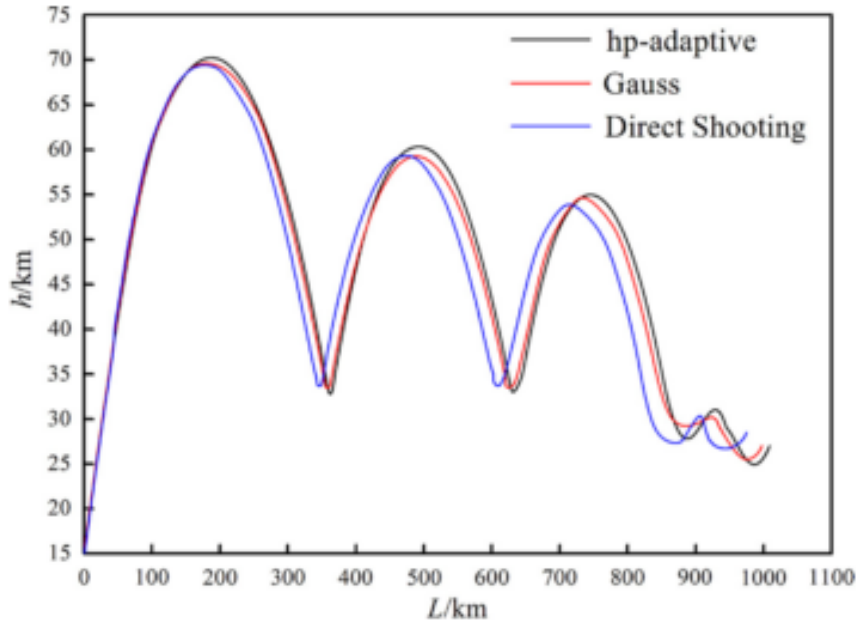


Figure 2.25: Comparison of optimisation techniques[17]. A hypersonic vehicle is optimised for maximum range. The hp-adaptive method can be observed to have produced the most optimal result.

pseudospectral methods have been introduced, which segment the mesh using an  $h$  method, whilst also having a variable polynomial degree, as in the  $p$  method[28]. These  $hp$  methods converge by varying the degree of the approximating polynomial as well as the number of segments simultaneously. Utilising both  $h$  and  $p$  methods improves the accuracy and robustness of the solution, as illustrated in Figure 2.25, from a study by Chai et al.[17] comparing the single shooting method to  $p$  and  $hp$ -adaptive pseudospectral methods. Additionally, the  $hp$ -adaptive method decreases the computational effort and memory usage necessary during the solution process[17, 28].

A secondary usability advantage of the pseudospectral method is the ability to generate Hamiltonian and costate values easily[33, 46, 98]. The Hamiltonian and costate values allow a solution to easily and quickly be checked to determine if some of the necessary conditions for optimality are being met. This is useful to determine initially if the optimal solution calculated by the pseudospectral solver is valid.

The pseudospectral method has been proven to be extremely effective for simulations in aerospace applications and has been proven in flight applications such as the zero propellant manoeuvre of the International Space Station in 2007, where the ISS was rotated 180 degrees without any propellant used following a pseudospectral method solution [11]. The pseudospectral method has been used successfully in a multitude of studies for the trajectory optimisation of hypersonic vehicles[17, 29, 57, 65, 71, 77, 100, 125, 137, 140]. These results indicate that the pseudospectral method is robust for complex, nonlinear systems, and that the pseudospectral method can be used for systems with many state variables[CITATIONXX].

## 2.9 Available Optimal Control Solvers

There are a number of optimal control solvers available, both commercially and open source. A summary of the most prominent available solvers is shown in Table 2.3. These programs are mostly general solvers, and must be configured specifically in order to solve a particular optimal control problem. The exception is ASTOS[8], which is a standalone program designed for aerospace trajectory optimisation.

Functionally, most of the available solvers are similar in operation. The states and controls of the optimal control problem are defined to the program by the user, along with any constraints; continuous or endpoint. The cost function of the problem is input, and dynamic model of the system is defined. An initial guess is provided, and once activated, the solver will move toward an optimal solution from this initial guess. The most significant practical difference between the solvers lies in the robustness of the optimal solution, ie. how easily a particular solver is able to converge to the optimal solution. For a simple and continuous optimisation problem all solvers will be able to approach the same solution (though with varying efficiency). However, for a complex and nonlinear optimisation problem, some solvers will converge much more easily than others. Generally, this stems from the underlying transcription method used.

The most common form of discretisation used by these solvers is the pseudospectral method, although other forms of collocation, as well as multiple shooting, are also used. Comparing the benefits of these solvers is difficult, as a particular problem may lend itself to one solver in particular, and all have been used widely. However, it is generally held that hp-adaptive pseudospectral methods are the current state-of-the-art in discretisation methods, and a solver which utilises one of these techniques is likely to have good convergence and accuracy properties[citeXX]. The readily available packages which utilise hp adaptive pseudospectral methods are GPOPS-2[97] and ICLOCS2[80].

ICLOCS2 is a software package in the alpha stages of development, which is based upon ICLOCS, a multiple shooting solver[80]. ICLOCS2 is able to implement a range of transcription methods, including a hp adaptive Legendre-Gauss Pseudospectral method[80]. As ICLOCS2 is relatively new at the time of writing, it has not yet been implemented in any published works and documentation is limited.

GPOPS-2 is a proprietary hp-adaptive pseudospectral method solver, which implements a variety of hp-adaptive pseudospectral methods, so that the best method may be chosen for a given problem[97]. GPOPS-2 is specifically designed to be as flexible as possible, to accommodate for a wide range of problem formulations[97]. GPOPS-2 is well proven in aerospace applications, and has been used for spacecraft orbit optimisation as well as in-atmosphere trajectory optimisation[CITEXX]. GPOPS-2 is well suited to solving multi-phase optimal control problems, which is necessary for efficient multi-stage launch optimisation[97]. GPOPS-2 represents the state of the art in trajectory optimisation software, and as such is used by a number of institutions around the world.

Both ICLOCS2 and GPOPS-2 uses IPOPT[133] (Interior Point OPTimizer) as the standard nonlinear programming solver (with the option of installing others). IPOPT is a widely used open source nonlinear optimisation package which utilises an interior point line search filter method.

Software	Publisher	Platform	Optimisation Type
DIDO[104]	Elissar Global	MATLAB	Chebychev Pseudospectral
GPOPS II[97]	RP Optimization Research	MATLAB	hp Adaptive Legendre-Gauss-Radau Pseudospectral
PROPT (IPOPT) [106]	TOMLAB	MATLAB	Legendre-Gauss Pseudospectral
ICLOCS2[80]	Imperial College	MATLAB	Multiple Shooting / hp Legendre-Gauss Pseudospectral
POST2[19]	NASA	FORTRAN	Direct Shooting
OTIS[34]	NASA	Fortran	Pseudospectral + Various
TRANSWORHP[135]	ESA	Fortran/C++	Full Discretisation
ASTOS[8]	Astos Solutions	Standalone	Multiple Shooting/Collocation
ACADO[52]	Open Source	C++	Direct
JModelica[56]	Modelon AB, Open Source	Modelica/Python	Collocation/Pseudospectral

Table 2.3: Summary of programs capable of pseudospectral optimisation.

## 2.10 Aerodynamic Analysis

Simulating the trajectory of access to space systems requires the aerodynamics of each stage of the launch system to be characterised at every flight condition experienced during launch. For this to be possible, it is necessary to create large aerodynamic coefficient databases, which cover the operable region of the vehicle, and include the effects of control surface deflections and propulsion.

There are a variety of tools available to calculate the aerodynamics of aerospace vehicles. These tools are primarily designed towards either accuracy or efficiency, as more accurate methods require more computational power, longer computational times and, usually, more man-hours to produce a solution. This trade off means a tool must be selected which best suits the requirements of a given problem. For a preliminary vehicle design, it is often desirable to select a tool which is as computationally efficient as possible, as the design of the vehicle is liable to change often. Whereas for more advanced stages of vehicle design, an accurate tool is desirable, to assess the design of the vehicle in detail.

The lowest fidelity, and highest efficiency methods include packages which use empirical relations derived from databases of existing vehicles, such as Missile DATCOM[citeXX missile datcom], as well as panel method codes such as HYPAERO, cbaero and HOTSOSE[cite cbaero, HYPAERO, hotsose]. Low fidelity methods offer rapid solutions, with highly variable accuracy. For simple, standard vehicle shapes, low fidelity methods may offer high accuracy, as low fidelity solutions are usually calibrated to higher fidelity simulations or experiments. However, for complex vehicle geometries, for example geometries involving engine through-flow, low fidelity models may be highly inaccurate, and are not acceptable for use[31].

Medium fidelity methods consist of inviscid Euler solvers such as CART3D, FUN3D and AIRPLANE[cite cart3d, AIRPLANE], which are able to provide reasonable accuracy, with medium run times, by neglecting viscous effects within the solution. These solvers are often used in the later stages of preliminary design, or when higher fidelity is necessary due to design features, but rapid solutions are still desired. Neglecting the viscous effects in the fluid flow means that the solution obtained from an inviscid solver will only be an approximation of the real flow, and that the accuracy of the solution varies depending on the type problem being solved. For problems such as lift on a thin airfoil, inviscid Euler methods may be quite accurate, however for a problem such as boundary growth on a flat plate these methods will not accurately model the solution[79]. A particular advantage that many inviscid Euler codes provide is automatic adjoint mesh adaptation, the ability for the mesh to be automatically and rapidly generated, and updated sequentially throughout the solution process, refining areas of complex geometry or flow. This enables multiple solutions to be easily computed, without the need to regenerate meshes manually. For preliminary design purposes, inviscid-flow Euler CFD solvers are used extensively across industry and academia[6].

High fidelity methods consist of Navier-Stokes CFD solvers such as Eilmer3/4, Fluent, CFX, STAR-CD, COMSOL and OpenFOAM [citationsxx]. These solvers will resolve the fluid flow and aerodynamic forces to a high level of accuracy, including viscous effects. However, the mesh for the problem must be generated prior to the calculation of the solution, which increases the working time significantly. Additionally, the computation times are much longer, and require more computational resources than lower fidelity methods. These factors make the generation of an aerodynamic database using high fidelity CFD an extremely time consuming process, which is suited for use on mature vehicle designs, or when accurate flow simulation is absolutely necessary. This is the case for the simulation of scramjet engines, which contain complex flow fields featuring high Reynolds-number flow, complex shock wave structures, and large thermal and composition gradients[110]. For this reason, scramjet engines must be simulated using high-fidelity methods to produce an accurate solution.

## 2.10.1 CART3D

CART3D is an inviscid CFD package, designed for use during preliminary vehicle design and analysis[6]. CART3D is computationally efficient and requires only a surface triangulation of the vehicle being analysed to initiate a simulation. CART3D features adjoint mesh adaptation, and uses cartesian 'cut-cells' which intersect the surface, allowing complex geometries to be analysed. The mesh automatically refines as the simulation progresses, reducing error. The absence of a requirement for a user generated mesh allows CART3D to be easily applied to complex launch vehicle designs, as well as allowing for simple modification of control surface deflections and flight conditions. CART3D has been used extensively for aerodynamic simulations in preliminary design, including analysis of the plumes of the Skylon spaceplane[74], HIFIRE-5[64], and in low sonic boom shape optimisations[3]. CART3D has shown good agreement when compared to experimental results for winged boosters

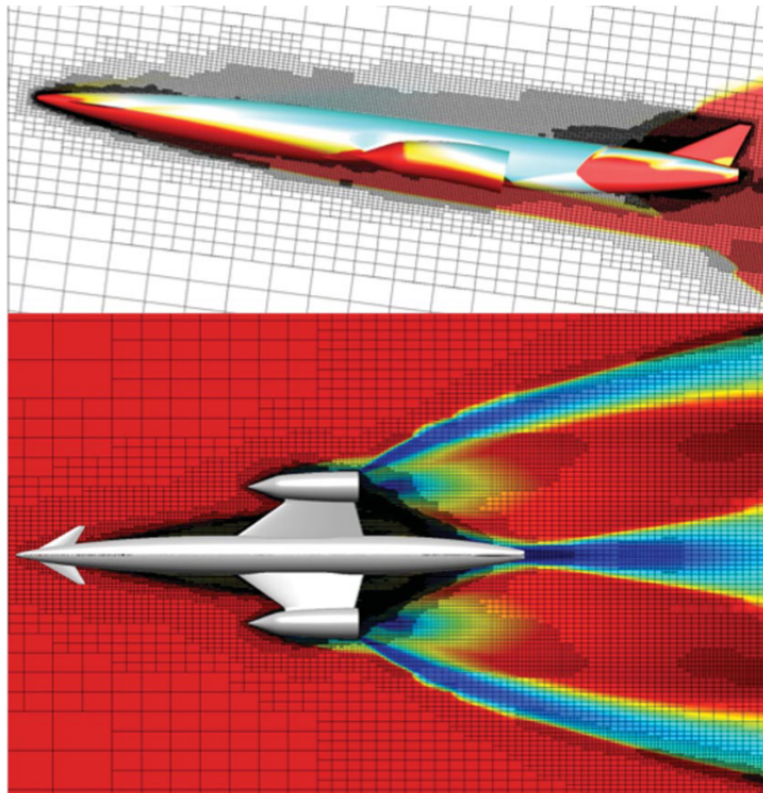


Figure 2.26: The Skylon spaceplane, simulated using CART3D at Mach 12.189,  $\alpha = 7.512^\circ$ [74]. Cell distribution produced by mesh adaptation is shown.

at hypersonic speeds[108], as well as supersonic missiles[1] and aircraft[3], and lifting bodies across wide Mach number ranges[5]. In addition, good agreement has been shown between CART3D, experimental results, and full Navier-Stokes solutions for the HIFIRE-1 hypersonic test payload[108]. In this case, the exception to close agreement was at an identified area of shock-induced boundary layer separation, which an inviscid solution does not capture[108]. The model of the HIFIRE-1 and pressure

coefficient results at each pressure tap are shown in Figure 2.27. Finally, in a comparison between CART3D and the Overflow-D Navier-Stokes solver, it was shown that both codes produce similar pressure distributions for simulations of the space shuttle fuel tanks at low Mach numbers[44]. The Overflow-D simulations were stated to require at least 20 times more CPU time than CART3D[44], an example of the efficiency afforded by CART3D.

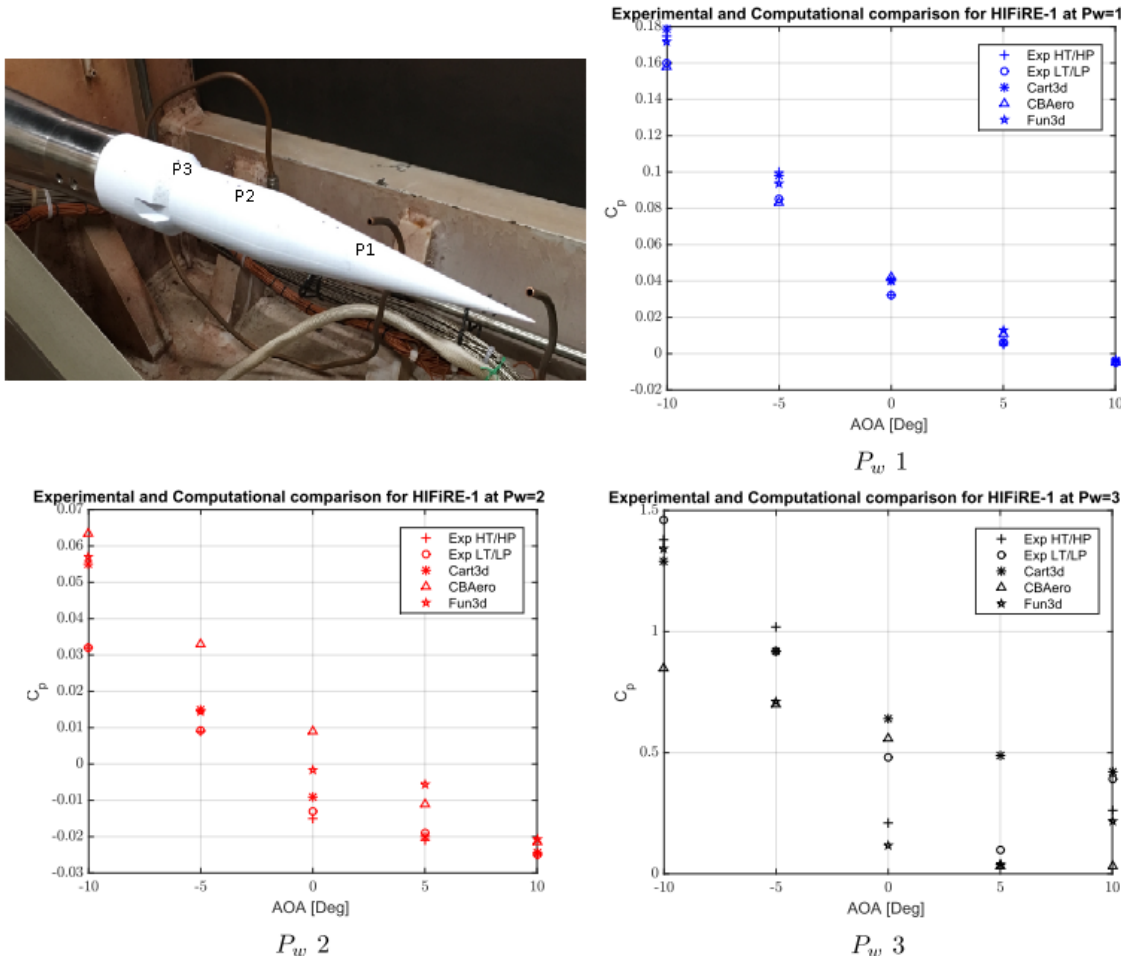


Figure 2.27: Comparisons of CART3D with experimental data and the FUN3D Navier-Stokes CFD solver. P1, P2 and P3 indicate pressure tap locations. Modified from Sagerman et al.[108].

## 2.10.2 Missile DATCOM

Missile DATCOM is a widely used, semi-empirical, aerodynamic prediction tool for missile configurations. Missile DATCOM uses component-buildup methods by which the aerodynamics of each component of the missile or rocket design are estimated and then added together to determine the aerodynamics of the entire vehicle. Missile DATCOM uses a combination of empirical and theoretical methods and is capable of calculating the aerodynamic forces, stability derivatives and moments over a range of angle of attack and Mach number values. The high efficiency of Missile DATCOM

allows an aerodynamic database to be generated simply and rapidly. Missile DATCOM has been shown to produce close agreement with experimental wind tunnel data for normal force and pitching moment coefficients, and reasonable agreement for axial force coefficients[118].



---

---

## CHAPTER 3

---

### LAUNCH VEHICLE DESIGN AND SIMULATION

First stage has been changed to 8.5m , with 1m of space for connection, also 70% thrust. Will include a section describing the launch site (ELA). Will put in pictures defining sun synch orbit, and more detail about sun synchronous orbit

Fuel tanks are depleted cylindrical first, to move CG for stability, and to minimise slosh (maybe point towards concorde here)

In order to be competitive in the emerging small satellite market, a small satellite launcher must be cost-effective, reliable, and capable of launching on a flexible schedule. The inclusion of airbreathing engines within a small satellite launch system has the potential for improving cost effectiveness compared to disposable rocket-powered launchers, by allowing partial reusability of a launch system. The airbreathing engine most appropriate for small satellite launch systems are scramjet engines, which operate efficiently within the hypersonic regime, with the capability to operate over a relatively large Mach number range compared to turbojet or ramjet engines. A launch system incorporating scramjets must necessarily include two rocket-powered flight stages; a first stage rocket to accelerate the system from launch to the minimum operational Mach number of the ramjet or scramjet engines; and a third stage rocket to accelerate the payload at exoatmospheric conditions and place it into the correct orbit. This chapter presents the design and modelling of a rocket-scramjet-rocket launch system in which the scramjet stage is reusable for multiple launches. For this launch system to be economically viable, the scramjet stage must be capable of accelerating to a high Mach number, and then returning to its initial launch site for re-use. Returning to the initial launch site removes the need for costly and time-consuming transportation, and allows the refurbishment and refuelling of the scramjet stage to begin immediately. This rocket-scramjet-rocket launch system is designed to launch satellites on the order of 200kg to a 567km altitude sun-synchronous orbit. A sun synchronous orbit is targeted as it is a potentially desirable orbit for small satellite missions, being advantageous for imaging purposes due to its low altitude and consistently timed overpasses. This orbit is consistent with previous

studies which have investigated rocket-scramjet-rocket small satellite launch systems, allowing the missions developed in this study to be compared and contrasted to unoptimised mission profiles. The rocket-scramjet-rocket launch system described in this chapter is used as a representative model for an airbreathing, partially-reusable, multi-stage small satellite launcher.

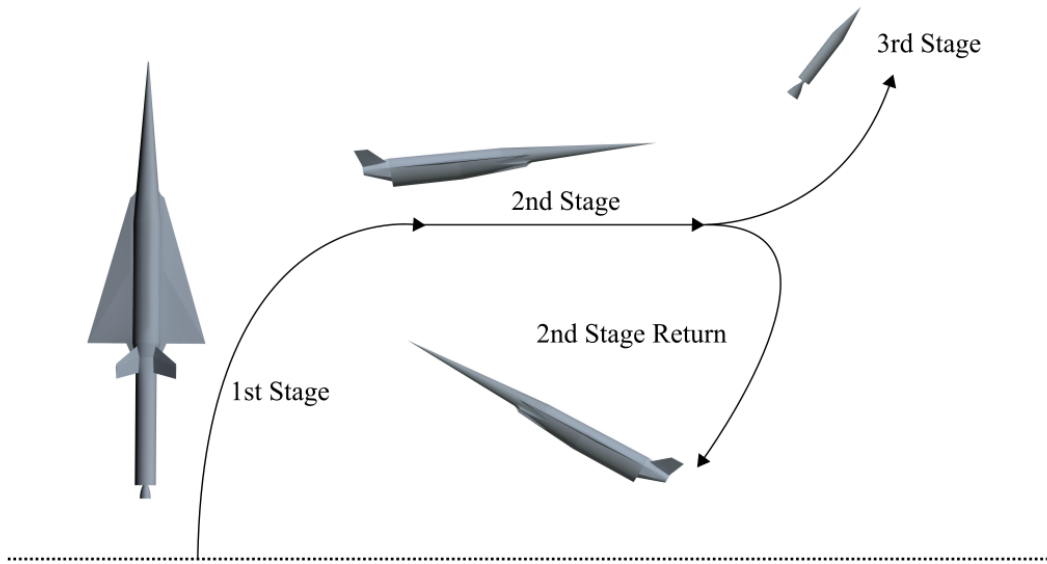


Figure 3.1: The launch process of the rocket-scramjet-rocket launch system, presented in simplified form.

The rocket-scramjet-rocket launch system used in this study has been designed based on the SPARTAN scramjet accelerator developed by Preller & Smart [CITATIONXX]. The SPARTAN is a scramjet-powered accelerator being developed by The University of Queensland and Hypersonix. The SPARTAN has been designed for small satellite launches, as part of a rocket-scramjet-rocket launch system. The SPARTAN has been used as the basis for design of the launch system, as it is the most complex stage of the system, and its unique trajectory requirements drive the design of the other stages. The trajectory of a launch system involving scramjet propulsion is significantly different to that of a fully rocket-powered launch system. Figure 3.1 shows a simplified representation of the launch trajectory for the vehicle simulated in this study. The operation of the scramjet engine requires in-atmosphere flight, at high dynamic pressure conditions for long periods of time. The launch system must be designed to withstand the high structural loading and heating generated by flight at these conditions. The SPARTAN vehicle is mounted to the front of the first stage rocket. The launch system is launched vertically under rocket power, from a traditional small rocket launch facility. This configuration allows the SPARTAN to take the brunt of the aerodynamic forces and heating, as well as allowing the use of the control surfaces of the SPARTAN. During first stage rocket operation, the

---

launch system pitches rapidly, reaching close to horizontal flight to allow the SPARTAN to stay at high dynamic pressure conditions. The SPARTAN is accelerated to its minimum operating velocity of approximately Mach 5, at which point separation occurs. The SPARTAN's four scramjet engines are ignited, and The SPARTAN is accelerated through the atmosphere, reaching approximately Mach 9. At this point, the specific impulse of the scramjet engines, and thus the efficiency of the SPARTAN, have decreased, and the third stage rocket is separated. The third stage rocket accelerates and performs a pull-up, before cutting its engine and coasting out of the atmosphere. Once the rocket is exoatmospheric, the engine is reignited, performing first a circularisation burn, and then a Hohmann transfer to the intended orbit. Meanwhile, the SPARTAN banks and executes a fly-back manoeuvre to return to its initial launch site. The SPARTAN extends landing gear, and lands on a traditional runway in the style of a conventional aircraft. The SPARTAN is able to be rapidly refurbished and remounted for further launches. To fulfil the requirements of this trajectory, The SPARTAN must be able to fly and manoeuvre at all Mach numbers from 0 to 9, as well as being able to withstand high structural and heating loads without significant deterioration.

The three stage launch system incorporating the SPARTAN is shown in Figures 3.2 & 3.3. The size and external design of the SPARTAN scramjet accelerator are used exactly as defined for the Baseline SPARTAN vehicle defined by Preller & Smart. The internal layout has been designed for the SPARTAN to carry a large fuel volume while allowing the third stage to fit within the fuselage. The first and third stages have been designed for this study. The third stage rocket replaces the third stage used in previous SPARTAN studies, which was powered by a Pratt & Whitney RL-10-3A engine, with a rocket stage powered by a SpaceX Kestrel engine. The SPARTAN design is presented first, as the design of the SPARTAN drives the design of the first and third stage rockets.

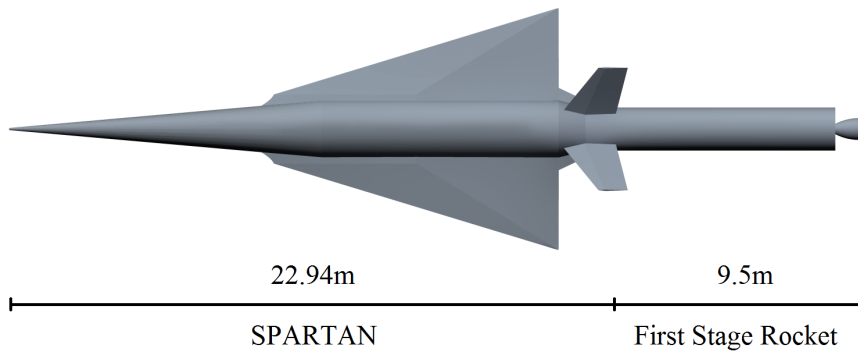


Figure 3.2: The rocket-scramjet-rocket launch system, top view, showing the SPARTAN and first stage.



Figure 3.3: The rocket-scramjet-rocket launch system, side view, showing the SPARTAN and fuel tanks, along with the third and first stages.

## 3.1 Second Stage Scramjet

### 3.1.1 The SPARTAN Accelerator

The SPARTAN vehicle in this study is designed based on the work by Preller & Smart CITATION. The SPARTAN is 22.94m long, with a frontal cone half angle of  $5^\circ$  [CITEXX DAWIDS THESIS]. A mass breakdown of the SPARTAN is shown in Table 3.1, adapted from [CITAXX Dawids thesis]. The fuel tank sizes and total fuel mass are sized to accommodate for the Kestrel-powered third stage, described in Section 3.3. This study assumes that the third stage is stored within the fuselage of the

Part	Fuselage	Wings	Tanks	Systems	Landing Gear	Scramjets	Fuel
Mass (kg)	2861.6	350.7	179.4	707.5	188.9	669.0	1562.0

Table 3.1: Mass breakdown of the modified SPARTAN vehicle.

SPARTAN for simplicity. It is assumed that the release mechanism for the third stage is able to be situated within the available space surrounding the third stage, however the release mechanism is not considered further in this study.

The fuel tanks are sized to fit around the kestrel-powered third stage. There are three fuel tanks; two cylindrical tanks situated underneath the third stage; and a truncated conical tank in the nose. The conical fuel tank is designed to fit immediately forward of the third stage. This fuel tank is 8m long, leaving  $1.47\text{m}^3$  of space in the nose for cooling systems, frontal landing gear and any additional systems or sensors which are necessary in the nose cone. The cylindrical tanks are positioned underneath and slightly to either side of the third stage, leaving space underneath for vehicle systems. The cylindrical fuel tanks are designed to be 8.5m long, with diameters of 0.87m, sized to give a nominal total tank volume of  $22\text{m}^3$ . The fuel tanks hold a total of 1562kg of LH2 fuel. This assumes an LH2 density of  $71\text{kg/m}^3$ , slightly denser than LH2 at phase transition point at 1 atm. The mass of the fuel tanks is scaled from Dawid Preller's Baseline vehicle model of the SPARTAN, giving a total fuel tank mass of 179.4kg.

### 3.1.2 Propulsion

The SPARTAN is powered by four underslung scramjet engines, fuelled by liquid hydrogen. These engines are Rectangular To Elliptical Shape Transition (REST) engines, configured to allow for a conical forebody (C-REST). REST engines have a rectangular to elliptical shape transition inlet, and an elliptical combustor, offering simplicity in design as well as reduced thermal loading and viscous drag compared to scramjets with planar geometries [121]. REST engines are also specifically designed to operate over a wide range of Mach numbers, and at off design conditions, making them particularly applicable to use on scramjet accelerator vehicles.

#### Propulsion Modelling

The properties of the C-REST scramjet engines must be modelled at every flight condition which the SPARTAN may experience during its flight. The thrust generated by the C-REST engines determines how rapidly the SPARTAN accelerates, and the efficiency of the engines determines the total flight time, and influences the separation point of the third stage rocket. The C-REST engines are simulated separately to the aerodynamic simulations of the SPARTAN, using quasi-1D simulation for simplicity. The engine model takes the conditions at the inlet, and calculates the exit conditions and propulsive properties of the engine. The engine exit conditions are added into the aerodynamic simulations and the propulsive properties are used in the simulated vehicle model.

Before the flow enters the engine, it is affected by the conical shock generated by the forebody of the SPARTAN. Figure 3.4 shows the locations of the flow properties which are necessary to calculate engine performance. The ambient atmospheric conditions are calculated by interpolation using the 1976 NASA Atmospheric properties[78]. The flow properties at the inlet of the engines is calculated using the Taylor-Maccoll analysis method for conical shocks[CitationXX]. This calculation is performed in the cone\_shoot program provided for this study by Prof. Michael Smart[CitationXX?]. The flow conditions following the conical shock are shown in Figure 3.5.

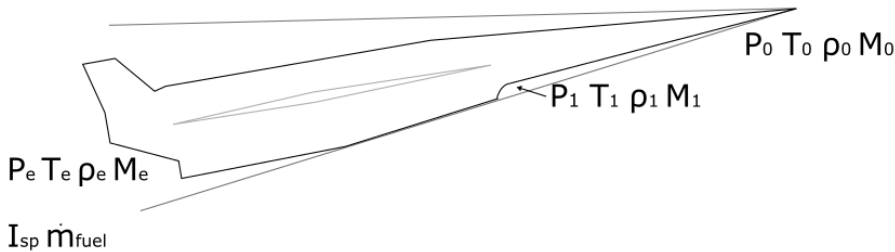


Figure 3.4: The locations of conditions relevant to C-REST engine simulation.

The engine model used is a CRESTM10 database[90, 94], analysed using quasi-1D simulation and provided for this study by Prof. Michael Smart. This database has previously been used in simulations of the SPARTAN, as explained in Section 2.7.1. This database provides data points of

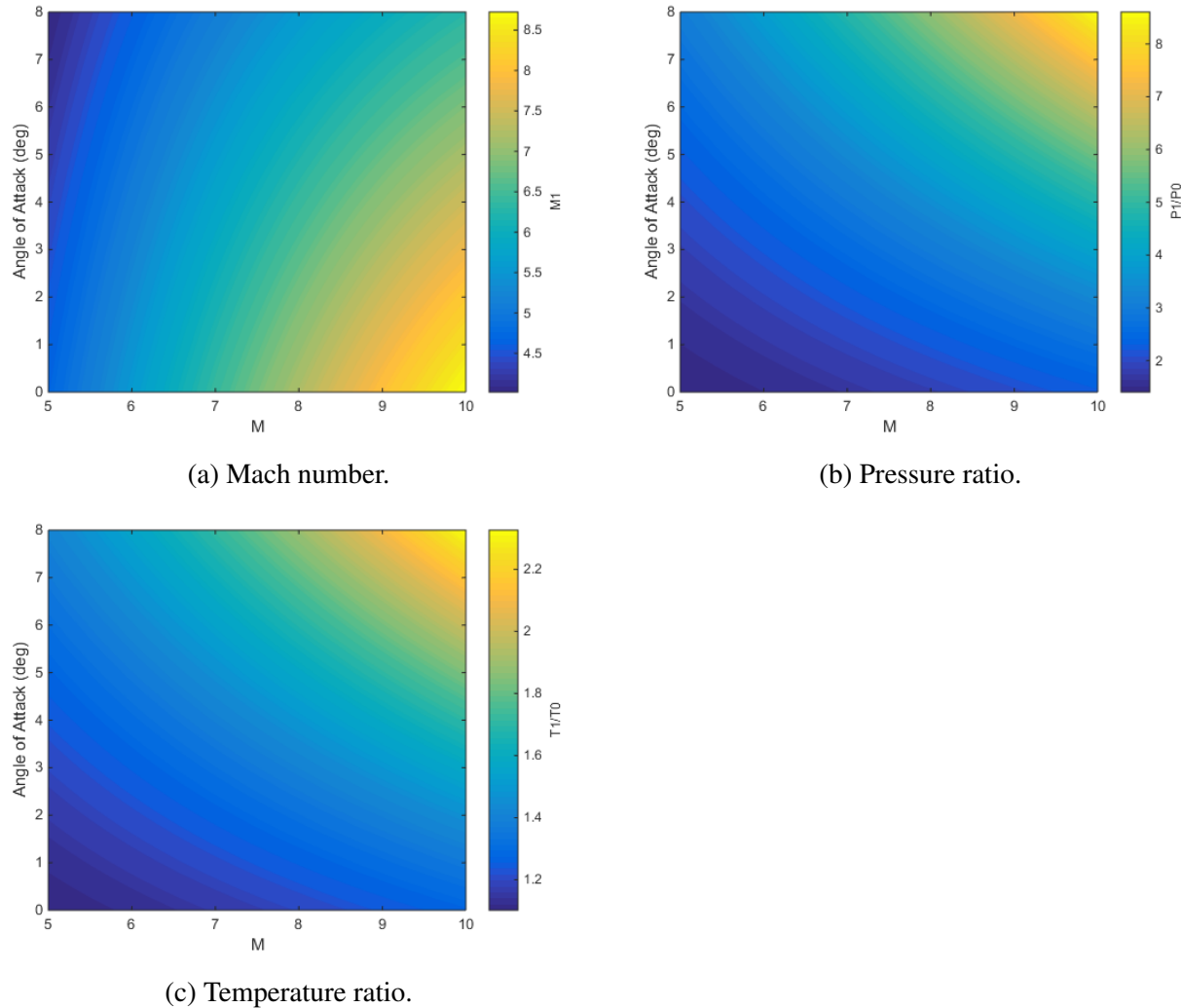


Figure 3.5: Flow conditions after the conical shock generated by the vehicle nose cone. Figure a) shows the Mach number, b) shows the pressure ratio, and c) shows the temperature ratio following the conical shock.

engine performance over inlet conditions within the operational range, at 50kPa dynamic pressure equivalent conditions. The specific impulse data set is shown in Figure 3.6. This data is interpolated using bivariate splines for the given inlet conditions, to calculate specific impulse produced by the engine. During flight the C-REST inlet conditions will stay within the region bounded by the available data. However, for the purposes of the trajectory optimisation, it is necessary for the vehicle model to be able to extrapolate for ISP and equivalence ratio data. This extrapolation is linear, and is used to drive the optimisation, but does not directly affect the final solution. For operation at high Mach numbers, the fuel mass flow rate is assumed to be stoichiometric, so that  $m_f = 0.0291\dot{m}$ . This ensures that the scramjet engines are performing at high efficiency throughout the acceleration of the scramjet stage. However, the C-REST engine is a fixed geometry engine, primarily designed for operability

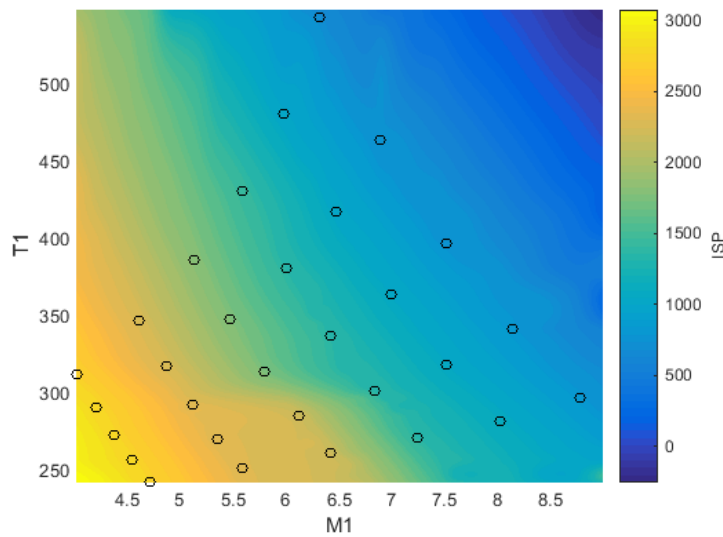


Figure 3.6: Specific impulse of the CRESTM10 engines with input temperature and Mach number. Available data points are indicated.

at high Mach numbers[94]. At lower Mach numbers, the addition of excessive fuel may cause the engine to choke and unstart, resulting in total loss of thrust[94]. To avoid unstart, an equivalence ratio ( $\phi$ ) of less than 1 is set at low Mach numbers. The equivalence ratio interpolation is linear, as the number of data points available for interpolation is low. The equivalence ratio over the range of SPARTAN operation is shown in Figure 3.7. The fuel mass flow rate is determined by approximating the flow into the inlet as an ideal gas;

$$\dot{m} = 0.9m_c A_{cap} P_0 M_0 \sqrt{\frac{\gamma_0}{R_{air} T_0}},$$

$$\dot{m}_{fuel} = \left(\frac{m_{fuel}}{m_{ox}}\right)_{st} \phi \dot{m}$$

The multiplier of 0.9 is an approximate term included to account for losses due to asymmetry within the engine[90]. The thrust for each engine,  $T$ , is obtained by inclusion of the interpolated specific impulse, ie.

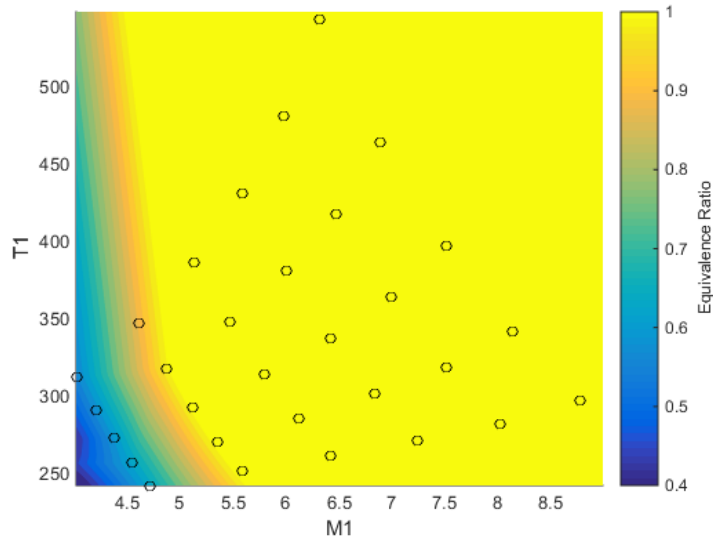


Figure 3.7: Operable equivalence ratio of the CRESTM10 engines with input temperature and Mach number. Available data points are indicated.

$$T = g_0 \dot{m} I_{sp}.$$

### 3.1.3 The Aerodynamics of the SPARTAN

*Note: Viscous correction will be added to the aerodynamic database, calculated by Alexander Ward. The additional thrust obtained by the nozzle exit and boat tail is currently being computed in Cart3d and will be added to the propulsive database.*

In order for the trajectory of the SPARTAN to be successfully simulated and optimised, the aerodynamics of the SPARTAN must be calculated for the large range of flight conditions experienced during the acceleration and return flights. The aerodynamics of the SPARTAN are calculated at set flight conditions covering the breadth of necessary conditions, and the results are tabulated in databases. During simulation, the aerodynamics of the SPARTAN are determined by interpolation over the aerodynamic databases using bivariate splines.

The aerodynamics are calculated for Mach numbers between 0-10, angles of attack between 0° and 10°, and for altitudes between 0-40km. Separate aerodynamic simulations are performed for engine-on and engine-off conditions, as the operation of the scramjet engines changes the aerodynamic characteristics of the SPARTAN significantly. When the engines are powered on, the engines are generating thrust on the internal nozzle, as well as on the boat-tail and base. When the scramjet engines are not operational air flows through the flowpath without fuel injection, generating a large amount of drag. The drag, lift and moment coefficients are determined by interpolating for Mach number, angle of attack, altitude, and centre of gravity as it shifts during flight. The drag and lift produced by each stage of the vehicle are calculated using the standard definition of the aerodynamic

coefficients:

$$F_d = \frac{1}{2} \rho c_d v^2 A, \quad (3.1)$$

$$F_L = \frac{1}{2} \rho c_L v^2 A. \quad (3.2)$$

## CART3D

The aerodynamics of the SPARTAN have been calculated using CART3D, an inviscid CFD package used in the preliminary design of aerospace vehicles. Cart3D utilises adjoint mesh adaption with a Cartesian cut-cells approach to produce an iteratively refined mesh to fit a flow solution. CART3D is been used to generate the aerodynamic database of the SPARTAN vehicle due to its applicability in both the subsonic and supersonic regimes, and its robustness across multiple flow solutions [16]. CART3D has previously been used to analyse hypersonic vehicles, and has shown fair agreement with experimental data across multiple studies CITATIONXX.

The CART3D Meshes are initiated with an outer boundary distance of 40 times the vehicle length. This boundary distance was observed to produce suitable free stream conditions and good mesh convergence. Nine mesh adaption levels are used. Nine levels have been observed to generally produce good convergence, with moderate computation times of 1-3 hours per simulation. The convergence of the residuals and forces are investigated to ascertain if a solution has converged. Figure XX shows an example solution validation for Mach 7, 2° angle of attack, engine-on conditions. Good convergence can be observed in the force functionals, with a corresponding decrease in the residual values indicating solution convergence.

*A CART3D validation image will be inserted here, showing decreasing residuals and converging functionals.*

## Trim Analysis

The SPARTAN is trimmed during flight using control surfaces on the wings. The trim is incorporated into the aerodynamic databases prior to trajectory simulation, assuming that the SPARTAN is trimmed at all conditions during flight. The SPARTAN is trimmed using control surfaces on the wings, shown in figure 3.8. Trim is determined by calculating the aerodynamic moment coefficient with zero flap deflection, then calculating the flap deflection necessary to balance the aerodynamic moments to zero. The moment generated by the body and wings of the SPARTAN is balanced by the moment generated by the ailerons, as well as the thrust moments on the engines and boat tail, when the C-REST engines are powered on. The force balance on the SPARTAN is shown in Figure 3.9. This trim balancing is calculated prior to trajectory optimisation for computational efficiency.

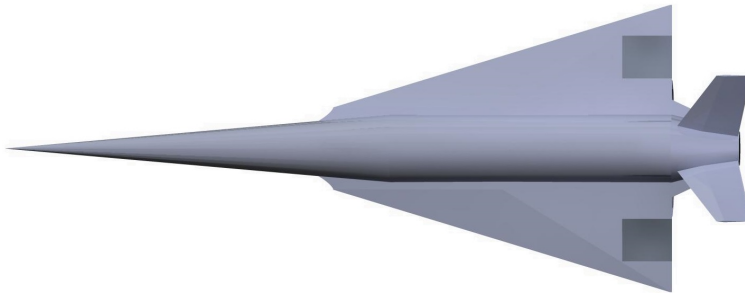


Figure 3.8: SPARTAN model showing control surfaces. *Dimensions will be included.*

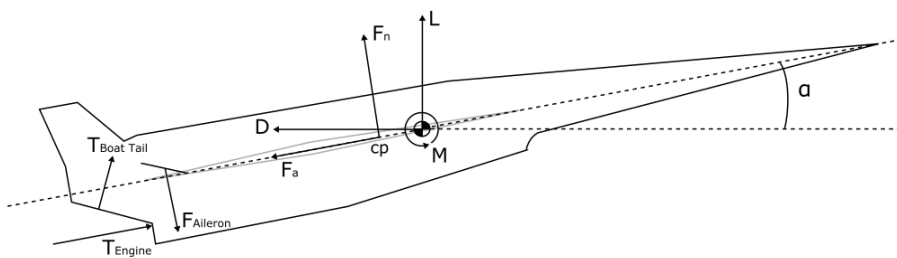


Figure 3.9: The forces on the SPARTAN during flight.

The centre of gravity of the SPARTAN is calculated using CREO. The centre of gravity varies during flight due to fuel consumption and third stage release, changing the necessary flap deflections for trim. Consequently, aerodynamic databases are created for centre of gravity conditions;

- full fuel including third stage,
- empty of fuel including third stage,
- empty of fuel after third stage release.

At each of these conditions, aerodynamic coefficients and flap deflections necessary for trim are calculated. For simplicity, it is assumed that structural, systems and landing gear masses are homogeneously distributed throughout the centre fuselage of the SPARTAN. The calculated centre of gravity for the SPARTAN without the third stage rocket is 14.52m along the body length. The centre of gravity of the SPARTAN is varied as fuel is depleted throughout the acceleration phase, as well as when the third stage rocket is released. A point mass model is used in conjunction with the aerodynamic database, and atmospheric properties obtained from the U.S Standard Atmosphere 1976[26]. The SPARTAN is assumed to be trimmed at all conditions during flight. The trimmed aerodynamics of the SPARTAN are determined by modelling the flaps at deflected states of  $-20^\circ$ ,  $-10^\circ$ ,  $10^\circ$ , and  $20^\circ$ . Each of these deflected states were modelled in CREO and a surface mesh was created in Pointwise.

The aerodynamics at each flap deflection were calculated at  $0^\circ$  angle of attack for Mach numbers between 0.2 and 10. For each aerodynamic data point of Mach numbers between 0.2 and 10, and angle of attacks from  $0^\circ$  to  $10^\circ$ , the necessary flap deflection are calculated, and the additional lift and drag produced by the flaps are added. The addition of trimmed aerodynamics is calculated for scramjet engines on, and engines off conditions. Due to centre of gravity variation, the trim analysis is calculated three times; at the beginning of SPARTAN acceleration; at the end of SPARTAN acceleration, when fuel has been depleted; and after the third stage has been released. The trimmed aerodynamic databases at the beginning and end of acceleration are interpolated between as the centre of gravity varies due to fuel depletion. After the third stage is released, the centre of gravity is kept constant, and a single trimmed aerodynamic database is used.

Figure 3.10 shows the necessary flap deflections to trim the SPARTAN. An Engine-on case is shown at a centre of gravity of XXm corresponding to full-fuel with third stage, and an Engine-off case is shown for a centre of gravity of XXm, corresponding to a fuel-empty state after third stage release. Additional figures illustrating the variation in moment coefficients are shown in Appendix XX. The flap deflections are designated as negative up. Negative flap deflection necessary for trim indicates that the centre of pressure is aft of the centre of gravity, and that the vehicle has positive static margin, and is generally likely to be stable.

*The stability of the SPARTAN will be mentioned here when the final aerodynamics are calculated. The effect of each trim map, how it impacts lift etc. will be detailed.*

## Database Generation

The trimmed aerodynamic databases of the SPARTAN are generated in full prior to trajectory simulation to improve the computational efficiency of the simulation. The aerodynamic coefficients of lift, drag and moment are tabulated, and these tables are interpolated between during simulation. The process for generating the aerodynamic databases is shown in Figure 3.11. An initial surface triangulation of the SPARTAN is created in Pointwise, shown in Figure 3.12. This is then imported into CART3D as a watertight surface.

Following simulation in CART3D over the required flight conditions, the aerodynamic databases were generated. The simulation files are processed using Clic, a subprogram of CART3D used to calculate aerodynamic forces and moments, given surface pressure distributions. The solutions were processed for the necessary centre of gravity positions. At each flight conditions data point, and for each centre of gravity position, the necessary flap deflection for trim are calculated. The additional lift and drag generated by the flap are added to the untrimmed aerodynamics to create a trimmed database.

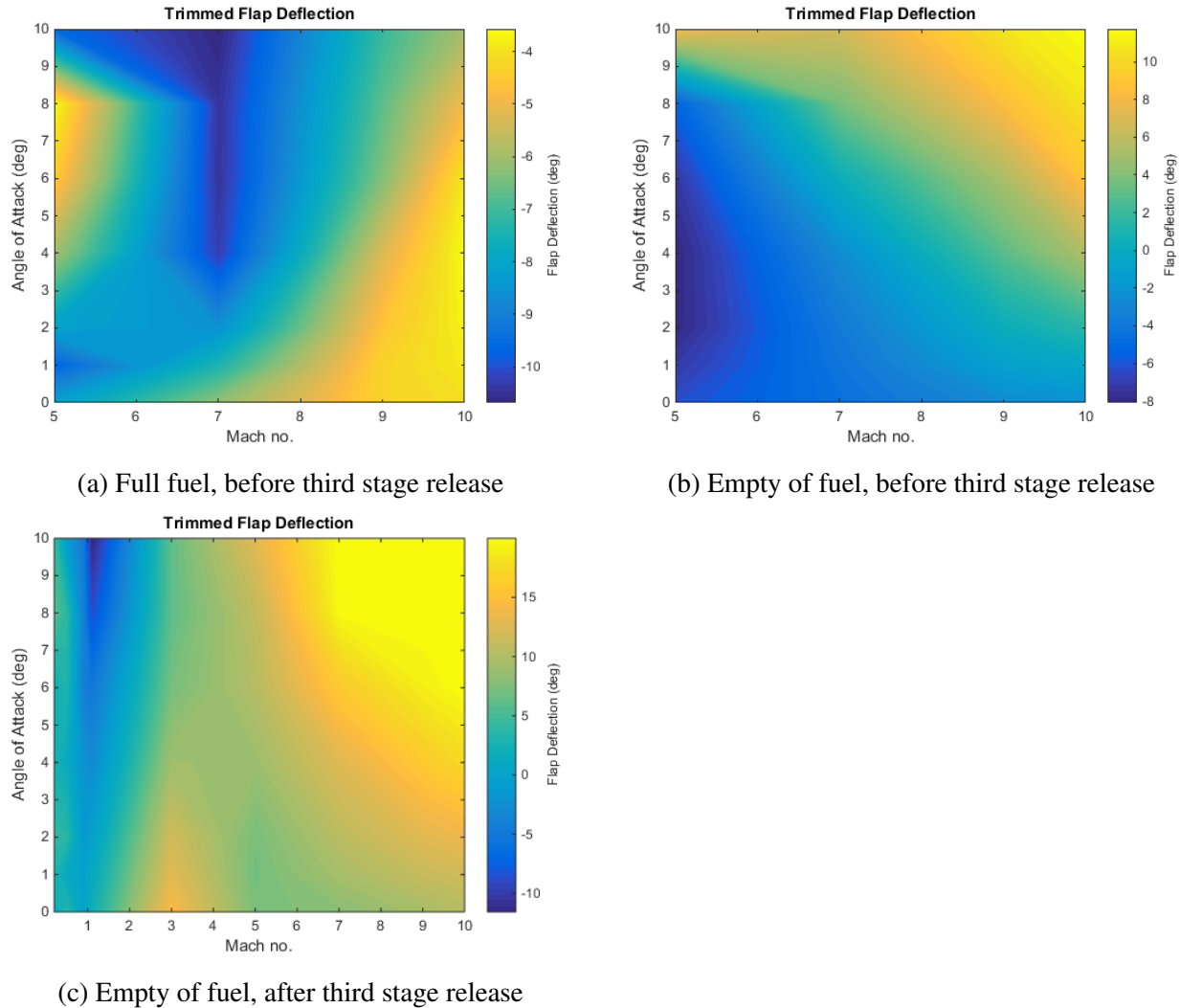


Figure 3.10: Flap deflection required for trim of the SPARTAN. Negative up. *These images will be modified when the final aerodynamics are calculated. The colourmap will be modified to have the same range across figures.*

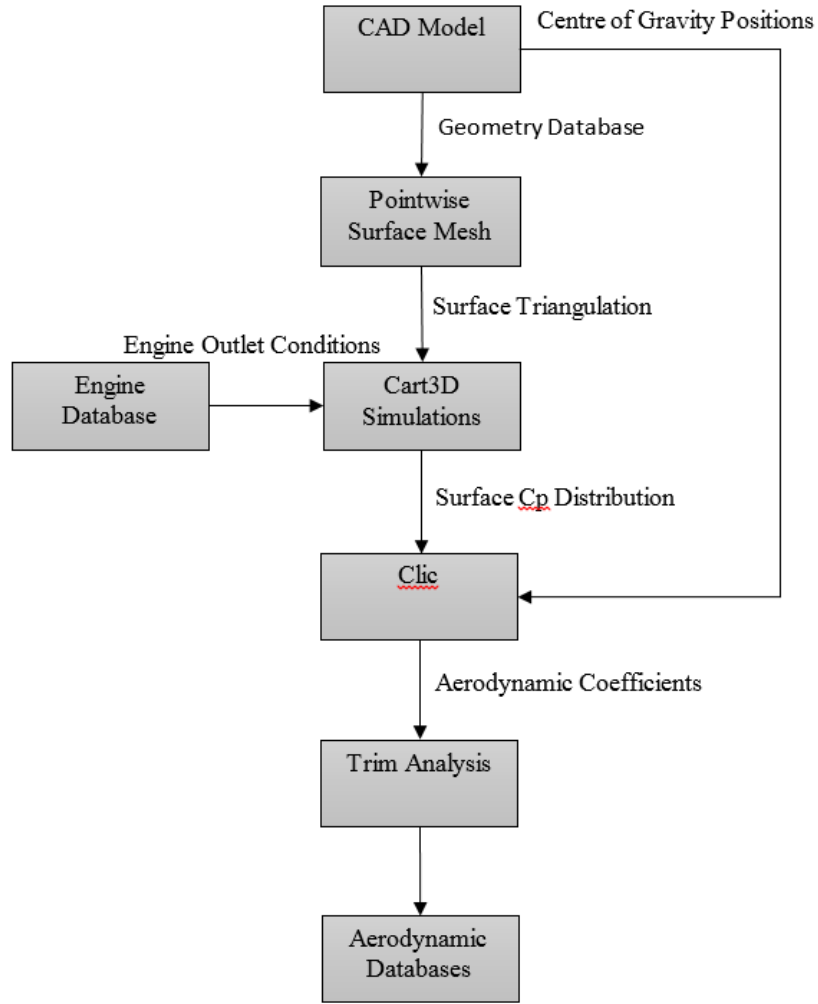


Figure 3.11: Process for generating aerodynamic databases.

### Engine-On Aerodynamics

The engine-on aerodynamics of the SPARTAN are used during the simulation of the acceleration phase, when the C-REST engines are operational at all times, as well as during the fly-back phase, when the engines are operational for a short time to aid the SPARTAN in returning to its initial launch site. The plumes of the SPARTAN are simulated using CART3D, using SurfBC boundary conditions which produce inflow and outflow conditions at the inlet and exit of the scramjet engines[85]. The exit conditions calculated by the CRESTM10 database, as defined in Section 3.1.2, are set as the outflow conditions for the CART3D surface. The scaled engine modelled in the CRESTM10 propulsion analysis has an exit area of  $0.5586\text{m}^2$ , smaller than the nozzle exit area on the SPARTAN, of  $0.9719\text{m}^2$ . To accommodate for this, the outflow surfaces are scaled to the exit area of the C-Rest engines simulated by quasi 1-D analysis, to ensure that the outflow conditions match the required nozzle position.

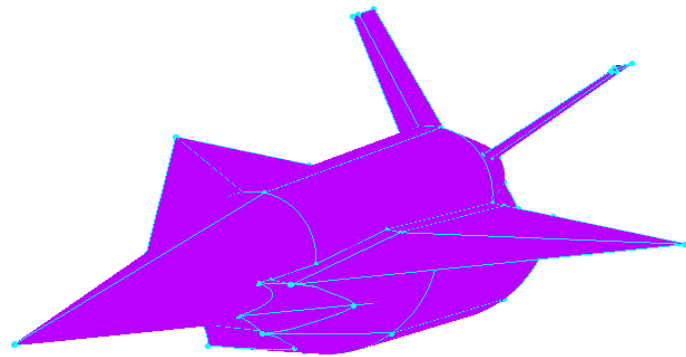


Figure 3.12: Surface triangulation of the Baseline SPARTAN. *This image will be recoloured.*

The outflow surfaces are positioned inside the nozzle on the SPARTAN model, so that the area of the outflow surface is  $0.5586\text{m}^2$ . The surface triangulation of the SPARTAN with outflow surfaces is shown in Figure 3.13. CART3D performs simulations nondimensionally, and requires the outflow

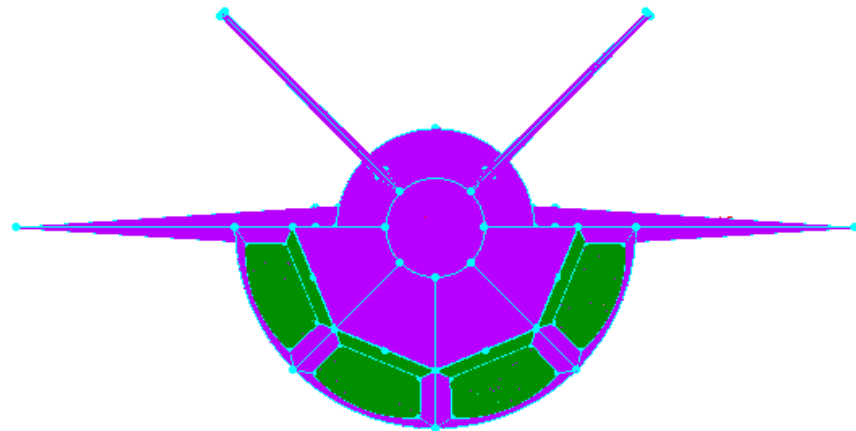


Figure 3.13: Pointwise view of the SPARTAN showing engine outlet boundaries.

conditions of a boundary to be normalised. The outflow conditions of  $P_e$ ,  $\rho_e$  and  $M_e$  given by the CRESTM10 propulsion model are normalised to CART3D nondimensionalised variables as follows CITATIONXX;

$$P_e^* = P_e / (\gamma_0 P_0), \quad (3.3)$$

$$\rho_e^* = \rho_e / \rho_0, \quad (3.4)$$

$$M_e^* = \sqrt{\gamma_e/\gamma_0} (M_e \sqrt{P_e^*/\rho_e^*})^2. \quad (3.5)$$

Where \* indicates the nondimensionalised input to CART3D. This nondimensionalisation includes a correction on the Mach number to account for  $\gamma_e$  variation, which is not possible to include directly in CART3D[74]. Engine-on aerodynamic calculations are performed for Mach numbers 5,7,9 and 10, and at altitudes from 20km to 40km. The plumes of the scramjet engines exit the nozzle of the SPARTAN, and are further expanded onto the boat tail on the rear of the SPARTAN fuselage, shown in Figure 3.14. This expansion causes significant force on the boat tail of the SPARTAN, generating additional lift, thrust and moment forces. The trimmed aerodynamics of the SPARTAN with C-REST engines on are shown in Figure 3.15.

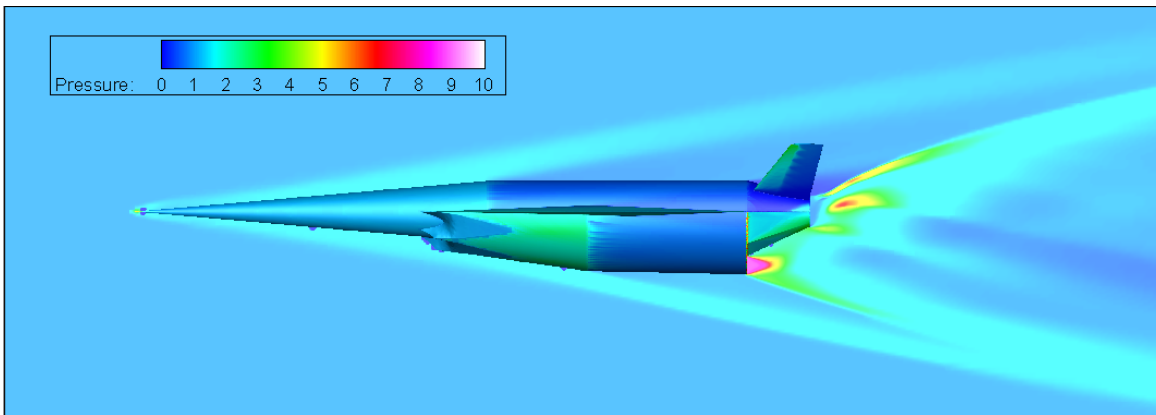


Figure 3.14: Engine-on CART3D simulation at Mach 7,  $6^\circ$  angle of attack, and 24km altitude. *The quality of these images will be improved.*

### Engine-Off Aerodynamics

During the majority of the return flight, the scramjet engines are not operational, and the SPARTAN is gliding without power. The return phase takes the SPARTAN from third stage separation, at approximately Mach 9, to landing approach at low subsonic speeds. While the engines are not powered on air flows through the flowpath without fuel injection, generating a large amount of drag. The aerodynamics of the SPARTAN are calculated using CART3D for Mach numbers from 0.2 to 10, and angle of attack values from  $0^\circ$  to  $10^\circ$  to cover the range of flight conditions experienced during the fly-back of the SPARTAN. An example CART3D solution is shown for a Mach 7 engine off condition in Figure 3.16. Figure 3.17 shows the engine off aerodynamic characteristics of the SPARTAN vehicle over the range of Mach numbers and angle of attack values analysed. These results show a distinct maximum region in the L/D of the SPARTAN at high Mach numbers, within the hypersonic regime. Below Mach 5, the L/D of the SPARTAN decreases sharply. This is caused by the scramjet engines unstarting, generating significant drag. The unstarted scramjet engines are shown in Figure

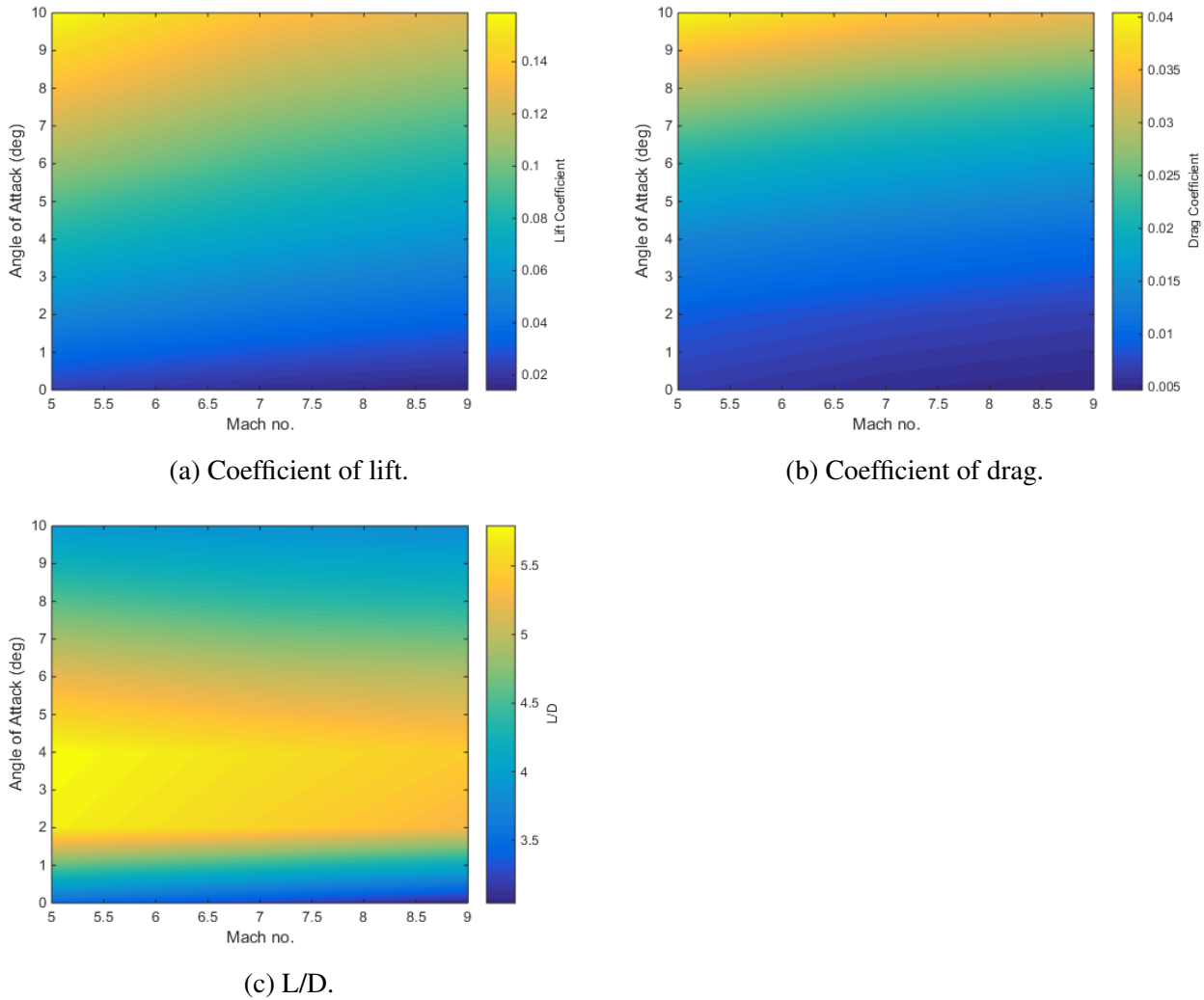


Figure 3.15: Trimmed aerodynamic coefficients with the C-REST engines powered on. Coefficients correspond to a reference area of  $62.77\text{m}^2$ .

[3.18.](#)

## 3.2 First Stage Rocket

The first stage rocket is required to deliver the second stage to near horizontal flight at Mach 5.1 flight conditions, after which it is discarded. To achieve this, the first stage rocket is modelled as a Falcon-1e first stage scaled down lengthwise to 9.5m, keeping the original diameter of 1.67m[CITATIONXX]. The Falcon-1e has been chosen due to its appropriate scale, and the proven flightworthiness of the Falcon-1. The first stage is attached to the rear of the scramjet second stage and is powered by a single LOX-kerosene Merlin 1-C engine. A connecting cowl has been modelled between the first stage rocket and the SPARTAN to improve the aerodynamic profile. The first stage has a structural

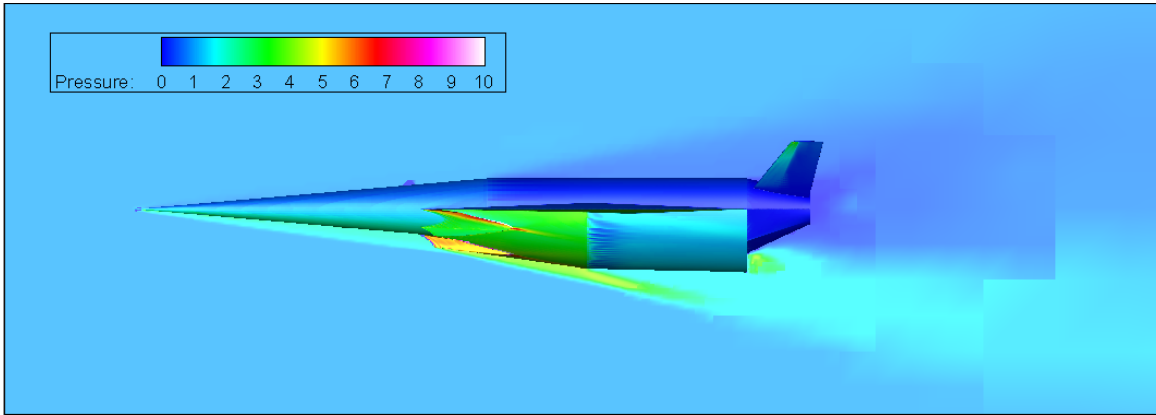


Figure 3.16: CART3D flow result for the SPARTAN, at Mach 7,  $6^\circ$  angle of attack.

mass of 1356kg, determined by scaling of the structural mass of the Falcon-1e. The engine mass of the Merlin 1-C is kept constant during scaling at 630kg[CITATIONXX]. The mass of the fuel in the first stage is scaled as part of the optimisation routine, as the dynamics of the vehicle, and its ability to reach a given separation point, are very closely coupled to the available fuel mass.

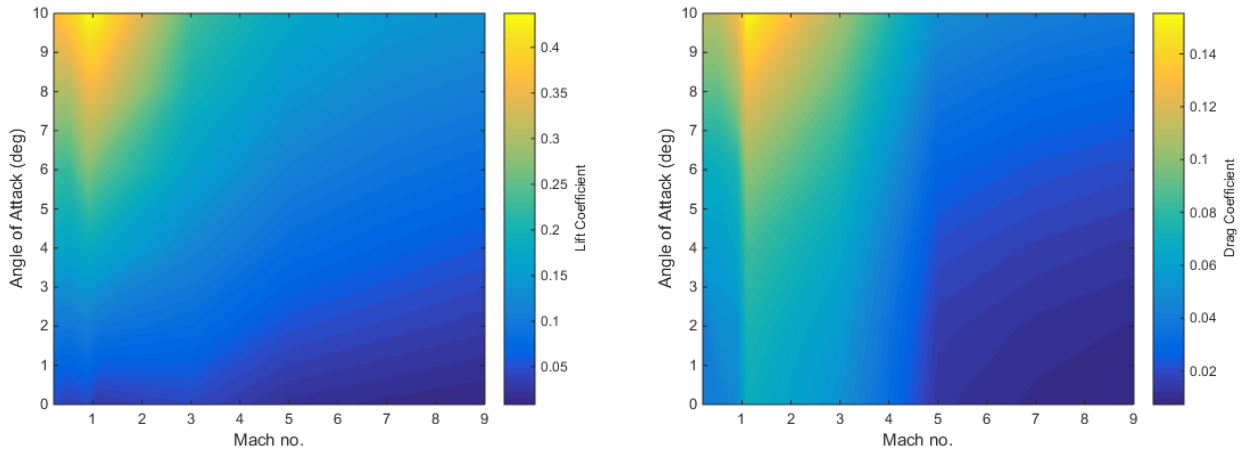
The thrust and specific impulse of the Merlin 1-C are determined by interpolation between the sea level and vacuum specific impulse of the Merlin 1-C, shown in Table 3.2, with pressure. Thrust scaling is determined by linear pressure scaling using nozzle exit area,  $T = T_{SL} + (p_e - p_{SL})A_e$ . The Merlin 1-C is throttled down to a constant 85% to allow the first stage to pitch over more easily.

$I_{SP_{SL}}$	275s
$I_{SP_{vac}}$	304s
$T_{SL}$	555.9kN
$A_e$	$0.552m^2$

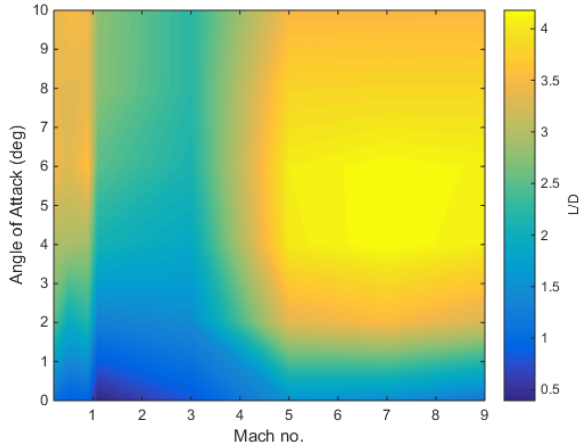
Table 3.2: First Stage Engine Properties [CITATIONXX].

### 3.2.1 Aerodynamics Including First Stage

The aerodynamics of the launch system during first stage flight are calculated in a similar manner to those of the SPARTAN without the first stage rocket, as detailed in Section 3.1.3. The aerodynamics of the SPARTAN and first stage rocket are calculated using CART3D. The first stage aerodynamics are modelled between angles of attack of  $0^\circ$  to  $-5^\circ$ , as the first stage will be flying at negative angle of attack to induce faster pitch-over. Mach numbers from 0.2 to 5.1 (second stage separation velocity) are simulated. Figure 3.19 shows an example CART3D simulation case, at Mach 2,  $-1^\circ$  angle of attack. The coefficient of lift, drag and aerodynamic moment are tabulated for each simulation. Figure 3.20 shows the lift and drag coefficients of the first stage, as well as the lift-over-drag, across the simulated Mach Numbers and angles of attack. Before the trajectory is simulated, the launch vehicle is trimmed



(a) Coefficients of lift of the SPARTAN, calculated using CART3D. (b) Coefficients of drag of the SPARTAN, calculated using CART3D.



(c) L/D of the SPARTAN.

Figure 3.17: Trimmed aerodynamic Characteristics of the SPARTAN with C-REST engine powered off. Coefficients correspond to a reference area of  $62.77\text{m}^2$ .

using the ailerons of the SPARTAN. The simulations of the SPARTAN with flap deflections between  $-20^\circ$  and  $20^\circ$  are used to calculate the deflection necessary to trim the vehicle, as described in Section 3.1.3, and the additional lift and drag generated by the ailerons is added to the aerodynamic database of the first stage launch vehicle.

### 3.3 Third Stage Rocket - Baseline

The third stage has a total length of 9m, with a 3m long nose, 4.5m long centrebody and 1.5m long engine. In this study the third stage rocket has been designed to accommodate a SpaceX Kestrel engine. In previous studies, the third stage has been designed to be powered by a Pratt & Whitney

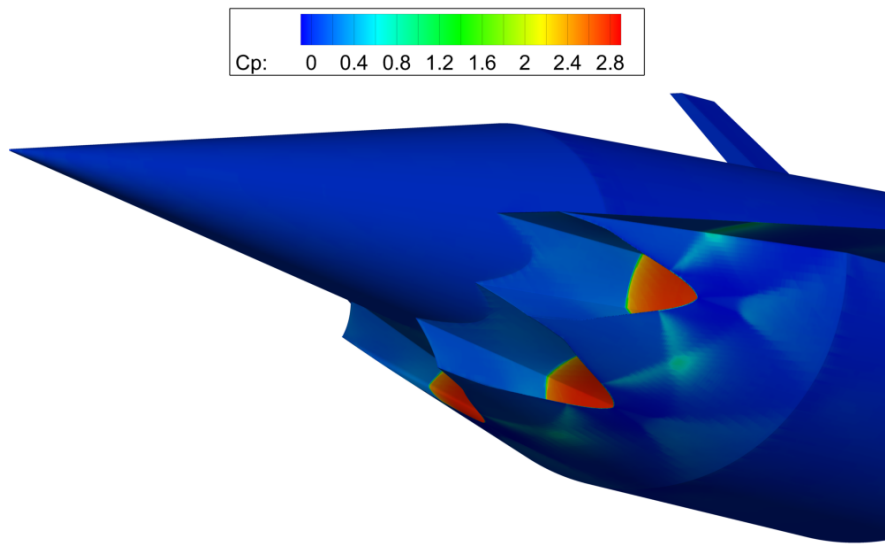


Figure 3.18: Unstarted scramjet engines at mach 3,  $2^\circ$  angle of attack.

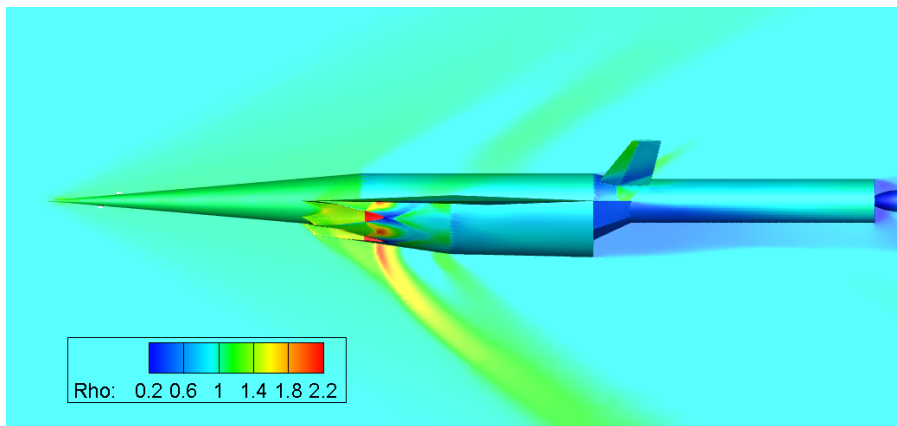


Figure 3.19: CART3D result for the SPARTAN and first stage vehicles at Mach 2,  $-1^\circ$  angle of attack.

RL-10-3A pump-fed engine. The Kestrel has been used over the RL-10-3A for its cost effectiveness. As a pressure-fed engine, the Kestrel trades off specific impulse for weight and cost savings when compared to the RL-10-3A. As the only expendable portion of the system; the cost of the third stage is one of the main drivers of overall system cost. Reducing the cost of the third stage allows the cost of launch to be directly reduced.

The third stage rocket is released at the end of the scramjet accelerator burn, and lifts the payload out of the atmosphere and into the desired orbit. The third stage weighs a total of 3300kg. This has been chosen as a nominal design weight, to satisfy the fuel necessary to achieve orbit with an acceptable payload, while also allowing for ample payload volume. The internal layout of the third stage rocket is shown in Figure 3.21. The third stage has a structural mass fraction of 0.09, similar to the Falcon 1 second stage [119]. This gives a total structural mass (without heat shield) of 285.7kg.

The kestrel engine used in the third stage is modified to have 50% increased propellant mass flow

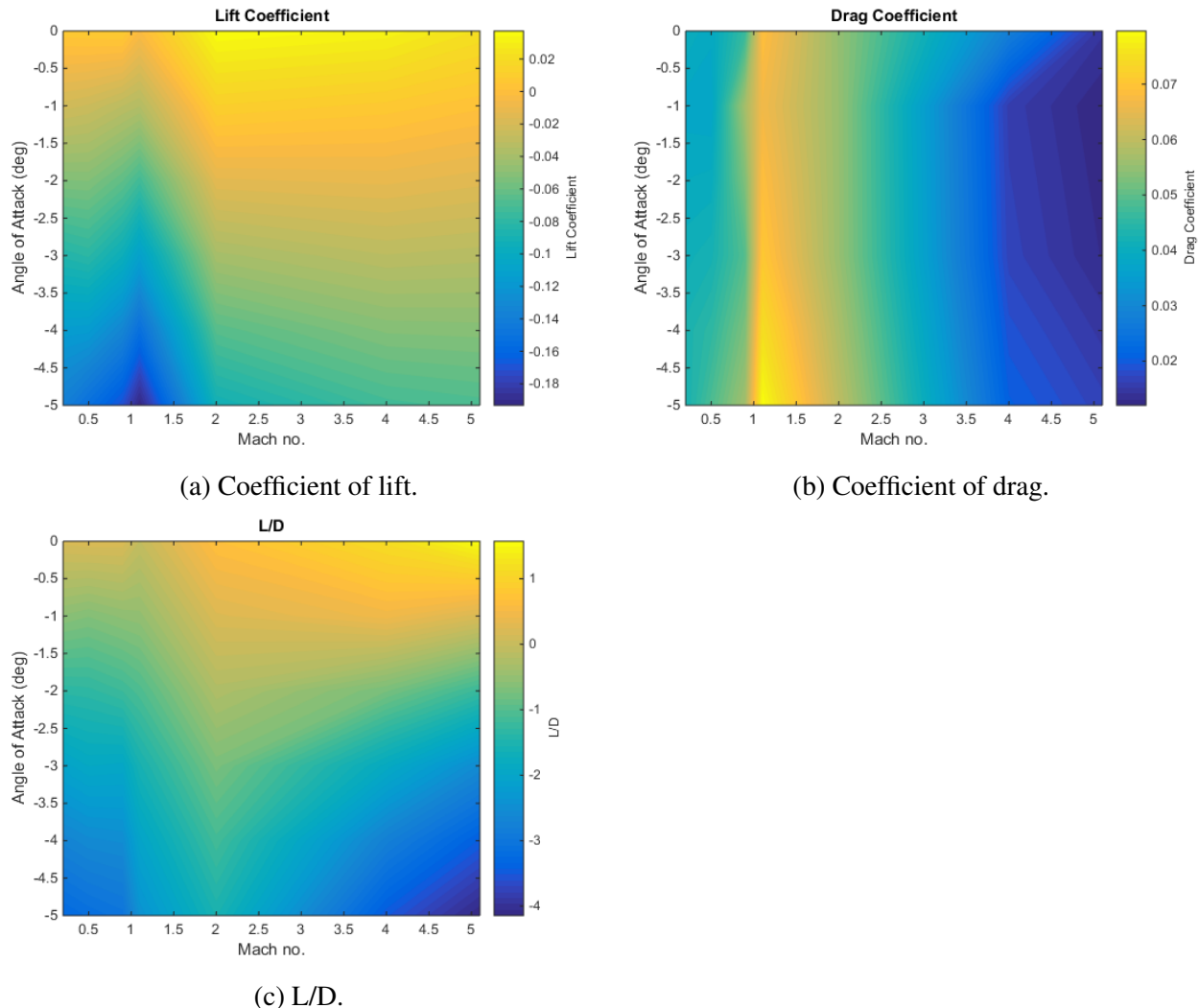


Figure 3.20: Aerodynamic characteristics of the SPARTAN including the first stage rocket.



Figure 3.21: The third stage rocket, showing major internal features. *Labels to be added.*

rate, giving a mass flow rate of 14.8kg/s. The nozzle exit of the Kestrel engine has been kept constant at 1.1m diameter. An increase in mass flow necessitates a corresponding increase in throat area. This increase in throat area decreases the area ratio of the nozzle. The initial area ratio is 60, measured from schematics in the Falcon-1 Users Guide. A 50% mass flow increase corresponds to a 50% throat area increase, which causes the area ratio to decrease to 40. This decrease in area ratio results in a 2% loss of efficiency from the nozzle, measured from the thrust coefficient relationships shown in Figure 3.22[122]. The coefficient of thrust is calculated for a specific heat ratio of 1.20, as this is close to the specific heat ratio of oxygen and RP-1 of 1.24[122]. The modified specific impulse of the engine is 310.7s.

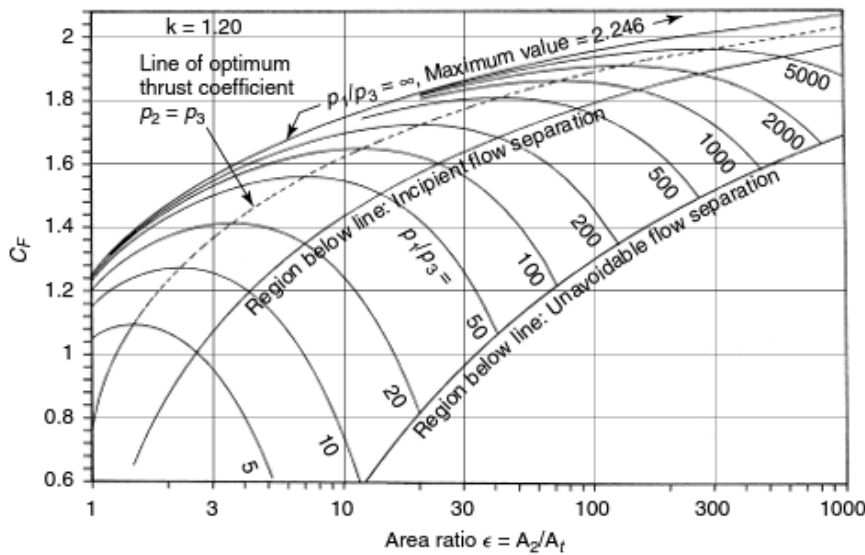


Figure 3.22: Variation in coefficient of thrust with area ratio [122].

### 3.3.1 Heat Shield Sizing

The third stage rocket is separated from the SPARTAN at a high dynamic pressure, after which it spends a considerable amount of time accelerating in-atmosphere before reaching exoatmospheric conditions. The time spent within a high dynamic pressure environment creates a large amount of heat loading, which must be mitigated by heat shielding. The heat shielding must be capable of withstanding the extremely high heat and structural loading necessary to protect the third stage rocket internals and payload, as well as being lightweight, as the payload-to-orbit is extremely sensitive to the mass of the third stage, and cost effective, as increasing the cost of the third stage directly increases launch cost due to it being expendable.

The heat shield used to protect the third stage is constructed from a tungsten nose tip, a reinforced carbon-carbon nose cone, and a phenolic cork cylinder, weighing 130.9kg in total. This heat shield is designed based on the materials and thicknesses defined in[93]. A mass breakdown is shown in

Table 3.3. Tungsten is used at the tip of the nose cone, the area of maximum heat loading. Tungsten has extremely high heat resistivity, and a very low coefficient of thermal expansion[CITATIONXX]. However, tungsten is costly and heavy, and is only used on the very tip of the nose where it is absolutely necessary. Reinforced carbon-carbon is used for the conical section of the heat shield, as this is an area that will be subject to high heat and structural loading. Carbon-carbon is able to withstand high temperatures, as well as being thermal shock resistant and having a low coefficient of thermal expansion[36]. Carbon-carbon is used in rocket and missile nose cones, as well as on aircraft leading edges due to its good heat resistant properties[36]. However, carbon-carbon is expensive, and is used only on the conical section of the heat shield to minimise cost. For the cylindrical section of the heat shield protecting the main body of the third stage, phenolic cork is used. Phenolic cork is a composite of ground cork and phenolic binders which is light and relatively cheap, with good heat resistivity. Phenolic cork has lower tensile strength and heat resistivity than carbon-carbon[20, 36], but is cheaper and lighter, making it appropriate for use on section of the heat shield which experiences lower heating and structural loads.

Part	Density	Geometry	mass
Tungsten Nose	$\rho_{Tungsten} = 19250 \text{ kg/m}^3$	50mm diameter cylinder, spherical tip	12.6kg
C-C Cone	$\rho_{CC} = 1800 \text{ kg/m}^3$	10mm thick, conical	93.4kg
Phenolic Cork Cylinder	$\rho_{PhenolicCork} = 320 \text{ kg/m}^3$	5mm thick, cylindrical	24.9kg

Table 3.3: Third stage heat shield breakdown.

### 3.3.2 Fuel Tank Sizing

The internal design of the third stage is allowed to be slightly variable as the trajectory is optimised. The third stage mass is fixed at 3300kg, and the calculated payload-to-orbit varies by exchanging leftover fuel mass for effective payload mass. To calculate the dynamics of the third stage, the fuel tanks have been approximately sized, assuming 160kg of payload-to-orbit. Realistically the exchange between fuel and payload mass would cause the fuel tanks to be resized slightly. For the purposes of this study the fuel tanks are assumed to be of constant size for simplicity. Currently this is a reasonable assumption as the internals of the rocket are very simplified. The structural mass is held constant at 9%. The third stage carries a total propellant mass of 2736.7kg. Table 3.4 breaks shows the component break-down of the LOX oxidiser and RP1 fuel.

### 3.3.3 The Aerodynamics of the Third Stage Rocket

The third stage aerodynamics have been calculated using Missile DATCOM [REFXX], a preliminary design tool for estimating the aerodynamic characteristics of missile and rocket vehicles. Missile DATCOM utilises empirical methods, along with various estimation techniques, to compute the

	<b>LOX</b>	<b>RP1</b>
Ratio	2.56	1
Density	1141kg/m3	813kg/m3 [73]
Volume	1.7248m3	0.9455m3
Mass	1968.0 kg	768.7 kg

Table 3.4: Third stage fuel distribution.

aerodynamics of missile-like vehicles across the subsonic, supersonic and hypersonic regimes. The aerodynamics of the third stage rocket are shown in Figure 3.23. The code used to compute the aerodynamics of the third stage rocket is detailed in Appendix XX.

### Thrust Vectoring

The third stage rocket is controlled via thrust vectoring. The centre of pressure is calculated using missile DATCOM. The thrust vector is set so that the moment generated by the engine matches the lift force acting at the centre of pressure, shown in Figure 3.24. The maximum thrust vector limit has been set to  $8^\circ$ . As no data on the maximum thrust vectoring capabilities of the kestrel engine was able to be found, this was set to the maximum gimbal range of the Aestus pressure-fed engine and OMS, similar pressure fed engines CITATIONXX.

The centre of gravity is determined using CREO, and is at XXm from the nose. It is assumed that the mass of the structure of the rocket (excluding fuel tanks, heat shielding, engine and payload) is distributed homogeneously for simplicity. The third stage rocket is statically unstable. Flying this rocket at an angle of attack will require an advanced automatic controller, as the only control available is produced by thrust vectoring. This study assumes that the third stage rocket is able to be controlled over any required trajectory, as long as the thrust vector limits of the vehicle are not exceeded.

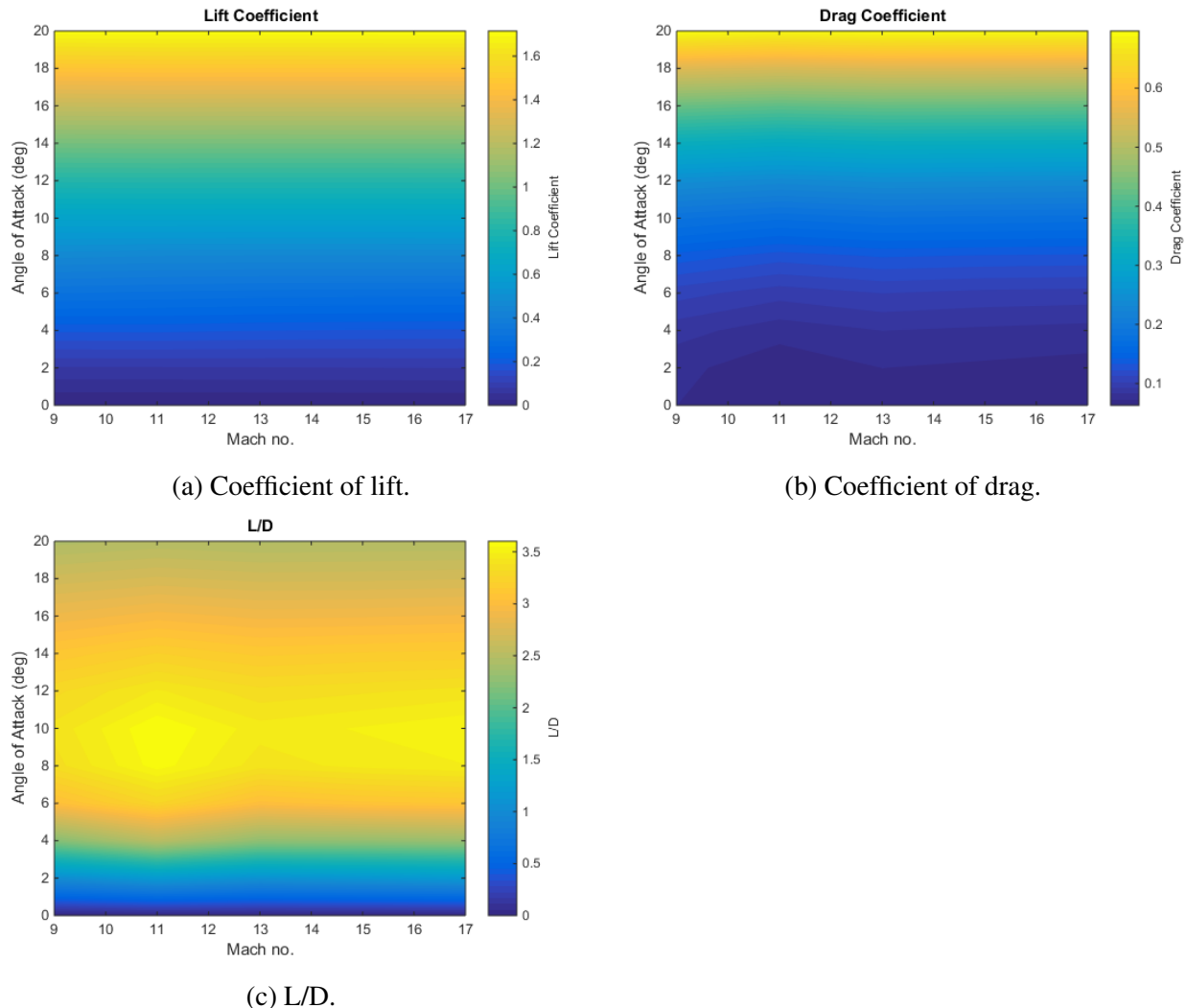


Figure 3.23: Aerodynamic characteristics of the baseline third stage rocket, for a reference area of  $0.95\text{m}^2$ .

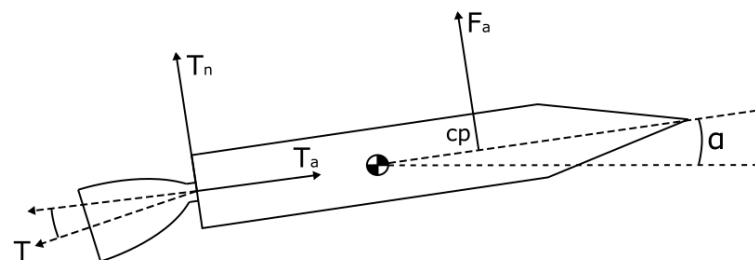


Figure 3.24: Thrust vector force balance.

---

---

## CHAPTER 4

---

### LODESTAR

This chapter covers the optimal control program LODESTAR (Launch Optimisation and Data Evaluation for Scramjet Trajectory Analysis Research), which has been used to simulate the optimal trajectories of the rocket-scramjet-rocket system. The dynamic model and structure of LODESTAR are presented, as well as the set-up of LODESTAR for the rocket-scramjet-rocket trajectory optimisation, and the validation methods used to determine if a solution has converged correctly.

LODESTAR has been developed to aid with the simulation and trajectory optimisation of space launch systems. LODESTAR is MATLAB based and utilises GPOPS-2, a proprietary pseudospectral method optimisation package. LODESTAR optimises a trajectory towards a user-defined objective function, such as maximum payload-to-orbit, subject to constraints which bound the operational region of a vehicle. Both rocket-powered and scramjet-powered vehicles are accurately modelled within LODESTAR in 6 degrees of freedom. LODESTAR contains multiple modes configured for the SPARTAN launch system, which are able to optimise trajectories for;

1. The ascent of the first stage rocket.
2. The ascent of the second stage scramjet-powered accelerator.
3. The flyback of the second stage scramjet-powered accelerator.
4. The ascent of the third stage rocket.
5. Combined trajectories of multiple stages in any combination.

Figure 4.1 illustrates a simplified iteration of the pseudospectral solver. Modules within LODESTAR calculate the vehicle aerodynamic and engine performance at each point along the trajectory, along with atmospheric conditions. This data is then used to calculate the dynamics of the vehicle along the

trajectory. The imposed constraints and cost are then evaluated to compute the feasibility and optimality of the solution. Based on this evaluation, the trajectory is then updated to a new iteration. This process repeats until the solver reaches a predefined tolerance of optimality. Due to the nature of the

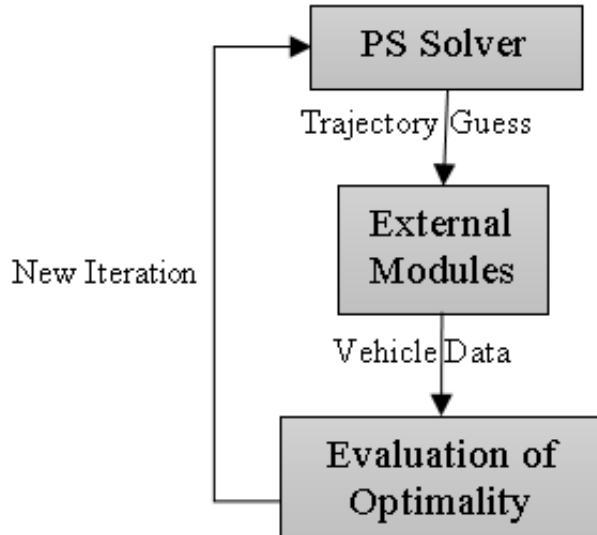


Figure 4.1: General work flow of the pseudospectral solver.

pseudospectral method, it is possible for GPOPS-2 to not be able to converge to a physically valid or optimal solution. LODESTAR contains a number of verification modules which assess the optimised trajectory solution to ensure that the solution is indeed an optimal trajectory, and that the dynamics of the solution are accurate.

## 4.1 Optimal Control Problem Structure

The pseudospectral method used by GPOPS-2 is described in detail in section 2.8. Practically, the implementation of optimal controls involves the specification of the dynamics of the system to be optimised, as well as the set of constraints and objectives which govern the optimisation problem. Together, these define the optimisation problem being solved. The states ( $\mathbf{x}$ ) and controls ( $\mathbf{u}$ ) are the variables which define the time dependent physical characteristics of the system. The state variables are dependent on the controls and the system dynamics, while the control variables are the variables which drive the behaviour of the system and are independently variable in the solution space.

### *Cost Function*

The cost function,  $J$ , defines the target of the optimisation problem. This cost function may be any function which is defined by the states or controls of the optimisation problem. The cost function is

defined as follows:

$$J(t, \mathbf{x}(t), \mathbf{u}(t)) = M[t, \mathbf{x}(t_f), \mathbf{u}(t_f)] + \int_{t_0}^{t_f} P[\mathbf{x}(t), \mathbf{u}(t)] dt, \quad t \in [t_0, t_f], \quad (4.1)$$

where  $M$  is the terminal cost function and  $P$  is the time integrated cost.

### *Dynamic Constraints*

The constraints impose various conditions on the optimisation problem. The optimisation problem is subject to a set of dynamic constraints, which describe the behaviour of the system over the solution space:

$$\dot{\mathbf{x}}(t) = f[t, \mathbf{x}(t), \mathbf{u}(t)]. \quad (4.2)$$

Implementing the dynamics as constraints allows each state variable to be approximated separately, and gives the optimiser some freedom to explore each state variable independently, greatly increasing the robustness of the optimal control problem. However, implementing the dynamics as constraints means that the dynamics do not have to be physically valid at all times during the process of searching for an optimal solution. A violation of the physical dynamics constraints can cause potential complications for the computational model of the vehicle. Much of the design of the vehicle model in this study is driven by the need for smooth, continuous interpolation schemes, which cover the entire possible operational range of the vehicle, ie. even if the solution is well within the range of all input data sets, the solver must be able to explore all regions within the set bounds.

### *Bounds and Path Constraints*

Inequality constraints define the bounds of each state, as well as any path constraints. The bounds directly confine the state and control variables to prescribed values. This serves the purpose of limiting the search space to the physically possible (eg. constraining altitude to be greater than ground level), constraining the vehicle within its performance limits (eg. limiting the angle of attack), and improving computational efficiency by ensuring that the optimiser is constrained to a reasonable solution space:

$$\mathbf{b}_{min} \leq \mathbf{x}(t), \mathbf{u}(t) \leq \mathbf{b}_{max}. \quad (4.3)$$

The path constraints are inequality constraints which consist of functions based on the states and controls of the system. Path constraints are generally used to impose physical limitations on the system such as structural, aerothermodynamic or pathing limitations:

$$\lambda[t, \mathbf{x}(t), \mathbf{u}(t)] \leq \mathbf{0}. \quad (4.4)$$

### *Event Constraints*

The event constraints define the states at the start and end points of a trajectory or phase:

$$\psi_0[\mathbf{x}(t_0), t_0] = \mathbf{0}, \quad (4.5)$$

$$\psi_f[\mathbf{x}(t_f), t_f] = \mathbf{0}. \quad (4.6)$$

These constraints determine the initial and terminal conditions of the optimisation problem. Additionally, if the problem has multiple phases, these constraints are used to couple the states and time of each phase to the preceding and following phases as follows:

$$\mathbf{x}_{f,1} - \mathbf{x}_{0,2} = \mathbf{0}, \quad (4.7)$$

$$\mathbf{t}_{f,1} - \mathbf{t}_{0,2} = \mathbf{0}. \quad (4.8)$$

### 4.1.1 GPOPS-2 Example - Brachistochrone Problem

This section describes a short example of an optimal control problem solved in GPOPS-II. The purpose of this example is to demonstrate the effectiveness of the pseudospectral method and GPOPS-II, and to provide a simple example case to establish the terminology of an optimal control problem.

The brachistochrone (from the Greek for 'shortest time') problem is a simple optimal control problem, which describes a ball rolling in two dimensions under gravity. The objective is to find the curve of descent which will minimise the time from point *a*, where the ball is at rest, to point *b*. It is assumed that gravity is constant and that there is no forces other than gravity acting on the ball. The analytical solution of this problem can be computed using the Euler-Lagrange equation as the equations describing a cycloid:

$$x = A(\theta + \sin \theta),$$

$$y = A(1 - \cos \theta)$$

This problem is included within GPOPS-2 as an example problem, and has been solved to illustrate the GPOPS-2 solution set-up[cite Gpops XX]. Table XX describes the set-up of the optimal control problem in GPOPS-2. The dynamic equations for the Brachistochrone problem are:

$$\dot{x} = v * \cos(u),$$

$$\dot{y} = v * \sin(u),$$

$$\dot{v} = g * \sin(u).$$

These equations are provided to GPOPS-2 as the time-variant system model in this form. The control variable is set to be the descent angle. The initial constraints are defined to initiate the ball at rest at the origin, and the terminal constraints are defined to terminate the problem at coordinates of XX XX. The cost is set to minimum time, so that the solution will be the descent angle which minimises the time to get from the initial position, to the end position.

Primal Variables	x Position y Position Velocity
Control Variables	Angle of Descent
Initial Constraints	Velocity x Position y Position
Terminal Constraints	x Position y Position
Path Constraints	None
Target Cost	Minimum Time

The GPOPS-2 solution to the Brachistochrone problem is shown in Figure 4.2, matching the analytical solution almost exactly. This is expected in this case, as the dynamics of the basic Brachistochrone problem are very simple. As the dynamics become more complex, it is no longer possible to obtain an analytical solution. For more complex problems, various methods must be used to verify the optimal solution. These methods are outlined later in this chapter, in Section XX.

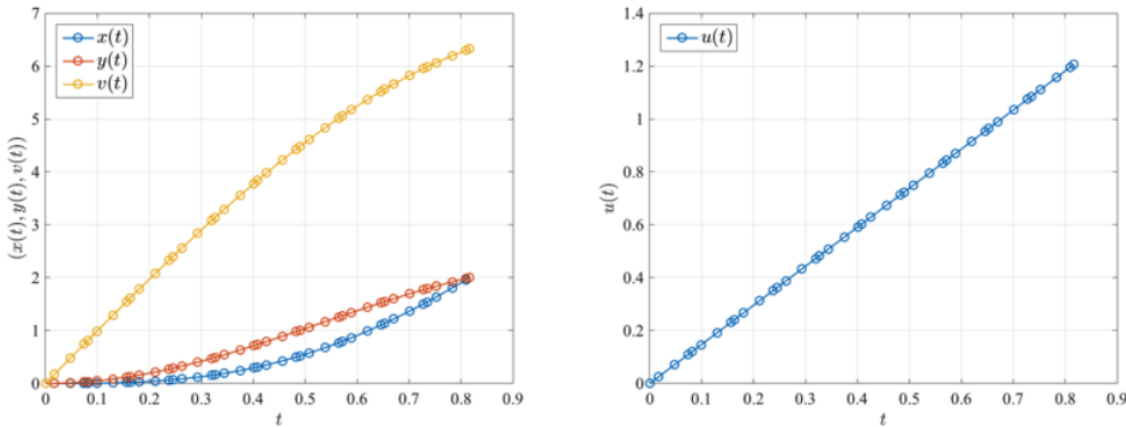


Figure 4.2: The solution to the brachistochrone problem, solved in GPOPS-2[CITATIONXX].

## 4.2 Rocket-Scramjet-Rocket Trajectory Optimisation

LODESTAR contains a variety of modules used to calculate a trajectory optimisation of a rocket-scramjet-rocket launch vehicle for maximum payload-to-orbit. These modules calculate the vehicles aerodynamic properties and run external simulations which then feed data back to the pseudospectral solver for evaluation. Figure 4.3 shows the information flow within LODESTAR.

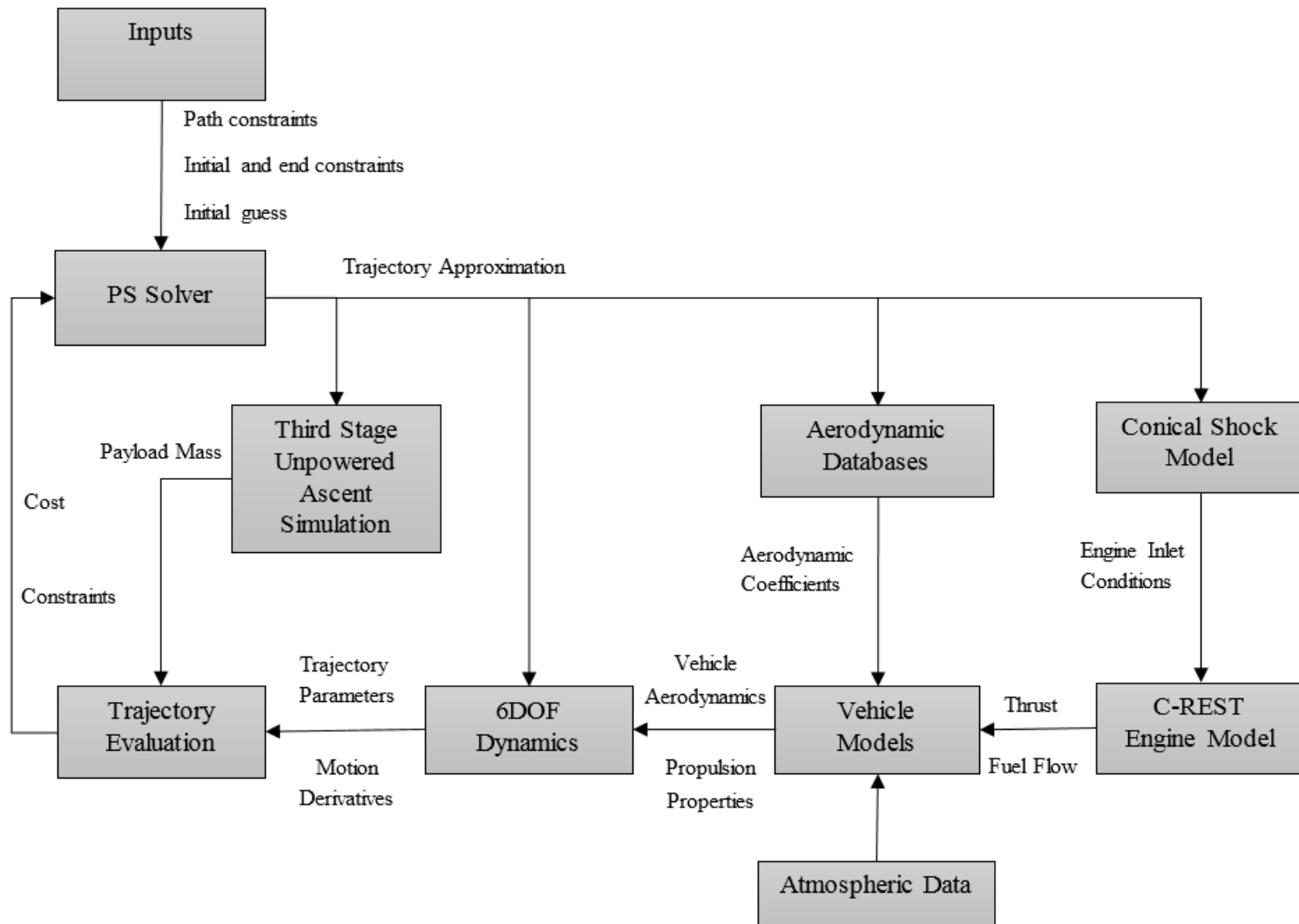


Figure 4.3: The process of the rocket-scramjet-rocket trajectory optimisation.

### 4.2.1 Dynamic Model

The dynamics of the vehicle are calculated in six degrees of freedom, with yaw constrained to zero. The dynamics of all stages are calculated using an geodetic rotational reference frame, written in terms of the angle of attack  $\alpha$ , bank angle  $\eta$ , radius from centre of Earth  $r$ , longitude  $\xi$ , latitude  $\phi$ , flight path angle  $\gamma$ , velocity  $v$  and heading angle  $\zeta$ . The equations of motion are [57]:

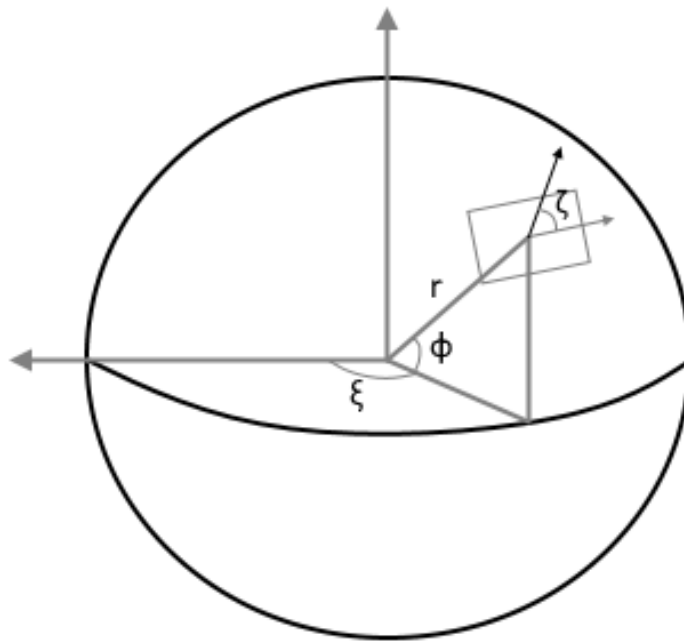


Figure 4.4: The Earth-fixed components of the geodetic rotational coordinate system.

$$\dot{r} = v \sin \gamma \quad (4.9)$$

$$\dot{\xi} = \frac{v \cos \gamma \cos \zeta}{r \cos \phi} \quad (4.10)$$

$$\dot{\phi} = \frac{v \cos \gamma \sin \zeta}{r} \quad (4.11)$$

$$\dot{\gamma} = \frac{T \sin \alpha \cos \eta}{mv} + \left( \frac{v}{r} - \frac{\mu_E}{r^2 v} \right) \cos \gamma + \frac{L}{mv} + \cos \phi [2\omega_E \cos \zeta + \frac{\omega_E^2 r}{v} (\cos \phi \cos \gamma + \sin \phi \sin \gamma \sin \zeta)] \quad (4.12)$$

$$\dot{v} = \frac{T \cos \alpha}{m} - \frac{\mu_E}{r^2} \sin \gamma - \frac{D}{m} + \omega_E^2 r \cos \phi (\cos \phi \sin \gamma - \sin \phi \cos \gamma \sin \zeta) \quad (4.13)$$

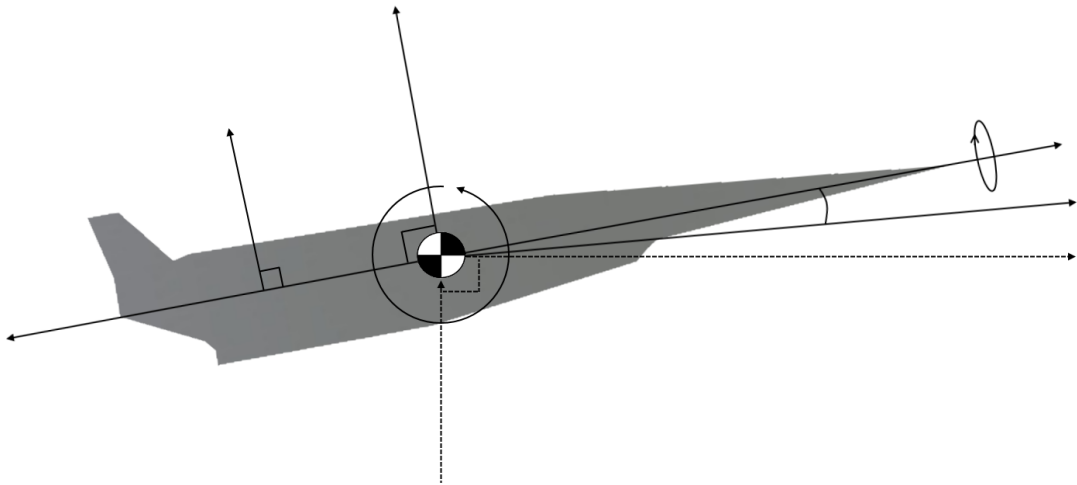


Figure 4.5: The vehicle-based components of the coordinate system.

$$\dot{\zeta} = \frac{T \sin \alpha \sin \eta}{mv \cos \gamma} - \frac{v}{r} \tan \phi \cos \gamma \cos \zeta + 2\omega_E \cos \phi \tan \gamma \sin \zeta - \frac{\omega_E^2 r}{v \cos \gamma} \sin \phi \cos \phi \cos \zeta - 2\omega_E \sin \phi \quad (4.14)$$

### 4.2.2 Trajectory Connection Points

The optimisation of a large, multi-vehicle launch trajectory requires that the optimal control problem be broken down into multiple segments. This segmentation is performed in order to assist the convergence of the optimal control solver, by ensuring that the dynamics of the underlying model are as smooth and continuous as possible across each segment. For a launch system, discontinuities in the system dynamics generally arise when the aerodynamics, mass and propulsion mode of a launch vehicle change significantly between stages or flight modes. If a vehicle model with large discontinuities is implemented directly into a single phase application of the pseudospectral method, it is likely to cause significant convergence issues, as the system dynamics will be unable to be approximated by the underlying polynomial of the pseudospectral method.

To allow the trajectory profile to be formulated as an optimal control problem, the trajectory of the rocket-scramjet-rocket launch system has been broken down into the seven segments shown in Figure 4.6. The segments have been separated into two groups; controlled segments which form the phases of the optimal control problem, and segments without control which are simulated separately, to increase computational efficiency and improve the convergence of the optimal control solver. Segments II-V are controlled by various combinations of angle of attack, bank angle and throttle, and are implemented as the phases of the optimisation problem. These phases are; The 1st stage pitching ascent; the 2nd stage ascent; the 2nd stage return flight; and the 3rd stage powered ascent. Segments I, VI and VII are segments without direct control, which are simulated using forward time stepping methods.

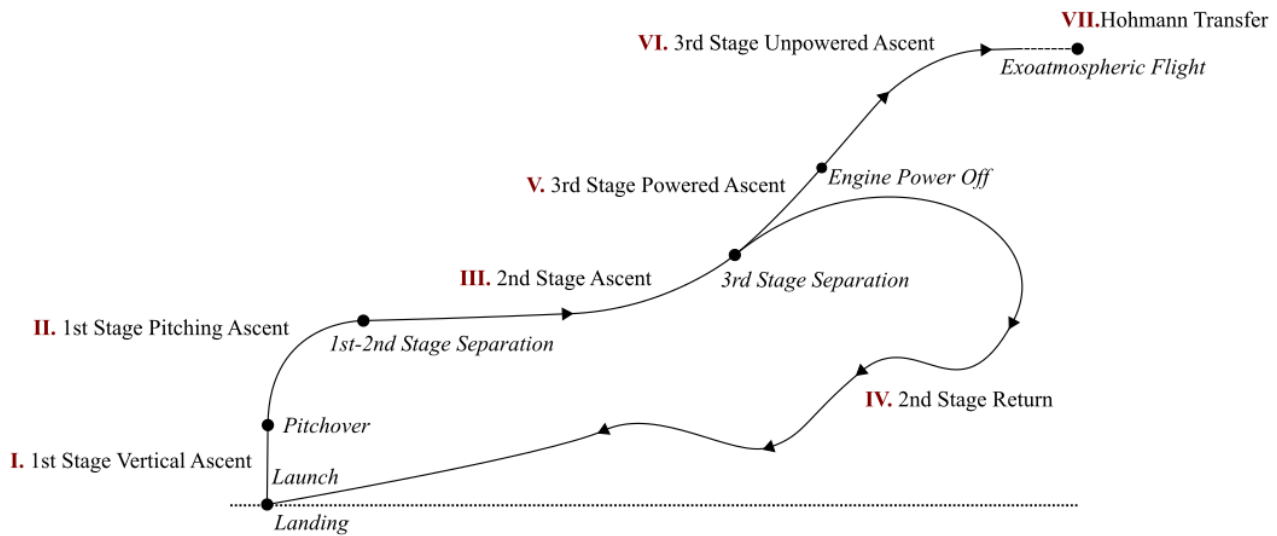


Figure 4.6: Illustration of the segmented launch profile.

These phases are; the pre-pitch segment of the first stage; the unpowered section of the third stage ascent; and the final Hohmann transfer to orbit. Each segment is connected through a set of conditions, which ensure that the trajectory of the vehicle is continuous, and that the trajectory that is being simulated is the one that is intended. The optimal control problem phases are connected through the use of initial and end discontinuity constraints on each phase to be coupled, ie  $\mathbf{x}_{f1} = \mathbf{x}_{02}, t_{f1} = t_{02}$ , while the forward simulated segments are simply initiated and terminated at set conditions. The segment coupling conditions are described in Table 4.1.

Section	Initial Conditions	End Conditions
1 <sup>st</sup> Stage Vertical Ascent (I)	Must start at rest, at the predefined launch site.	Fly until pitchover conditions are met.
1 <sup>st</sup> Stage Pitching Ascent (II)	Start at pitchover conditions	-
2 <sup>nd</sup> Stage Ascent (III)	Must begin at 1 <sup>st</sup> stage pitching ascent end conditions.	-
2 <sup>nd</sup> Stage Return (IV)	Must begin at 2 <sup>nd</sup> stage ascent end conditions.	Must approach landing conditions at the initial launch site.
3 <sup>rd</sup> Stage Powered Ascent (V)	Must begin at 2 <sup>nd</sup> stage ascent end conditions.	Must produce exoatmospheric flight at the termination of stage VI.
3 <sup>rd</sup> Stage Unpowered Ascent (VI)	Must begin at 3 <sup>rd</sup> stage powered ascent end conditions.	Terminates when flight is parallel with Earth's surface.
3 <sup>rd</sup> Stage Hohmann Transfer (VII)	Must begin at 3 <sup>rd</sup> stage unpowered ascent end conditions.	Must attain prescribed orbit.

Table 4.1: Segment coupling conditions for combined trajectory optimisation.

## I. First Stage Vertical Ascent

LODESTAR optimises the ascent of the first stage rocket in two sections; pre and post-pitchover. Initially, the first stage rocket is launched vertically, and continues vertically for a small amount of time, until pitchover is initiated. During the vertical launch the rocket is assumed to need no control, and is held at 0° angle of attack. The pitchover is defined to occur at 90m altitude and 30m/s velocity, rather than at a specific time. This allows the pre-pitchover phase to be simulated separately, after the optimisation has been completed. If the initial mass is variable, the pre-pitchover trajectory is calculated to match the pitchover mass, and the initial launch altitude will necessarily be slightly variable. This variation in launch altitude is small, on the order of ten meters or less.

## II. First Stage Pitching Ascent

The post-pitchover trajectory is an angle of attack controlled phase in the optimisation routine, which is simulated from pitchover until second stage separation. During this phase, the launch system is allowed to fly at negative angles of attack, to assist in pitching. The fuel mass of the first stage rocket is unconstrained. This approach is used on account of the selected first stage being able to reach the required range of altitudes and flight angles with only small fuel mass variations. Nevertheless, small variation in fuel mass can have an important effect on the capabilities of the first stage, influencing the velocity achievable at first to second stage separation, as well as the rate at which the rocket is able to

pitch, and consequentially, the altitude and flight path angle range of the first stage. It is useful in the preliminary design stages to be able to vary the mass of the first stage vehicle during the optimisation process, allowing a less trial-and-error approach than selecting a starting fuel mass manually.

Optimisation Parameter	Associated Variables	Allowable Values
Initial Constraints	Velocity	30m/s
	Altitude	90m
	Latitude	-12.16°
	Longitude	136.75°
	Trajectory Angle	89.9°
	Angle of Attack	0°
Terminal Constraints	$\mathbf{x}_{f\text{II}} - \mathbf{x}_{0\text{III}}$	0
	$t_{f\text{II}} - t_{0\text{III}}$	0
Path Constraints	Dynamic Pressure	0kPa - 50kPa
Control Variables	$\ddot{\alpha}$	
State Variables	Altitude	
	Velocity	
	Latitude	
	Longitude	
	Trajectory Angle	
	Heading angle	
	Total mass	
	Angle of Attack ( $\alpha$ )	-5° - 5°
	$\dot{\alpha}$	

Table 4.2: Optimisation setup of the first stage phase. **The other tables in this section will be modified to conform to this one. But I am currently unsure whether this table layout is clear.**

### 4.2.3 III. Second Stage Ascent Trajectory

The ascent trajectory of the SPARTAN is controlled using angle of attack, and bank angle. This trajectory is constrained to a maximum dynamic pressure of 50kPa, corresponding to the maximum structural limits of the vehicle. During the ascent, the engines are assumed to be operating at an equivalence ratio of 1 at all times.

Initial Constraints	Velocity Fuel Mass Latitude Longitude
Terminal Constraints	Fuel mass Heading Angle
Path Constraints	Dynamic Pressure
Target Cost	Maximum Payload-to-Orbit
Control Variables	
State Variables	

#### 4.2.4 IV. Second Stage Return Trajectory

After releasing the third stage rocket, the scramjet-powered second stage must return back to the initial launch site. During the fly-back, the SPARTAN cannot exceed its dynamic pressure limit of 50kPa. The end state is constrained to a minimum of  $-20^\circ$  trajectory angle, which is assumed to be an appropriate trajectory angle for approach to a landing strip. All other state variables are left unconstrained at the end point. It is assumed that for an optimal trajectory, the SPARTAN will end its return at the minimum energy state possible, corresponding to the minimum velocity and altitude attainable while satisfying the end latitude and longitude constraints.

During the return, the C-REST engines are able to be throttled on and off. The throttle is set as a control variable, variable between 0 and 1, where 1 represents the maximum equivalence ratio at that point. The fuel mass flow rate is scaled linearly with the throttle:

$$\dot{m}_{fuel} = \dot{m}_{fuel,max} \text{throttle}, \quad (4.15)$$

and the thrust of the engine is assumed to scale linearly with the fuel mass flow rate.

Initial Constraints	Altitude Velocity Flight Path Angle Heading Angle Latitude Longitude
Terminal Constraints	Distance From Launch Site
Path Constraints	Dynamic Pressure
Target Cost	Minimum End Velocity
Control Variables	
State Variables	

#### 4.2.5 V. Third Stage Powered Ascent

The trajectory of the third stage rocket is only directly optimised during the powered section of its trajectory. During powered flight, the engine is used to control the third stage vehicle. After this point, the engine is cut, and the third stage is assumed to not have sufficient aerodynamic control to manoeuvre.

The third stage rocket is constrained to an angle of attack of less than  $20^\circ$ . This is assumed to be the maximum controllable angle of attack possible for the third stage rocket. Additionally, a maximum normal force restriction is placed on the third stage. Previous studies flew the third stage rocket at a constant  $10^\circ$  angle of attack, and initially released the rocket at 50kPa[CITEXX]. For this study, it is assumed that  $10^\circ$  angle of attack produces the maximum allowable normal force at 50kPa, to prevent the rocket from being released into an environment which could exceed its structural limitations. The maximum allowable normal force is calculated at the release Mach number, and set as a path constraint.

Initial Constraints	
Terminal Constraints	None
Path Constraints	Angle of Attack
Target Cost	
Control Variables	
State Variables	

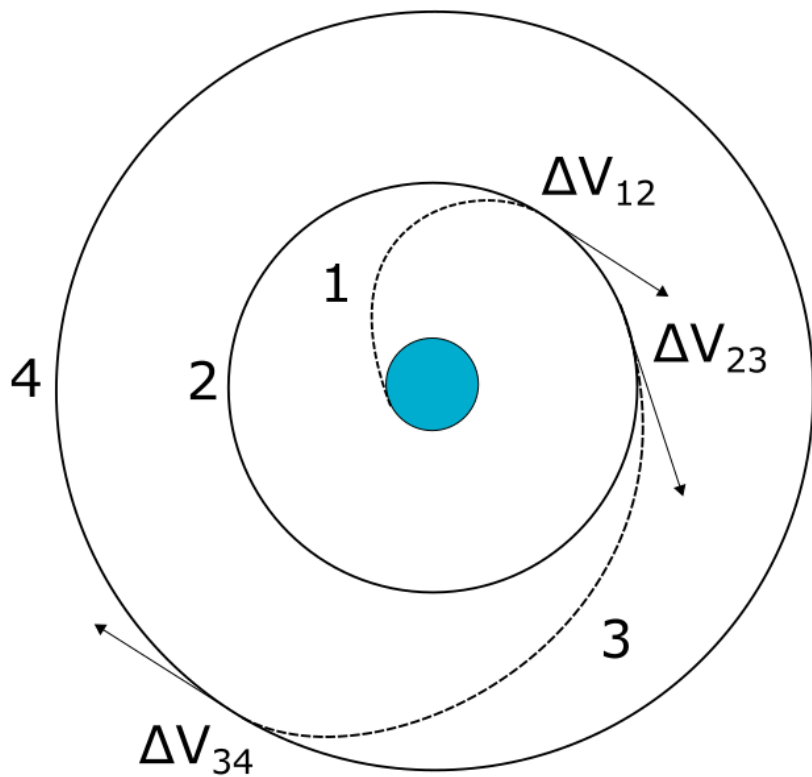


Figure 4.7: The Hohmann transfer manoeuvre.

#### 4.2.6 VI. Third Stage Unpowered Ascent

The unpowered section of the trajectory is simulated from the end of the controlled section of the trajectory, using a second order Taylor series approximation. This integration ceases when the flight path angle reaches  $0^\circ$ . During this phase, the heat shield is released once the rocket has reached a dynamic pressure of  $10\text{Pa}$ , where it is assumed that atmospheric effects will have ceased to have a major thermal effect. As the third stage is required to deliver the payload into heliosynchronous orbit, the third stage must achieve an inclination of  $97.63^\circ$  at the end of this phase.

#### 4.2.7 VII. Hohmann Transfer

After the rocket has attained exoatmospheric flight parallel to the Earth's surface, a circularisation burn is performed. This circularisation burn takes the third stage rocket into low orbit around the Earth. However, in order to reach a heliosynchronous orbit of  $567\text{km}$ , the orbit of the third stage rocket must be raised. To this end, the final manoeuvre performed by the third stage rocket is a Hohmann transfer. A Hohmann transfer is the most fuel efficient way to raise a spacecraft from one circular orbit to another. Following circularisation, the third stage engine is reignited (or remains ignited) and the third stage manoeuvres into an appropriate elliptical orbit.

Circularisation burn

$$\Delta V_{12} = \sqrt{\frac{\mu}{r_2}} - V_1 \quad (4.16)$$

begin hohmann transfer

$$\Delta V_{23} = \sqrt{\frac{\mu}{r_2}} \left( \sqrt{\frac{2r_4}{r_2 + r_4}} - 1 \right) \quad (4.17)$$

insertion burn

$$\Delta V_{34} = \sqrt{\frac{\mu}{r_4}} \left( 1 - \sqrt{\frac{2r_2}{r_2 + r_4}} \right) \quad (4.18)$$

The mass of the third stage rocket at each burn is calculated using the Tsiolkovsky rocket equation:

$$m_2 = \frac{m_{1f}}{\exp^{\frac{V_{12}}{I_{SP} \cdot g_0}}} \quad (4.19)$$

$$m_3 = \frac{m_2}{\exp^{\frac{V_{23}}{I_{SP} \cdot g_0}}} \quad (4.20)$$

$$m_4 = \frac{m_3}{\exp^{\frac{V_{34}}{I_{SP} \cdot g_0}}} \quad (4.21)$$

Finally, the payload-to-orbit is determined by removing the structural mass from the total mass of the vehicle at the end of the Hohmann transfer. The remaining mass is taken to be the payload-to-orbit capability of the vehicle.

$$m_{payload} = m_4 - m_{struct} \quad (4.22)$$

## 4.3 Optimality Conditions

LODESTAR provides the capacity to validate the optimal solution provided by the pseudospectral method solver. This partial validation is used to determine whether the pseudospectral method solver has converged close to an optimal solution of the nonlinear programming problem. It is particularly useful to validate that the optimality and constraint tolerances which have been chosen are sufficiently small, or to check whether the pseudospectral method solver has approached an optimal solution in the case that the defined tolerances are not able to be reached. This partial validation is achieved through the examination of four key metrics; the IPOPT constraint violation and dual infeasibility parameters; the Hamiltonian necessary condition for optimality; the state derivatives; and finally a forward simulation.

The first metrics to be checked are the IPOPT constraint violation (*inf-pr*) and dual infeasibility parameter (*inf-du*)[60]. The constraint violation parameter is a measure of the infinity-norm ( $L_\infty$ -norm) of the constraints of the problem[60]. This factor must be suitably small in order to indi-

cate that the constraints of the problem to have been met. While the permissible magnitude of this factor changes with each individual problem, it is always desirable for this factor to be as small as possible. For this study only solutions with  $L_\infty\text{-norm}(inf-pr) < 10^{-4}$  are accepted as having satisfied the imposed constraints. The dual infeasibility is a Karush-Kuhn-Tucker condition[50], which is a necessary condition for optimality. A dual feasible solution indicates that the dual problem is at least a lower bound on the optimal solution,  $p^*$ , ie.  $p^* \geq g(\lambda, v)$ . For more details on duality see [50]. A low dual infeasibility indicates that the solution has approached an optimal solution. Again, the magnitude of this value is variable with each problem, though as a problem becomes more complex, the ability to converge towards an optimal solution diminishes. For the problem in this study,  $L_\infty\text{-norm}(inf-du) < 0$  are accepted due to the highly complex nature of the vehicle model. In this study it is accepted that a given solution may not approach the global optimum, and multiple solutions are calculated to mitigate the error caused by the problem complexity, with the 'most optimal' solution selected.

The Hamiltonian of the optimal control problem is defined as

$$H(x(t), u(t), \lambda(t), t) = \lambda^T(t)f(x(t), u(t)) + L(x(t), u(t)). \quad (4.23)$$

The Hamiltonian of the optimal control problem is investigated as a partial verification that the first order necessary conditions hold. Due to the unconstrained end time of the trajectory problems,  $H \equiv 0$  [95]. This is calculated using LODESTAR and the Hamiltonian condition is able to be verified. The Hamiltonian will likely not be exactly equal to zero along the trajectory. This is due to the heuristic nature of the solver, which will approach close to an optimal solution, but never reach it exactly. A sufficiently small Hamiltonian indicates that the end solution approaches an optimal solution, and may be a candidate as an optimised trajectory case.

The pseudospectral method considers the dynamics of the system as constraints on the optimal control problem, and solves across the entire trajectory simultaneously. This causes the physical system dynamics to have an associated margin of error, ie.  $\dot{x} = f(x)$  will only hold to a certain degree of accuracy. For a well converged solution, this margin of error will be negligibly small, and the dynamics of the system will be consistent with realistic Newtonian dynamics. However, when the problem is not well converged, the dynamics of the system may have a large error. A check is performed on each state to affirm that the derivative of the approximated state is equal to the derivative supplied by the vehicle model. This checks that the solver has converged to a solution which satisfies the vehicle dynamics at each individual node. The state feasibility of the solution is checked through a comparison of the state derivatives,  $\dot{x} = f(x, u)$ .  $\dot{x}$  is first determined through numerical differentiation of the state variables over the solution time. Then  $f(x, u)$  is determined using the dynamics of the system and vehicle model, in the same way that  $f(x, u)$  is input to the pseudospectral solver. Examination of the error between the 'expected' state derivatives, and the

numerical approximation of the derivatives,  $\dot{x} - f(x, u)$ , allows the accuracy of the system dynamics to be verified.

The final verification check is a full forward simulation. This forward simulation starts at the initial conditions prescribed by the pseudospectral method solver, and propagates the dynamics of the system forward in time using numerical approximation. The forward simulation uses the optimised control variables as the only input. This checks that the flight path will follow the optimised path using the calculated control inputs. This is the most complete test of the optimal solution. However, in some cases calculating a forward solution may be problematic. The pseudospectral method has a limited number of nodes, potentially spread across relatively large time steps. Due to the high accuracy of the polynomial approximation, the pseudospectral method is able to maintain accuracy over large time steps. However, a forward simulation necessarily has less accuracy than the spectral method, and may interpolate differently when applied to the optimal solution, causing minor deviations. This particularly occurs when the states or controls are changing rapidly. These minor deviations may propagate themselves forward, causing significant deviation in the forward simulation. In some cases, this can also cause the forward simulation to appear close to the optimial solution, when it should deviate. For this reason, a forward simulation is a good final check of an optimal solution, but knowledge of the system dynamics must be used, along with the other verification methods, to ascertain if a solution has converged sufficiently.

It may be useful to include example images here



---

---

## CHAPTER 5

---

### OPTIMISED ASCENT TRAJECTORY

sensitivity study including: potentially max heating rate? max  $q$ , L/d (potentially varied viscous drag? as this is uncertain and has a magnitude change on the return trajectory), Isp, third stage mass and L/D

This chapter presents a maximum payload-to-orbit trajectory optimisation for the rocket-scramjet-rocket launch system incorporating the SPARTAN. This chapter consists of a modified form of the Journal of Spacecraft and Rockets paper 'Trajectory Design of a Rocket-Scramjet-Rocket Multi-Stage Launch System' (accepted for publication). A constant dynamic pressure case with the minimum pull-up necessary for the third stage to achieve orbit is computed as a reference. The trajectory of the SPARTAN and third stage are optimised for maximum payload-to-orbit, and compared to the minimum pull-up trajectory. A sensitivity study is carried out by varying the maximum allowable dynamic pressure by  $\pm 10^\circ$ , followed by increasing the drag by  $10^\circ$ , and computing new optimal trajectory results.

The results of this chapter are currently undergoing modification. The results will be updated to use a combined SPARTAN/Third stage optimisation which has been successfully implemented in LODESTAR, rather than separately optimised trajectories. This improvement results in a more optimal trajectory. Cart3d aerodynamics will be used rather than Hypaero for consistency, with viscous corrections which have been calculated by Alexander Ward. The sensitivity analysis will be refocussed slightly to highlight the potential implications to future vehicle designs. Currently, the ascent optimisation in LODESTAR is complete, however, aerodynamic simulations are being carried out in Cart3D to add additional nozzle and boat-tail thrust to the propulsion database. When these simulations are complete, optimal trajectories will be generated. The general shape of the optimised trajectories is not expected to change significantly.

This chapter will be expanded to include a more thorough sensitivity analysis, including the variation of specific impulse, along with more data points for each parameter variation. The discussion

on the sensitivity analysis will be refocussed to highlight the particular design attributes which may lead to performance variations. Additionally the validation of each case will be discussed in detail, with forward simulation comparisons and optimality condition validations provided in appendices.

### 5.0.1 Optimisation Methodology

The three stages are considered as separate optimisation problems, which are coupled at the stage separation points. The first and second stages are coupled by a separation point which is determined by the optimal altitude and flight path angle for the second stage trajectory, as well as the minimum starting velocity of the scramjet. This separation point is used as an end condition on the first stage optimisation. For the minimum pull-up case, the second and third stages are coupled by the end point of the second stage simulation, which is reached when the second stage has expended all of its fuel. The third stage trajectory is optimised for maximum payload from the end of the second stage trajectory.

For the maximum payload cases, the second and third stages are coupled *a priori* by running the third stage optimisation repeatedly for different separation altitudes, velocities, and angles and tabulating the results. The terminal cost of payload-to-orbit, for the second stage optimisation, is generated from this table using interpolation. By setting the objective of the third stage optimisation to maximise payload mass, the coupled optimisation of the second stage in turn maximises payload mass over both stages. The coupling of the stage simulations means that the stage optimisations are performed backwards-in-time to design the complete trajectory; first the third stage is optimised for maximum payload-to-orbit and tabulated over a range of altitudes, velocities and flight path angles, then the second stage is optimised for maximum payload-to-orbit, and lastly the first stage is optimised for fuel mass to reach the optimal second stage start point.

## 5.1 Current Methodology

This section presents the current optimisation methodology, used to generate the optimised ascent trajectory results. This section will be updated to show the combined optimisation, and some details will be moved to Chapter 4.

### Third Stage Optimisation

The third stage rocket trajectory is optimised for maximum payload-to-orbit, so that the second stage scramjet and third stage rocket form a Bolza optimisation problem and maximise payload collectively. The cost function is configured to maximise payload at the end of the trajectory:

$$\min_{\mathbf{u}_3} C_{3 \rightarrow LEO}(\mathbf{x}_3(t_{3,f})) \quad (5.1)$$

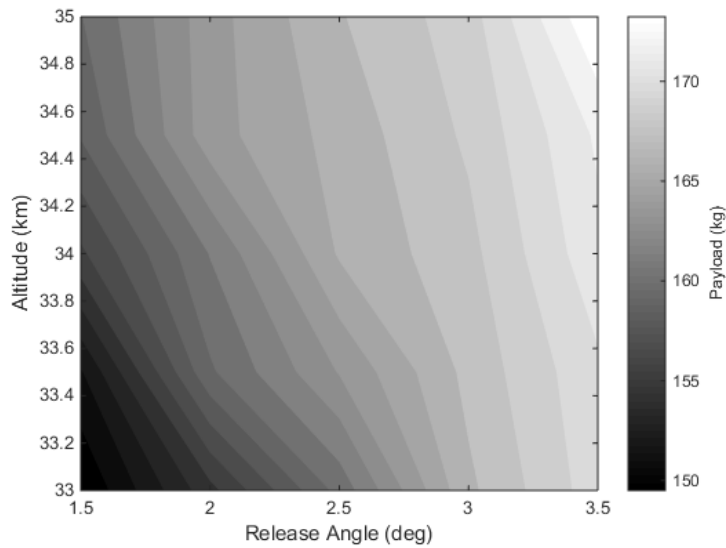


Figure 5.1: Payload mass results with variation in rocket stage release point for  $v = 2875\text{m/s}$ , heading angle =  $1.78 \text{ rad}$  and latitude =  $-0.136 \text{ rad}$ .

where

$$C_{3 \rightarrow LEO}(\mathbf{x}_3(t_{3,f})) = -m_{payload}, \quad (5.2)$$

and  $\mathbf{x}_3(t_{3,f})$  are the tabulated separation conditions of altitude, velocity, and flight path angle. A direct shooting optimisation is performed with twenty angle of attack node points, interconnected by spline interpolation from separation,  $t_{3,0}$ , to a variable end time,  $t_{AoA,f}$ . At this time, the angle of attack is gradually reduced, so that it reaches 0 at the end of burn time,  $t_{burn,f}$ , also variable. A constraint is imposed so that the angle of attack must have at least 10 seconds to reduce to 0 at end of burn, ie.  $t_{burn,f} - t_{AoA,f} \geq 10$ , to allow time for manoeuvring.

The payload mass is calculated after the Hohmann transfer to the desired orbit, by taking the remaining fuel to be the effective payload capacity. SQP is used to find the optimal solution, utilising MATLAB's *fmincon* solver[124]. As an example, tabulated optimal payload to orbit results for a 2875m/s third stage release velocity are shown in Figure 5.1. Payload increases with both altitude and release angle, however it is clear that the potential payload increase due to increasing the separation altitude lessens as release angle increases.

### First Stage Optimisation

After launch, the first stage flies vertically until 100m altitude, when a pitchover is initiated. From pitchover, the first stage is optimised for the minimum fuel mass necessary to reach the first-second stage separation conditions,  $\mathbf{x}_1(t_{1,f})$ , of 1520m/s velocity, and altitude and flight path angle determined by the second stage trajectory.

The separation velocity of 1520m/s corresponds to Mach 5.1 at 50kPa, the minimum operating point of the proposed scramjet[93]. Release at the minimum operable point is advantageous, as the scramjet specific impulse increases at low velocities[93]. The altitude and flight path angle at first-second stage separation is defined by the optimised second stage. This approach is used on account of the selected first stage being able to reach the required range of altitudes and flight angles at 1520m/s with small fuel mass variations. Nevertheless, small variation in fuel mass can have an important effect on the capabilities of the first stage, influencing the velocity achievable at first to second stage separation, as well as the rate at which the rocket is able to pitch, and consequentially, the altitude and flight path angle range of the first stage. The optimal (lowest fuel consumption) trajectory for the first stage stack that can reach first-second stage separation condition  $\mathbf{x}_1(t_{1,f})$  is found by setting a cost function to minimise fuel mass:

$$\min_{\mathbf{u}_1} C_{1 \rightarrow 2}(\mathbf{x}_1(t_{1,f})) \quad (5.3)$$

where

$$C_{1 \rightarrow 2}(\mathbf{x}_1(t_{1,f})) = m_{fuel} \quad (5.4)$$

and the end point is fixed by the optimal second stage start conditions. The first stage is limited to  $-5^\circ$  angle of attack to produce a conservative trajectory solution, within the capabilities of the vehicle. The optimal trajectory is determined using the pseudospectral method. Ten results are obtained by varying the number of nodes in DIDO between 90-99, converging to very similar minima. The final result is chosen as the solution which uses the least fuel.

### Second Stage Optimisation - Constant Dynamic Pressure, Minimum Pull-Up

The constant dynamic pressure case with minimum pull-up optimises the trajectory to minimise variation from the desired dynamic pressure, with the third stage release angle constrained to  $1.5^\circ$ , approximately the minimum release angle necessary to reach orbit. This constraint results in a trajectory with the smallest possible pull-up manoeuvre. The trajectory is configured with a quadratic cost function centred around 50kPa dynamic pressure:

$$\min_{\mathbf{u}_2} C_2(\mathbf{x}_2(t_2), \mathbf{u}_2(t_2)) \quad (5.5)$$

where

$$C_2(\mathbf{x}_2(t_2), \mathbf{u}_2(t_2)) = \int_{t_{2,0}}^{t_{2,f}} \frac{(\mathbf{q} - 50 \times 10^3)^2 + 10^5}{10^5} dt \quad (5.6)$$

This quadratic function provides a smooth, continuous function to increase solver stability and ensure uniform dynamic pressure. Scaling and translating constants of  $10^5$  are included to normalize the cost function, in order to improve the accuracy and stability of the solution. Second-third stage separation occurs when the scramjet has expended all of its fuel. The third stage is then optimised for maximum

payload from the calculated second-third stage separation point.

In order to ensure an optimal solution, the number of nodes which DIDO uses is manually varied between 96-105, and a solution computed for each node value to ensure a distinct local minima. Ten solutions are observed to provide a sufficient number of node variation, with the solutions converging to similar local minima. The range of node values is chosen to produce accurate solutions, with efficient computation times. The final solution chosen corresponds to the node value which most minimises the cost function, and thus minimises the deviation from the 50kPa dynamic pressure trajectory.

### Second Stage Optimisation - Maximised Payload

For the maximum payload optimisation, the second and third stages are considered using a dynamic programming approach. First, in order to increase the computational efficiency of the optimisation, optimal third stage payloads are tabulated over a 3 degree grid of separation conditions,  $\mathbf{x}_2(t_{2,f})$ , as described in Section 5.1, providing the optimal payload for a range of velocity, altitude and flight path angles at separation as shown in Figure 5.1. Then, the interpolated third stage payload is used as the terminal cost  $C_{2 \rightarrow 3}(\mathbf{x}_2(t_{2,f}))$  for the calculation of the second stage trajectory optimisation, which optimises both the second and third stages by setting the cost function to maximise payload:

$$\min_{\mathbf{u}_2} C_2(\mathbf{x}_2(t_2), \mathbf{u}_2(t_2)) + C_{2 \rightarrow 3}(\mathbf{x}_2(t_{2,f})) \quad (5.7)$$

where

$$C_2(\mathbf{x}_2(t_2), \mathbf{u}_2(t_2)) = 0.01 \int_{t_{2,0}}^{t_{2,f}} \dot{m}_{fuel} dt \quad (5.8)$$

$$C_{2 \rightarrow 3}(\mathbf{x}_2(t_{2,f})) = -m_{payload}. \quad (5.9)$$

$C_2(\mathbf{x}_2(t_2), \mathbf{u}_2(t_2))$  is included to improve numerical stability and is weighted by a constant, 0.01, in order to have negligible effect on the resultant trajectory. This problem is solved using the pseudospectral method[105]. As with the constant dynamic pressure case, the number of nodes is manually varied between 96-105, and a solution computed for each node value, converging to similar local minima. The final solution chosen corresponds to the node value which most maximises the payload-to-orbit of the vehicle. The third stage is optimised for maximum payload from the calculated second-third stage separation point, as a check to ensure that the interpolation has provided an accurate payload-to-orbit result.

## 5.2 Optimised Ascent Trajectory Results

LODESTAR is used to investigate the suitability of a pseudospectral method approach to optimisation of scramjet-rocket trajectories and to develop optimal trajectory solutions. The following trajectories

are developed:

1. :  $q = 50\text{kPa}$  fixed SPARTAN trajectory with minimum pull-up  
→ Verifies simulation and provides baseline trajectory.
2. : Trajectory optimised for payload-to-orbit,  $q_{max} = 50\text{kPa}$   
→ Demonstrates improved performance through coupled trajectory optimisation.
3. : Trajectory optimised for payload-to-orbit,  $q_{max} = 45\text{kPa}$  &  $q_{max} = 55\text{kPa}$   
→ Comparison of these simulations allows investigation into the effect of  $q$  max on payload-to-orbit.
4. : Trajectory optimised for payload-to-orbit,  $q_{max} = 50\text{kPa}$ , 110% SPARTAN Drag  
→ Comparison of optimal trajectories at 100% and 110% drag allows investigation of the robustness of the solution with variation in vehicle design.

Table 5.1 details key results for comparison.

Table 5.1: Summary of Simulation Results

Trajectory Condition	1	2	3a	3b	4
	$q = 50\text{kPa}$ $\gamma_{2 \rightarrow 3} = 1.5^\circ$	$q \leq 50\text{kPa}$ $\text{Max } m_{Payload}$	$q \leq 45\text{kPa}$ $\text{Max } m_{Payload}$	$q \leq 55\text{kPa}$ $\text{Max } m_{Payload}$	$q \leq 50\text{kPa}$ $\text{Max } m_{Payload}$ $110\% C_D$
<b>Payload to Orbit (kg)</b>	156.8	169.9	163.9	176.4	161.8
<b>Separation Alt, 1→2 (km)</b>	24.4	25.0	25.6	24.0	25.3
<b>1<sup>st</sup> Stage Structural Mass Fraction</b>	.0740	.0740	.0744	.0744	.0749
<b>Separation Alt, 2→3(km)</b>	33.17	34.49	34.46	34.58	34.29
<b>Separation <math>v</math>, 2→3(m/s)</b>	2905	2881	2861	2893	2829
<b>Separation <math>\gamma</math>, 2→3(deg)</b>	1.50	2.91	2.31	3.39	2.97
<b>Separation <math>q</math>, 2→3(kPa)</b>	46.3	36.9	36.59	36.71	36.7
<b>2<sup>nd</sup> Stage L/D, 2→3</b>	3.21	3.24	3.35	3.34	2.94
<b>2<sup>nd</sup> Stage Flight Time (s)</b>	349.1	357.0	381.8	326.8	356.9
<b>3<sup>rd</sup> Stage <math>t</math>, <math>q &gt; 20\text{kpa}</math> (s)</b>	65	29	25	23	27

### 5.2.1 First Stage Evaluation - q=50kpa Second Stage Separation

Figure 5.2 shows an example first stage trajectory, optimised for minimum mass, with end conditions of 24.4km altitude and 1.56° flight path angle. These separation conditions correspond to the second stage separation conditions for a 50kpa dynamic pressure trajectory.

The first stage flies a fixed vertical trajectory for 3.79s, after which a pitchover is initiated. After pitchover the angle of attack reduces to -1.17° at 13.1s. The angle of attack is then raised to 0.88° at 29.9s, before reducing gradually to the minimum of -5°, adjusting in stages in order to reach the

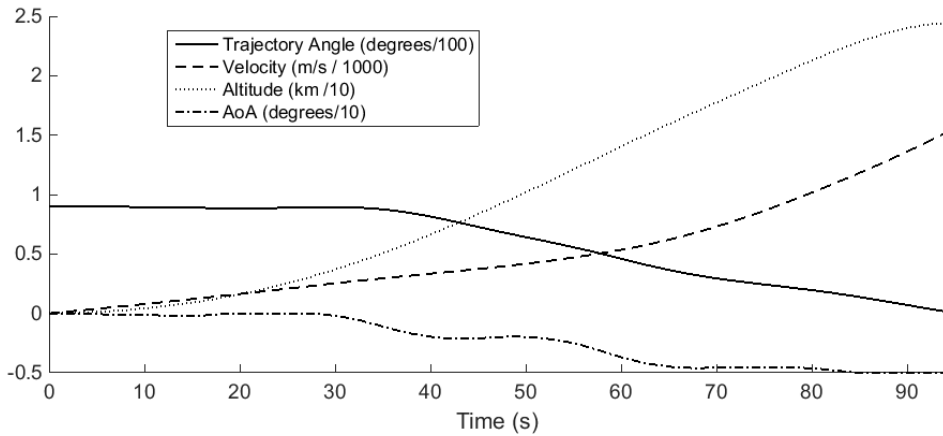


Figure 5.2: First stage trajectory, optimised for minimum fuel mass and a release point of 50kPa.

desired end conditions. An altitude of 24.4km is reached after a total flight time of 93.6s, with a total ground distance of 34.5km covered. This trajectory shape is very similar for all first stage simulation cases.

## 5.2.2 Second Stage Evaluation

### Fixed Dynamic Pressure Trajectory, Minimum Pull-Up

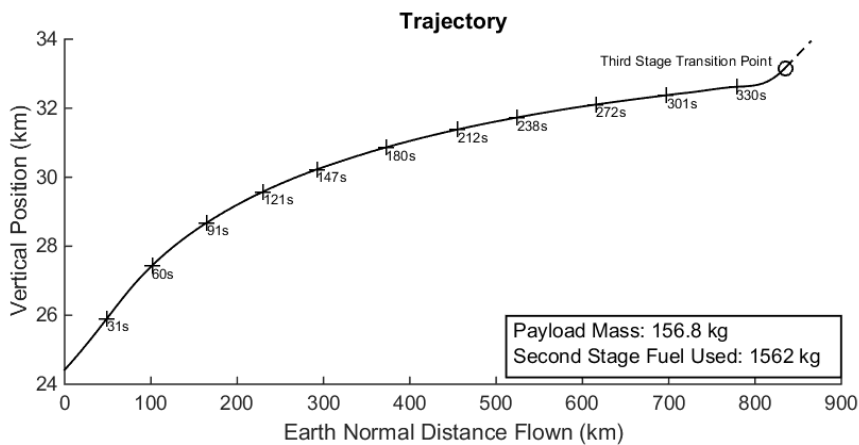


Figure 5.3: Trajectory path of the 2<sup>nd</sup> stage SPARTAN vehicle flying at 50kPa constant dynamic pressure, with 1.5° third stage release angle.

A constant dynamic pressure trajectory with a pull-up to 1.5° flight path angle at third stage release is produced as a baseline for comparison with a payload-optimised trajectory, and to verify that LODESTAR is able to optimise a complex airbreathing trajectory. A pull-up to 1.5° flight path angle is the minimum necessary for the third stage to reach orbit. At release angles below 1.5°, the thrust vector limitations necessary to produce a trimmed trajectory constrain the angle of attack of

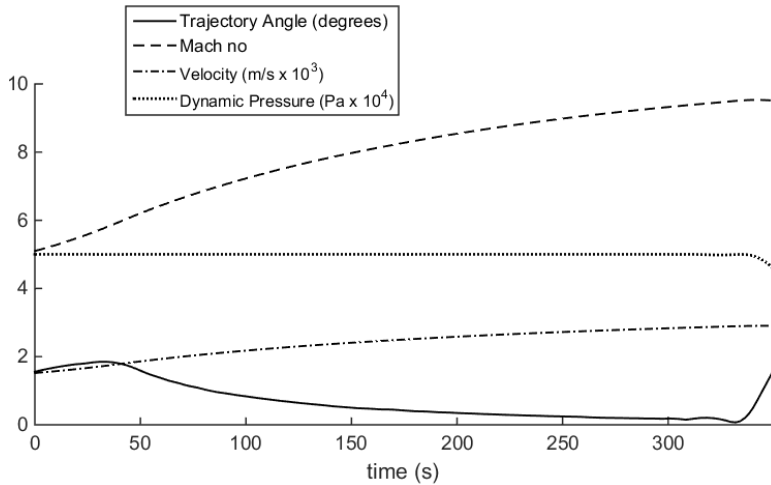


Figure 5.4: Trajectory data for 50kPa constant dynamic pressure trajectory, with  $1.5^\circ$  third stage release angle.

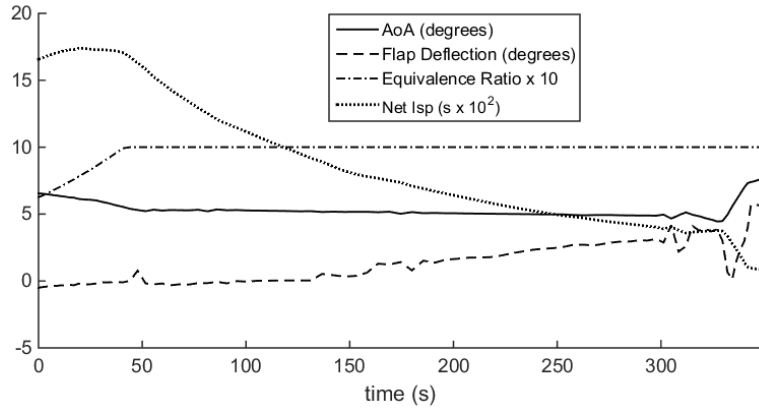


Figure 5.5: Vehicle performance data for 50kPa constant dynamic pressure trajectory, with  $1.5^\circ$  third stage release angle. Note: Flap deflection is positive down.

the third stage so that the rocket does not generate the lift required to exit the atmosphere. This angle of attack limitation, imposed by the maximum thrust vector, necessitates a scramjet-stage pull-up manoeuvre in order for the third stage rocket to operate successfully.

The constant dynamic pressure, minimum pull-up trajectory for the SPARTAN stage is shown in Figures 5.3, 5.4 and 5.5 with key results summarised in Table 5.1. Due to the clear objective of a constant dynamic pressure trajectory, any deviations from the target dynamic pressure are readily apparent, allowing the efficacy of the optimiser to be verified. These results show very close adherence to 50kPa dynamic pressure (maximum 0.29% deviation) until pull-up at 336.4s. Third stage release occurs at 349.1s at 33.17km altitude. Over the trajectory the Mach no. increases from 5.10 to 9.52 and the velocity from 1520m/s to 2905m/s. The flap deflection shows an overall increase from  $-0.53^\circ$  to  $5.76^\circ$  over the trajectory. The net specific impulse ( $I_{sp,net} = \frac{T-D}{m_f g}$ ) generally decreases over the trajectory, as the efficiency of the scramjet engines decreases. However, at the beginning of the

trajectory the equivalence ratio increases as the capture limitations are relaxed with increasing Mach number. This causes the net specific impulse to increase, to a maximum of 1739s, during the first 19.45s flight time.

Figure 5.14 shows the corresponding third stage atmospheric exit trajectory after release, evaluated as described in Chapter 4. After atmospheric exit, this trajectory is followed by a Hohmann transfer to a heliosynchronous orbit, resulting in a total payload to orbit of 156.8kg.

### Dynamic Pressure Limited Trajectory

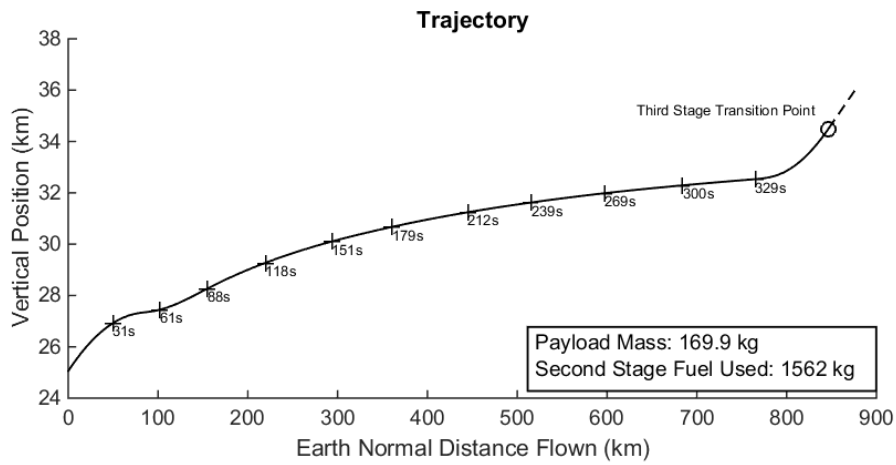


Figure 5.6: Maximum payload trajectory path of the 2<sup>nd</sup> stage SPARTAN vehicle when limited to 50kPa dynamic pressure.

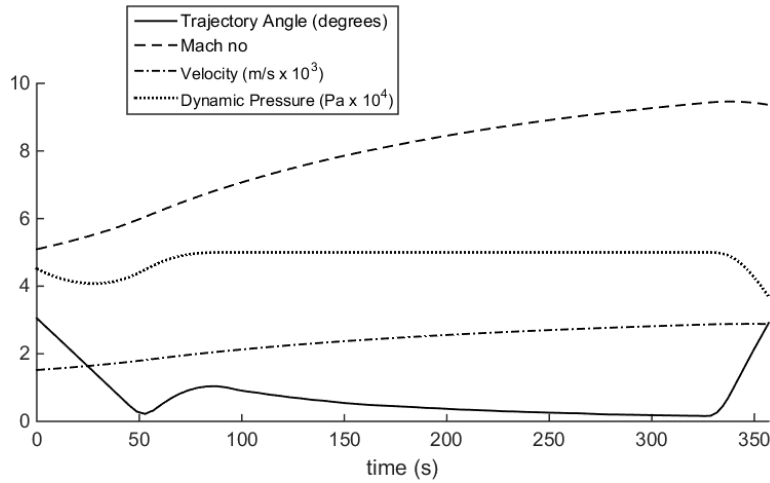


Figure 5.7: Trajectory data for 50kpa dynamic pressure limited trajectory.

LODESTAR is configured to optimise the total payload mass to orbit. A maximum dynamic pressure limit of 50kPa is applied to the optimisation process to allow direct comparison with the constant  $q$  trajectory and so that an equivalent vehicle can be used.

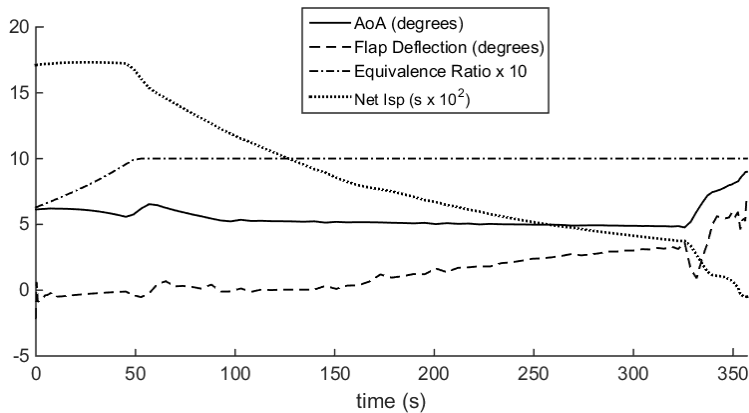


Figure 5.8: Vehicle performance data for 50kPa dynamic pressure limited trajectory. Note: Flap deflection is positive down.

The optimal trajectory shape for a  $q = 50\text{kPa}$  limited, maximum payload to orbit trajectory is shown in Figures 5.6, 5.7 and 5.8 with key results summarised in Table 5.1. The equivalence ratio of the engine is less than 1 until 52.77s, causing the SPARTAN to fly under 50kPa in this region (to a minimum of 40.8kPa) in order to raise equivalence ratio by flying in a higher temperature region. This increase in equivalence ratio results in a corresponding increase in net specific impulse. After the equivalence ratio increases to 1, the trajectory follows a constant dynamic pressure path at 50kPa until 331.7s at which point a pull-up manoeuvre is performed, gaining altitude until rocket stage release at 357.0s flight time. This trajectory is able to deliver 169.9kg of payload to heliocentric orbit, an increase of 8.35% over the constant dynamic pressure result with minimum pull-up. The point at which the pull-up manoeuvre begins is the optimisation result that takes into account the best combination of velocity, altitude and release angle for scramjet stage performance and the release of the rocket stage. This pull-up indicates the region at which increasing altitude and release angle becomes more important than extracting maximum thrust from the scramjet (which is attained at high  $q$  and low flight angle at an equivalence ratio of 1). Flight in a lower dynamic pressure environment results in less thrust output from the scramjet engines, as well as an increase in angle of attack and flap deflection angle to compensate for the additional lift required. Due to this, less overall acceleration is obtained compared to the constant dynamic pressure result with minimum pull-up. Separation occurs at a velocity of 2881m/s, a decrease of 24m/s. However, at the same time separation altitude increases by 1.32km to 34.49km, resulting in a decrease in separation dynamic pressure to 36.9kPa.

The larger scramjet stage pull-up assists the rocket in manoeuvring to exoatmospheric altitude by increasing the altitude and angle at separation by virtue of the increased L/D ratio and manoeuvrability of the scramjet vehicle. Even a small increase in release angle, to the optimal angle of  $2.91^\circ$ , significantly reduces the turning that is required by the rocket as evident from comparing Fig 5.14 and 5.15. Further benefits are the reduced time that the rocket must spend in a high dynamic pressure environment, and a decrease in the maximum dynamic pressure that the rocket stage experiences by

20.3%, as shown in Table 5.1. This allows the structural mass and heat shielding, necessary to achieve exoatmospheric flight, to be decreased, enabling higher payload to orbit.

Compared to studies considering vehicles with a scramjet-rocket transition within a single stage[72][128], the maximum payload to orbit trajectory of the multi-stage system shows a scramjet-rocket transition point at much lower altitudes. This lower transition point is a consequence of the stage separation creating an energy trade-off, which does not occur in a single stage vehicle. Single-stage vehicles must necessarily transport all components to exoatmosphere, and so utilise the scramjet engines until higher altitude to take advantage of their high efficiency. A multi-stage vehicle is able to separate the scramjet stage. This separation occurs when the performance benefits provided by the superior aerodynamics and engine efficiency of the scramjet stage are offset by the energy required to lift the extra mass to higher altitude. The beneficial ability to separate the scramjet stage results in a lower altitude scramjet-rocket transition point, when compared to single stage vehicle designs.

### Dynamic Pressure Sensitivity

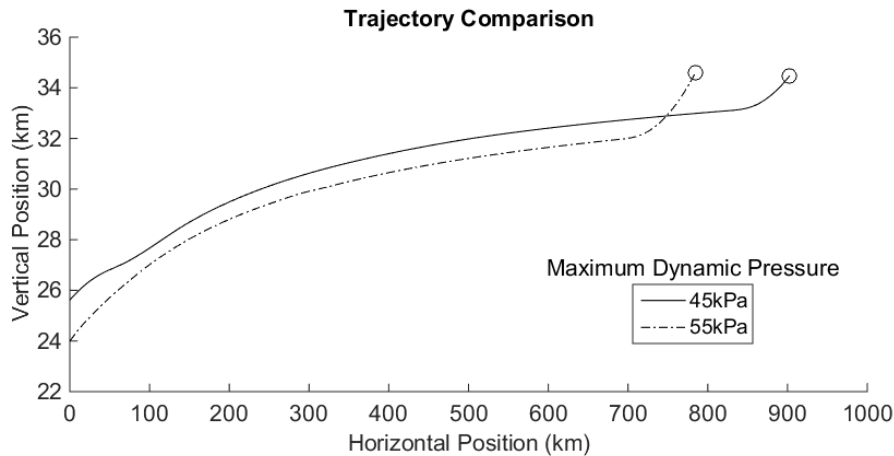


Figure 5.9: Comparison of 45kPa / 55kPa dynamic pressure limited trajectory paths for maximum payload to orbit.

To investigate the sensitivity of the vehicle to changes in  $q_{max}$ , the maximum dynamic pressure is varied to 45kPa and 55kPa and the flight trajectory optimised, with results shown in Figures 5.9, 5.10 and 5.11 and summarised in Table 5.1. The  $\pm 10\%$  variation in maximum dynamic pressure has very little effect on the payload mass delivered to heliocentric orbit. Varying the maximum dynamic pressure by  $\pm 5\text{kPa}$  from 50kPa causes a variation of only  $+6.5\text{kg}(+3.8\%)$  or  $-6.0\text{kg}(-3.5\%)$  in payload to orbit. Separation altitudes of 34.46km and 34.58km are reached for 45kPa and 55kPa limited cases respectively, with separation velocities of 2861m/s and 2893m/s. The 45kPa limited case flies for 381.8s, significantly longer than the 55kPa case which flies for 326.8s. Both trajectories pull-up to similar altitudes, with relatively small variation in separation velocity  $-20\text{m/s}$  or  $+12\text{m/s}$ .

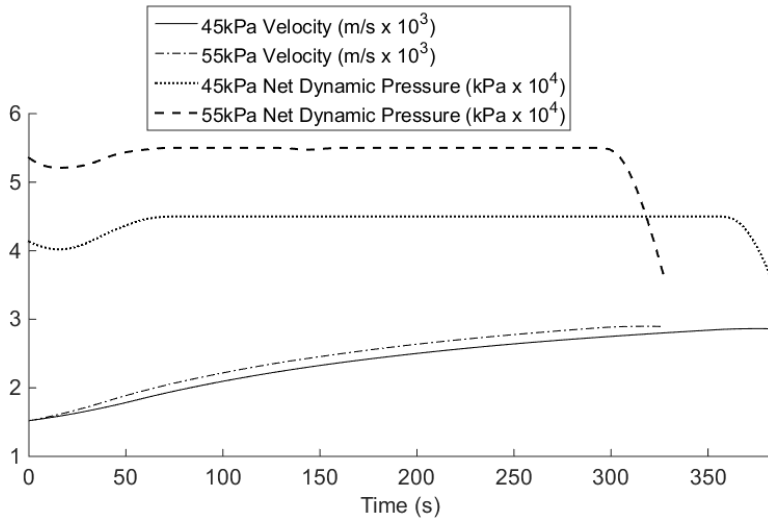


Figure 5.10: Comparison of trajectory data for 45kPa / 55kpa dynamic pressure limited trajectories.

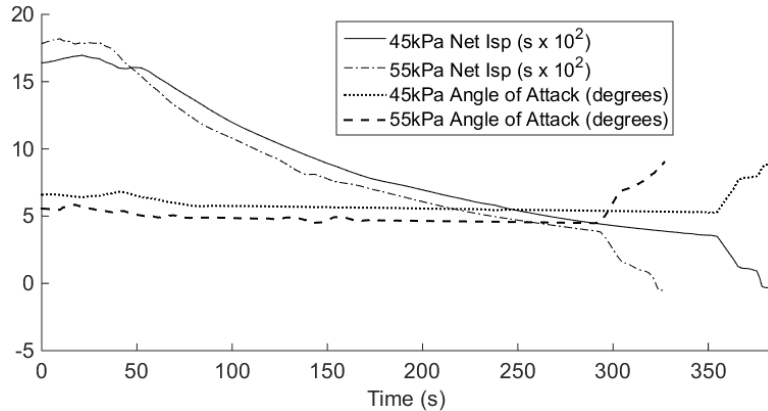


Figure 5.11: Comparison of vehicle performance data for 45kPa / 55kpa dynamic pressure limited trajectories.

This small variation in velocity is despite the increase in air density and decrease in angle of attack required for flight at 55kPa dynamic pressure, both of which increase the mass flow into the engine. Although the thrust output of the REST engines increases with dynamic pressure, so does the drag on the vehicle, and the net increase in performance is small.

Only a small variation in optimal payload mass is observed, without modification of vehicle design to account for the dynamic pressure limit. This indicates that designing and operating a vehicle at lower dynamic pressures may be preferable. Flying at a lower maximum dynamic pressure allows reduction of the structural weight and heat shielding of the vehicle. However, as the 45kPa limited case has a higher first-second stage separation altitude, a larger first stage fuel mass is required, though this increase in fuel mass is small. Between 25.6km and 24.0km (45kPa and 55kPa optimal start points) there is only a 2.2% variation in the fuel mass required. This small variation in first stage fuel consumption would easily be offset by a decrease in second stage structural mass.

### Drag Sensitivity Analysis

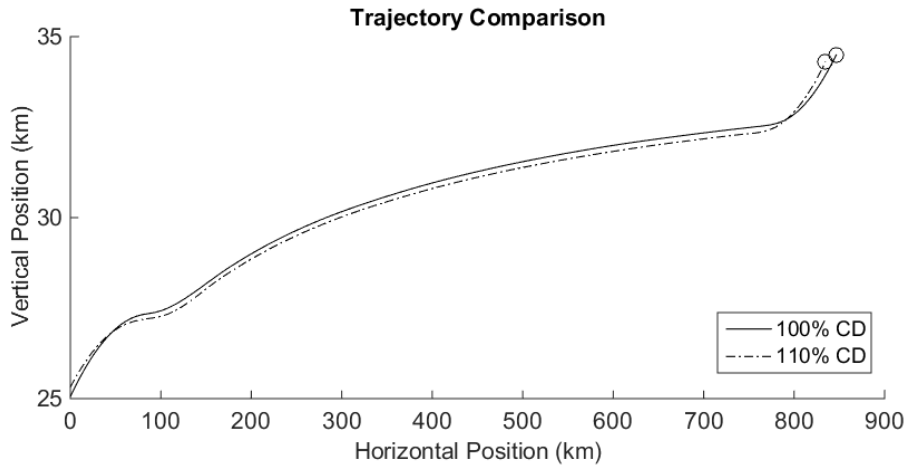


Figure 5.12: Comparison of trajectory paths for 100% and 110% drag cases for a 50kPa dynamic pressure limited maximum payload trajectory.

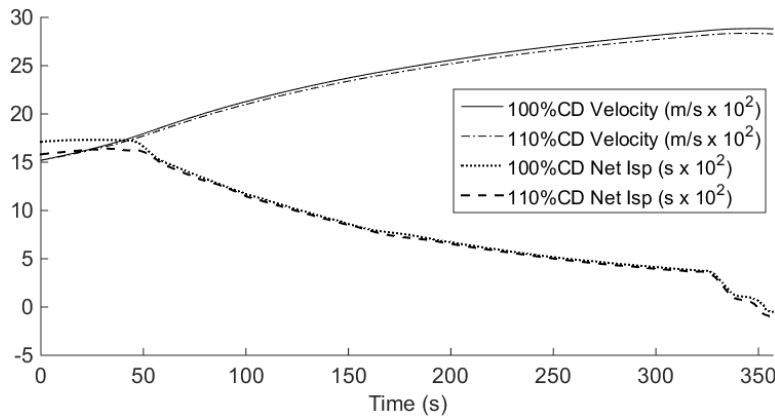


Figure 5.13: Comparison of  $v$  and  $I_{sp,net}$  for 100% and 110% drag cases for a 50kPa dynamic pressure limited maximum payload trajectory.

To investigate the effect of vehicle design and uncertainty in aerodynamic performance on the optimal trajectory the drag on the vehicle is increased by 10%, and an optimised trajectory calculated with dynamic pressure limited to 50kpa. Selected results are compared to the 100% drag result in Figures 5.12 and 5.13. These results show that when drag is increased (ie. L/D is decreased) the optimal trajectory shape is similar to the base-line case, though the high drag second stage follows a slightly slower and hence lower flight path, with a lower stage transition point. The similar flight path shape of the high drag case suggests that sacrificing velocity to increase separation altitude in a pull-up manoeuvre is optimal for multiple vehicle designs. Although the lower transition point indicates that the rocket is favoured at an earlier point in the climb manoeuvre, due to the decreased aerodynamic efficiency of the scramjet vehicle. The net result is a lower payload-to-orbit of 161.8kg

(a decrease of 4.8%).

### 5.2.3 Third Stage Evaluation

Third stage trajectories for release angles of  $1.50^\circ$  and  $2.91^\circ$  are shown in Figures 5.14 and 5.15. These trajectories correspond to third stage release points at the end of a constant dynamic pressure trajectory with minimum pull-up (as shown in Section 5.2.2) and an optimised 50kPa limited trajectory (as shown in Section 5.2.2). These third stage trajectories show a pull-up to high altitude before the circularisation burn is performed.

The third stage released at  $1.5^\circ$ , shown in Figure 5.14, is limited by the maximum thrust vector angle for the first 47s of flight. This places significant limitations on the maximum allowable angle of attack. This angle of attack limitation reduces the lift of the rocket, causing it to spend a large amount of time at low altitude, in a high drag environment. The angle of attack increases gradually to a maximum of  $17.6^\circ$  at 66s before decreasing until burnout at 140s.

The release of the third stage rocket from an optimised scramjet trajectory is shown in Figure 5.15. Release at a higher, more optimal angle, mitigates the effects of the thrust vector angle limitation, so that the thrust vector limit is only reached during the first 10s flight time. After this, the angle of attack is limited by the maximum allowable normal force rather than the thrust vector limit, resulting in a higher maximum angle of attack. The rocket increases flight path angle and gains altitude rapidly, resulting in less time spent in a high drag environment, and a larger payload to orbit. The angle of attack is increased gradually to  $18.14^\circ$  at 48s, before decreasing until burnout at 138s.

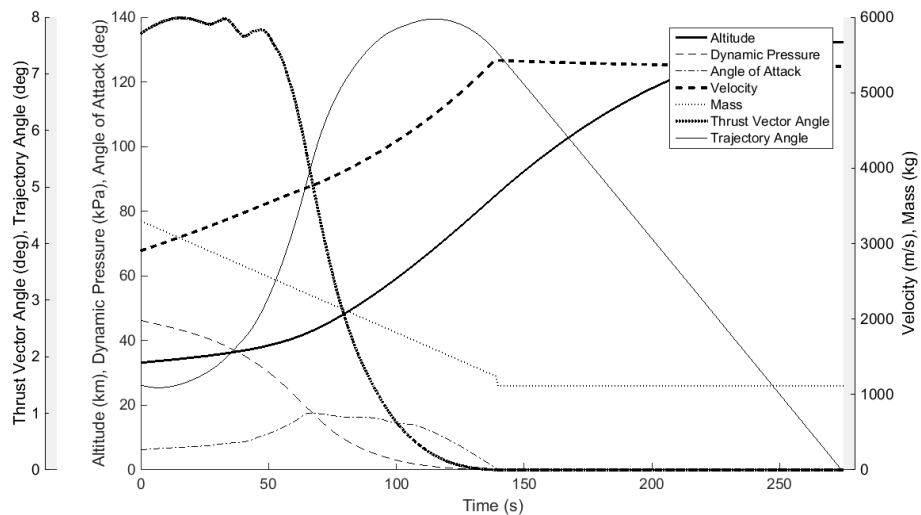


Figure 5.14: Third stage rocket trajectory simulated from the end of the 50kPa constant dynamic pressure SPARTAN trajectory, released at an angle of  $1.50^\circ$ , velocity of 2905m/s, and altitude of 33.17km.

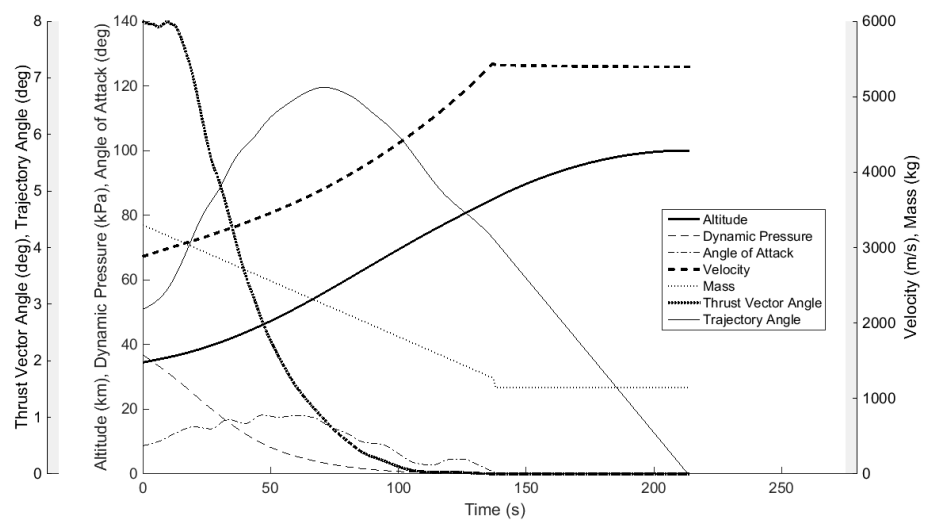


Figure 5.15: Third stage rocket trajectory simulated from the end of the 50kPa dynamic pressure limited maximum payload SPARTAN trajectory, released at an angle of  $2.91^\circ$ , velocity of 2881m/s, and altitude of 34.49km.



---

---

# CHAPTER 6

---

## OPTIMISED TRAJECTORY INCLUDING FLY-BACK

This chapter presents the optimised trajectory of the launch system, including the fly-back of the SPARTAN. The combined optimisation for the ascent/fly-back and third stage trajectory is currently operational in LODESTAR. Figures 6.1-6.7 show an example of a combined optimised trajectory for the ascent/return of the SPARTAN and the ascent of the third stage, for maximum payload-to-orbit. However, the aerodynamic and propulsive databases are currently being updated, and will change the optimised results slightly. It is not expected that the major points of interest in the trajectory will change.

The ascent trajectory will be compared to the optimised ascent without fly-back calculated in Section 5. The SPARTAN compensates for the fly-back by banking during ascent. This requires additional angle of attack, and results in less velocity and a smaller pull-up. A small deviation from 50kPa dynamic pressure is observed directly before pull-up, accompanied by a rise in bank angle. This manoeuvre reduces the total range during ascent for minimal velocity losses, decreasing the fuel necessary for the return flight.

The return flight analysis consists of a modified form of the paper 'Fly-Back of a Scramjet-Powered Accelerator', presented at Scitech 2018. Currently, this analysis is for a standalone optimised fly-back from a fixed point. The results will be modified to be for the fly-back portion of the combined optimisation. The analysis in this section is expected to change little.

The sensitivity analysis in this chapter will be expanded, and will be compared against the sensitivity analysis without fly-back, presented in Chapter 5, to determine how the fly-back changes the sensitivity of the trajectory to the design parameters of the SPARTAN. As in Chapter 5, the validation of each case will be discussed, with forward simulation comparisons and optimality condition validations provided in appendices.

## 6.1 Combined SPARTAN Ascent-Descent & Third Stage Example

This section contains a current example of a concurrently optimised SPARTAN ascent/fly-back and third stage ascent.

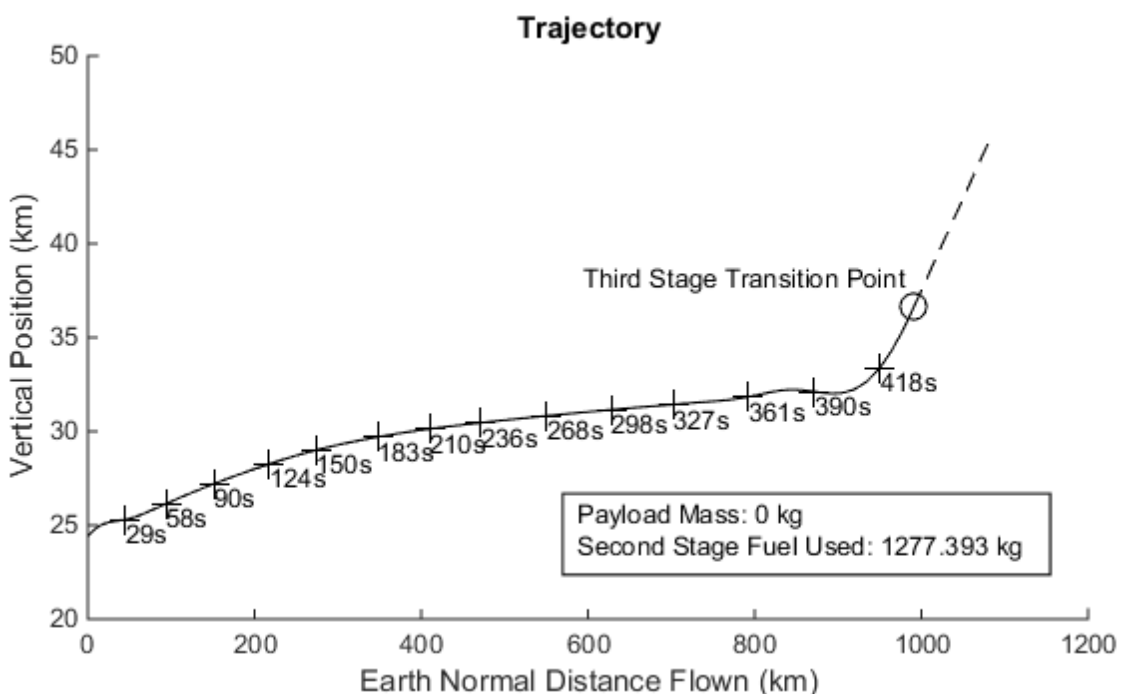


Figure 6.1: The flight path of the SPARTAN ascent.

## 6.1. COMBINED SPARTAN ASCENT-DESCENT & THIRD STAGE EXAMPLE

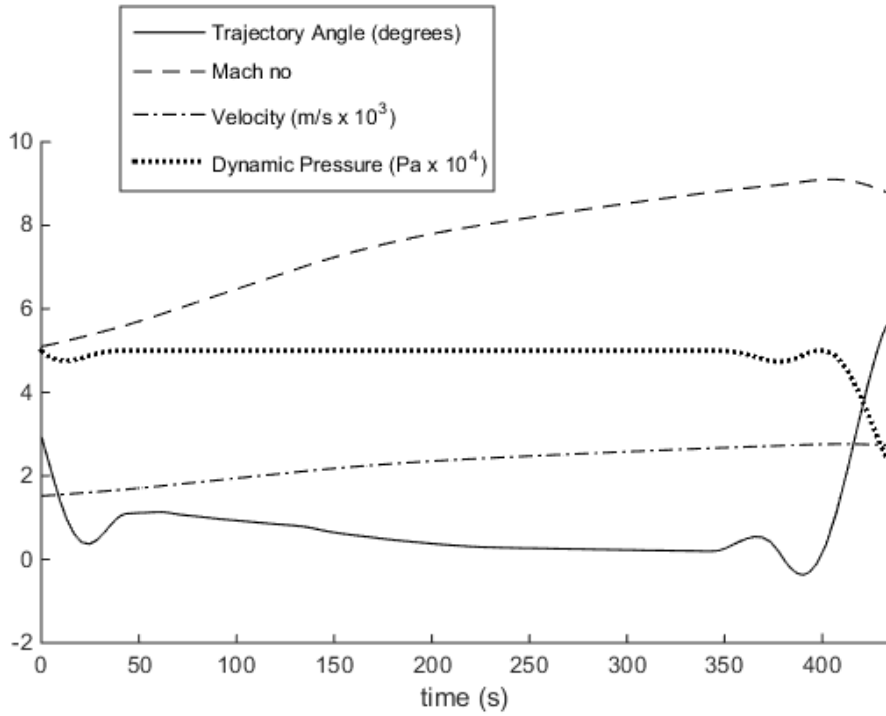


Figure 6.2: Aerodynamic parameters of the SPARTAN ascent.

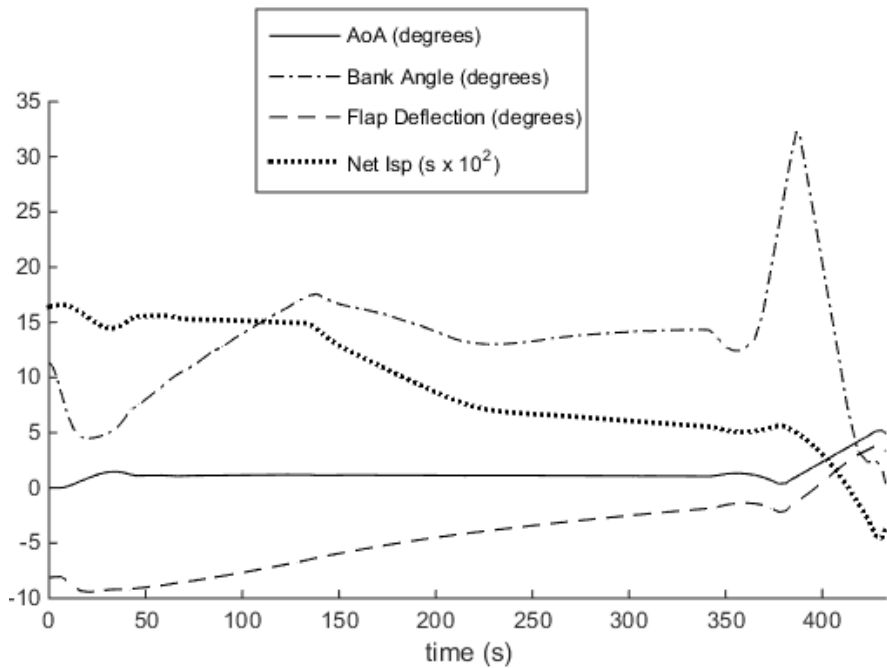


Figure 6.3: Vehicle parameters of the SPARTAN ascent.

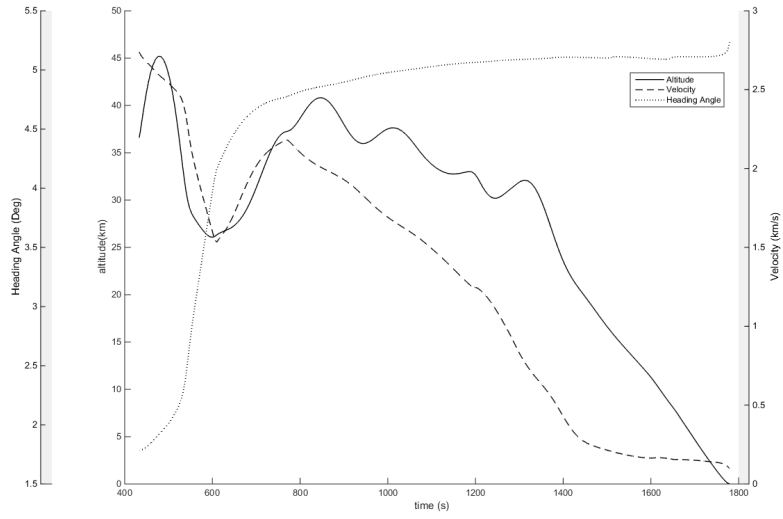


Figure 6.4: The flight path of the SPARTAN fly-back.

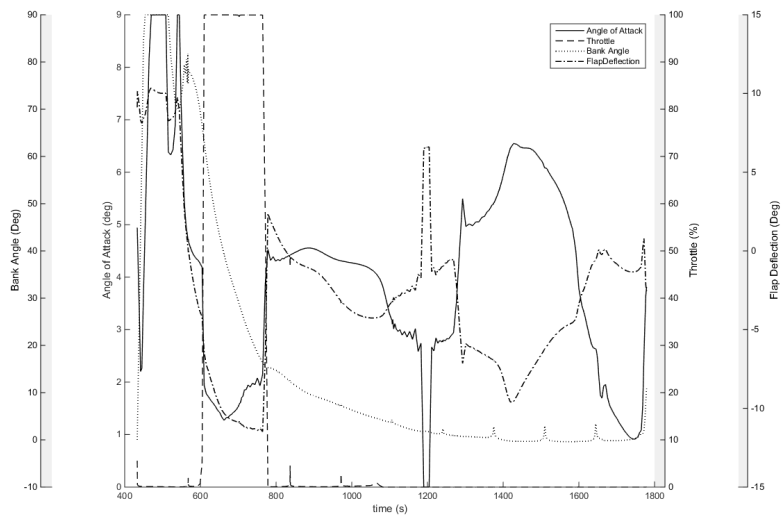


Figure 6.5: Vehicle parameters of the SPARTAN fly-back.

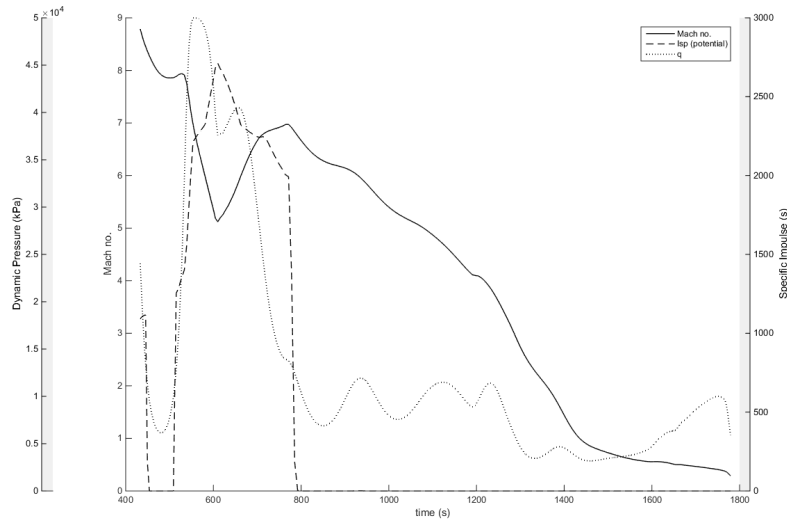


Figure 6.6: Aerodynamic and propulsion parameters of the SPARTAN fly-back.

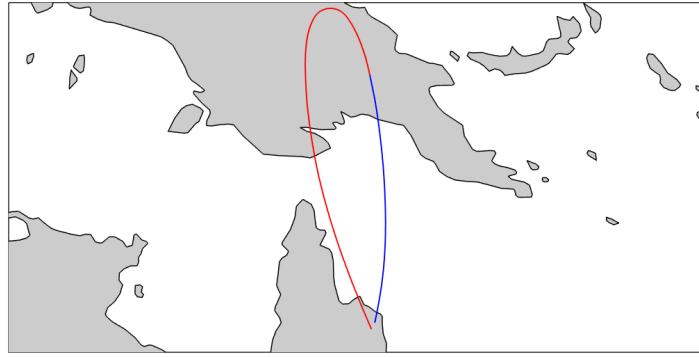


Figure 6.7: The ground track of the ascent and fly-back of the SPARTAN.

## 6.2 Fly-Back Trajectory Analysis

The fly-back of the SPARTAN is optimised using LODESTAR. The fly-back is optimised for minimum fuel usage, with initial conditions constrained to be similar to the intended third stage release point, and end position constrained within 12.7km of the initial launch site, at  $15.3^\circ\text{S}, 144.9^\circ\text{E}$ [38]. The margin of 12.7km is allowed so as to not over-constrain the end position within LODESTAR, and it is assumed that the landing strip will not be at the exact location of the launch site. The angle

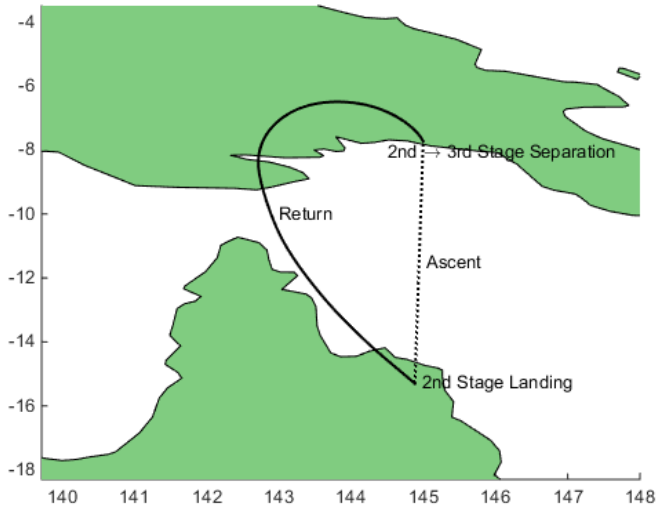
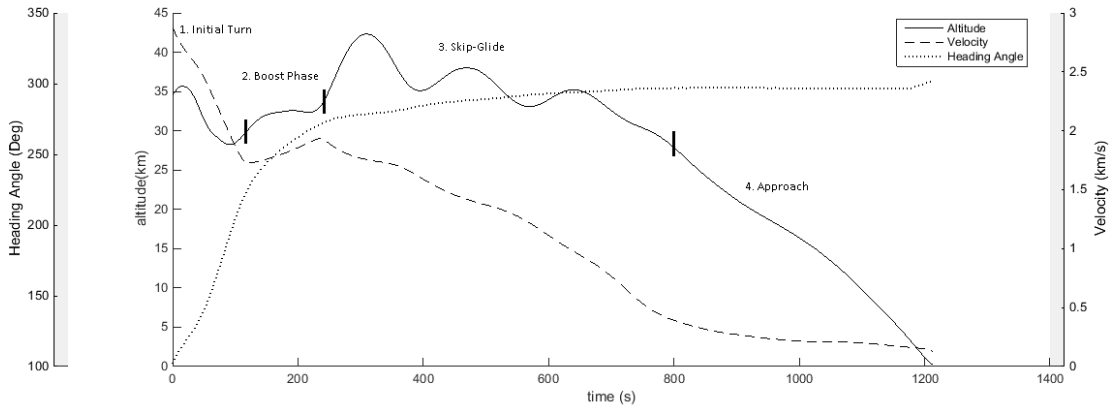


Figure 6.8: Ground track of the optimised fly-back of the SPARTAN vehicle.

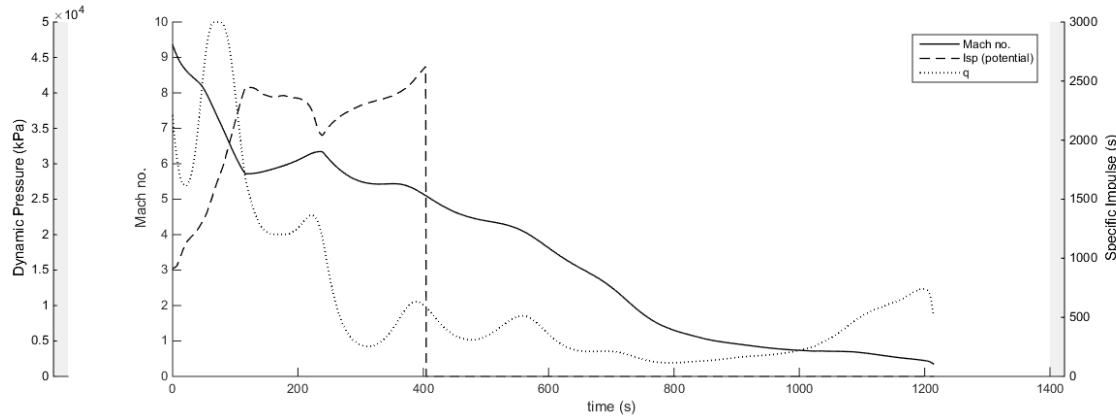
of attack is limited to  $10^\circ$ , to ensure vehicle stability. The bank angle is limited to  $90^\circ$  to produce a conservative solution and to limit any possible design complications that may arise from inverted flight. The dynamic pressure is limited to 50kPa, the structural limit of the vehicle. The scramjet engines are limited to only operate above 20kPa dynamic pressure, an estimated lower limit on the operable mass flow rate. The end of the trajectory is constrained to sub-200m altitude, and a trajectory angle range between  $-10^\circ$  and  $0^\circ$  to ensure that the SPARTAN can perform a landing manoeuvre. These constraints ensure that the vehicle is approaching the landing site at the end of the optimised trajectory. The end velocity is only limited to be greater than 0m/s. It can be assumed that the optimal fly-back trajectory minimises end velocity as shown in the optimised trajectory results. It is also assumed that the vehicle is able to carry any necessary fuel in addition to the fuel required during the ascent trajectory, allowing the initial conditions to be kept constant. The potential specific impulse is shown along the trajectory, this is the specific impulse obtainable from the C-REST engines should they be powered on.

### 6.2.1 Optimised Trajectory

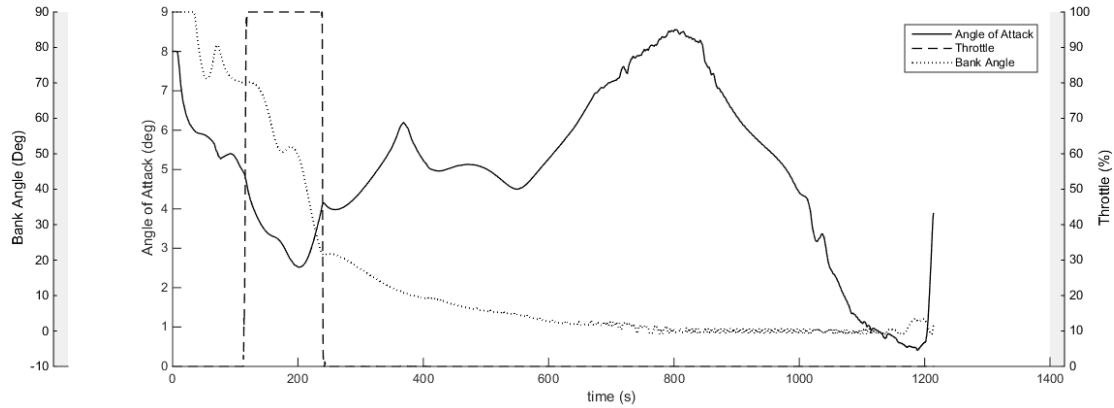
The optimised fly-back trajectory is shown in Figures 6.8 and 6.9. The fly-back is initiated from the optimised second-third stage separation point at 7.7°S, 145.0°E, 34.5km altitude, 2.9° trajectory angle, 2881m/s velocity and 102° heading angle, corresponding to the conditions of optimal third stage release described in Section ???. The SPARTAN is shown to be capable of fly-back, using 166.0kg of fuel, a total increase in the fuel usage of the SPARTAN of 10.6%. The optimised trajectory has four distinct parts; 1. initial turn, 2. boost phase, 3. hop-glide, and 4. approach.



(a) Flight path.



(b) Aerodynamic and performance data.



(c) Control time histories.

Figure 6.9: Trajectory data for the fly-back of the SPARTAN vehicle. Optimised for minimum fuel usage using LODESTAR.

### Initial Turn

The SPARTAN starts at the maximum bank angle of  $90^\circ$ , and sustains this bank angle for 34.4s. At this point, the altitude of the SPARTAN decreases, and the vehicle is close to hitting the dynamic pressure of 50kPa. To avoid exceeding this limit, the bank angle is reduced to  $71.2^\circ$ , allowing the vehicle to generate sufficient lift to slow its descent. The bank angle is then increased again, to  $80.7^\circ$  at 70.8s. After this time, the bank angle is gradually reduced.

### Boost Phase

Soon after the bank angle begins to reduce, at 118.7s flight time and Mach 5.71, the scramjet engines are ignited. The C-REST engines are powered-on at a point of high potential specific impulse, at a low Mach number, and burn for 119.8s. The altitude of the SPARTAN is raised during the majority of the burn, ensuring that the Mach number is kept low for maximum efficiency[94], as shown in Figure 6.9. The maximum altitude is limited by the lower dynamic pressure limit of the C-REST engines of 20kPa. The bank angle of the vehicle is reduced to produce increased lift, so as to increase the altitude of the SPARTAN, while also maximising the specific impulse of the scramjet engines by keeping the angle of attack low. Low angle of attack decreases the temperature and raises the Mach number, at the inlet of the C-REST engines. While these effects partially offset each other[94], the temperature increase is more significant, and decreasing angle of attack has the net effect of increasing the specific impulse of the C-REST engines. This increase in specific impulse is balanced by a decrease in the L/D of the SPARTAN at angle of attack values lower than  $4^\circ$ , as illustrated in Figure 3.17c. However, the specific impulse has a more significant impact than L/D during this phase, resulting in the optimised angle of attack being kept low. At 204s the angle of attack is increased, bringing the L/D of the vehicle towards maximum and initiating the first 'skip' of the skip-glide phase.

### Skip-Glide

During the unpowered trajectory after the burn phase, the angle of attack is controlled so that the L/D of the SPARTAN is close to the maximum. Initially, the SPARTAN performs several 'skips' after the scramjet burn. These are due to the high L/D of the SPARTAN above Mach 4, and are aided by the angle of attack, which is controlled to emphasize the size of the skips. These skips are consistent with research which has shown that a periodic skipping trajectory increases the downrange distance achievable by hypersonic vehicles[30, 58].

### Approach

After the skip phase, as the vehicle is approaching Mach 1, the angle of attack is reduced gradually to bring the SPARTAN down to 200m altitude, in a controlled manner. At the end of the trajectory

the SPARTAN levels out, and reaches 200m altitude at  $-9.6^\circ$  trajectory angle and 119.8m/s velocity. These conditions are similar to those of the space shuttle at landing[107], and it is assumed that the SPARTAN is able to perform a landing manoeuvre after this point.

### 6.2.2 Sensitivity Analysis

To investigate the robustness of the fly-back trajectory to vehicle design; the drag coefficient and specific impulse of the SPARTAN are varied by  $\pm 10\%$ , and the new optimal fly-back trajectories are calculated using LODESTAR. These optimised trajectories, shown in Figures 6.10 and 6.11, investigate the effects of potential performance variation caused by changes in the vehicle design. The consistency of the trajectory shape indicates that the optimal solution is robust with variation in the aerodynamic parameters and specific impulse of the SPARTAN. The optimised trajectories show clear trends with variation in vehicle parameters.

Increasing the drag coefficient causes the fuel necessary for fly-back to increase by +51.5kg (+31.0%). Conversely, decreasing the drag coefficient by 10% causes the fuel necessary for fly-back to decrease by -58.0kg (-34.9%). When the drag is increased (ie. L/D is decreased), the scramjet engine burn phase begins earlier, and continues for longer. The greater burn time allows the maximum altitude attained during the initial 'skip' to be higher. This additional altitude is necessary as the greater drag causes the velocity, and consequentially altitude, of the SPARTAN to decrease more rapidly.

Increasing the specific impulse causes the fuel necessary for fly-back to decrease by -11.5kg (-6.9%), while decreasing the specific impulse causes the fuel necessary to rise by +22.9kg (+13.8%). The start of scramjet burn is consistent across different specific impulse test cases. Due to the increase in thrust, the SPARTAN accelerates more rapidly for the higher specific impulse case. As a consequence, the initial 'skip' is performed sooner, and subsequent skips are larger.

These results indicate that the aerodynamic performance of the SPARTAN has significantly more impact than the efficiency of the scramjet engines on the optimised fly-back trajectory. During the fly-back trajectory, the specific impulse is effecting performance only whilst the scramjet engines are operating, compared with the aerodynamics of the vehicle, which effect performance throughout the trajectory. This suggests that, for maximum fly-back performance, the aerodynamic performance should be given preference over engine efficiency in the design of fly-back hypersonic accelerators.

### 6.2.3 Conclusion

The fly-back trajectory of the SPARTAN hypersonic vehicle is investigated, from separation at  $7.7^\circ\text{S}, 145.0^\circ\text{E}$  to landing at  $15.3^\circ\text{S}, 144.9^\circ\text{E}$ , corresponding to a near  $180^\circ$  turn and a fly-back of 878km. The aerodynamics of the SPARTAN are calculated using CART3D, an inviscid CFD package, over the range of Mach numbers and angle of attack values of flight. The optimal trajectory of the SPARTAN is

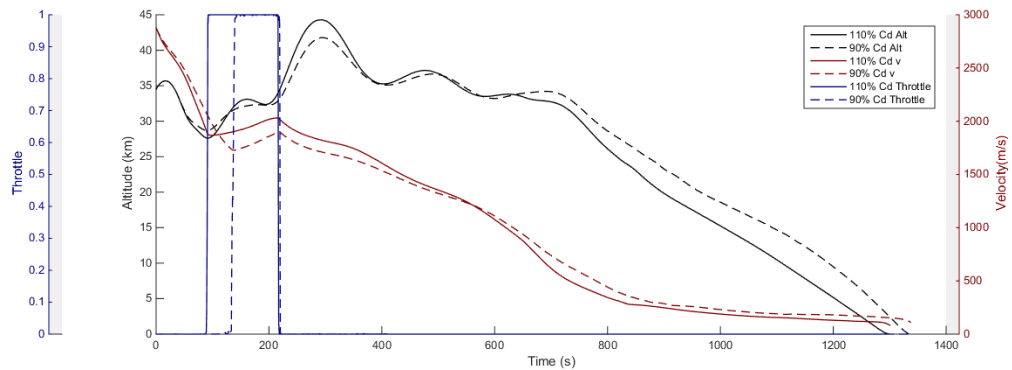


Figure 6.10: Comparison of optimal trajectories with  $\pm 10\%$   $C_D$  variance.

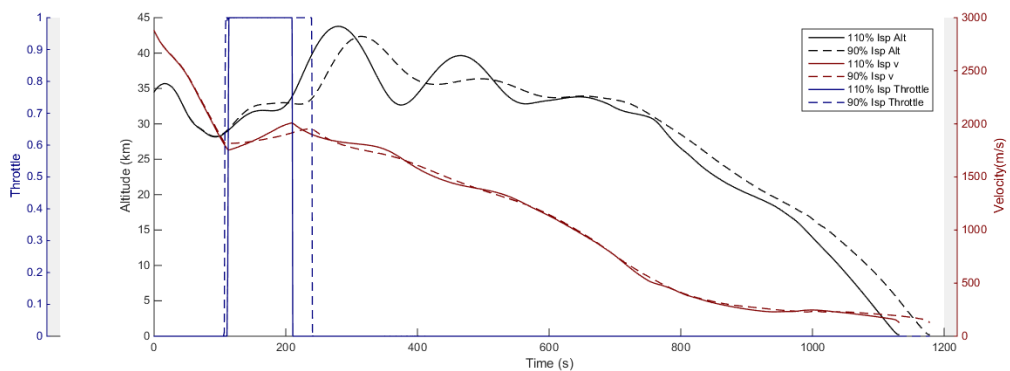


Figure 6.11: Comparison of optimal trajectories with  $\pm 10\%$   $I_{SP}$  variance.

calculated, to fly-back to the initial launch position with minimum fuel. The optimal trajectory is calculated using the launch vehicle optimal control program LODESTAR. It is found that the SPARTAN is capable of returning to its initial launch position, using 166.0kg of fuel. The optimal trajectory terminates when SPARTAN reaches 200m altitude at a velocity of 119.8m/s. After this point, it is assumed that the SPARTAN lands on a traditional runway, at similar conditions to the space shuttle. This result indicates that the fly-back of a hypersonic launch vehicle from high velocity separation at a Mach number greater than nine, returning to its initial launch site using scramjet hypersonic air-breathing engines, is feasible. This fly-back to the the original launch site is a crucial component for low cost access-to-space using scramjets.

The coefficient of drag of the SPARTAN and specific impulse of the scramjet engines were independently varied by  $\pm 10\%$  and the new optimal trajectories calculated to assess the robustness of the fly-back trajectory to uncertainties in vehicle aerodynamics and scramjet performance. It was found that a  $\pm 10\%$  variation in  $C_D$  results in a +31.0% or -34.9% variation in fuel mass burned during fly-back, while a  $\pm 10\%$  variation in  $I_{SP}$  results in a much smaller variation of -6.9% or +13.8%. These results indicate that the aerodynamics of a fly-back hypersonic accelerator are much more significant to the fly-back fuel usage than the performance of the scramjet engine.

---

---

## CHAPTER 7

---

### CONCLUSIONS

- The optimal ascent trajectory for the rocket-scramjet-rocket three stage launch system involves a pull-up before third stage release.
- The optimal fly-back of the SPARTAN involves several distinct stages, including a boost phase, skip phase and glide phase.
- Description of conclusions from the combined ascent/fly-back trajectory. The combined ascent and fly-back trajectory involves the SPARTAN banking during ascent, to mitigate the distance flown during the ascent trajectory.
- Summary of conclusions from third stage sizing analysis.

### 7.1 Recommendations for future work

- Further design optimisation incorporating trajectory optimisation.
- Sizing of entire system for optimal monetary cost efficiency.



---

## LIBRARY

- [1] Dineth Abeynayake and Alan Agon. “Comparison of computational and semi-empirical aerodynamics tools for making fit-for-purpose modelling decisions”. In: *20th International Congress on Modelling and Simulation*. December. Adelaide, Australia, 2013, pp. 1–6.
- [2] Xcor Aerospace. *Lynx Sspacecraft*. 2017. URL: <https://xcor.com/launch/lynx-spacecraft/> (visited on 11/30/2017).
- [3] Michael J. Aftosmis, Marian Nemec, and Susan E. Cliff. “Adjoint-based low-boom design with Cart3D”. In: *29th AIAA Applied Aerodynamics Conference 2011*. June. 2011, pp. 1–17. ISBN: 9781624101458. DOI: [doi:10.2514/6.2011-3500](https://doi.org/10.2514/6.2011-3500). URL: <http://www.scopus.com/inward/record.url?eid=2-s2.0-84872373928&partnerID=tZ0tx3y1>.
- [4] Airbus Defence and Spaces solution to reuse space Launchers. 2017. URL: <https://airbusdefenceandspaces.com/reuse-launchers/> (visited on 11/23/2017).
- [5] D Almosnino. “Assessment of an inviscid euler-adjoint solver for prediction of aerodynamic characteristics of the NASA HL-20 lifting body”. In: *34th AIAA Applied Aerodynamics Conference, 2016* June (2016). DOI: [10.2514/6.2016-3266](https://doi.org/10.2514/6.2016-3266). URL: [https://www.scopus.com/inward/record.uri?eid=2-s2.0-84980371959&partnerID=40&md5=1b304aabaa2976daf4d0742d5bdc6ba](http://www.scopus.com/inward/record.uri?eid=2-s2.0-84980371959&partnerID=40&md5=1b304aabaa2976daf4d0742d5bdc6ba).
- [6] Dan Almosnino. “A Low Subsonic Study of the NASA N2A Hybrid Wing-Body Using an Inviscid Euler-Adjoint Solver”. In: *34th AIAA Applied Aerodynamics Conference* June (2016), pp. 1–18. DOI: [doi:10.2514/6.2016-3267](https://doi.org/10.2514/6.2016-3267). URL: <http://dx.doi.org/10.2514/6.2016-3267>.
- [7] ARCA. *Haas2CA*. 2017. URL: <http://www.arcaspace.com/en/haas2c.htm> (visited on 12/01/2017).
- [8] Astos Solutions. *Astos Solutions*. 2018. URL: <https://www.astos.de/>.

- [9] Australia's hypersonic plane for a new space race. URL: <http://www.bbc.com/future/story/20161117-australias-hypersonic-spaceplane-for-a-new-space-race> (visited on 06/21/2018).
- [10] Mokhtar S. Bazaraa, Hanif D. Sherali, and C. M. Shetty. *Nonlinear Programming: Theory and Algorithms*. John Wiley & Sons, 2013.
- [11] Nazareth Bedrossian, Bastion Technologies, and Louis Nguyen Nasa. "Zero Propellant Maneuvre Flight Results For 180 Degree ISS Rotation". In: *20th International Symposium on Space Flight Dynamics*. Annapolis, MD, 2007.
- [12] John T. Betts. "Survey of Numerical Methods for Trajectory Optimization". In: *Journal of Guidance, Control, and Dynamics* 21.2 (1998), pp. 193–207. ISSN: 0731-5090. DOI: [10.2514/2.4231](https://doi.org/10.2514/2.4231).
- [13] F. S. Billig. "Research on supersonic combustion". In: *Journal of Propulsion and Power* 9.4 (1993), pp. 499–514. ISSN: 0748-4658. DOI: [10.2514/3.23652](https://doi.org/10.2514/3.23652).
- [14] Pt Boggs and Jw Tolle. "Sequential quadratic programming for large-scale nonlinear optimization". In: *Journal of Computational and Applied Mathematics* 124.1-2 (2000), pp. 123–137. ISSN: 03770427. DOI: [10.1016/S0377-0427\(00\)00429-5](https://doi.org/10.1016/S0377-0427(00)00429-5). URL: <http://linkinghub.elsevier.com/retrieve/pii/S0377042700004295> \$ \backslash http://www.sciencedirect.com/science/article/pii/S0377042700004295.
- [15] John Bradford et al. "Exploration of the design space for the ABLV-GT SSTO reusable launch vehicle". In: *Space 2000 Conference and Exposition* September (2000). DOI: [doi:10.2514/6.2000-5136](https://doi.org/10.2514/6.2000-5136). URL: <http://dx.doi.org/10.2514/6.2000-5136>.
- [16] R Bulirsch et al. "Combining direct and indirect methods in optimal control: Range maximization of a hang glider". In: *Optimal Control (Calculus of Variations, Optimal Control Theory and Numerical Methods)* 111 (1993), pp. 273–288.
- [17] Dong Chai et al. "Boost-skipping trajectory optimization for air-breathing hypersonic missile". In: *Aerospace Science and Technology* 46 (2015), pp. 506–513. ISSN: 12709638. DOI: [10.1016/j.ast.2015.09.004](https://doi.org/10.1016/j.ast.2015.09.004). URL: <http://dx.doi.org/10.1016/j.ast.2015.09.004>.
- [18] Stephen Clark. *Falcon 9 rocket launching Sunday sports fin upgrade*. 2018. URL: <https://spaceflightnow.com/2017/06/25/falcon-9-rocket-launching-sunday-sports-fin-upgrade/> (visited on 06/21/2018).
- [19] William Colson. *Program to Optimize Simulated Trajectories* 2. 2017. URL: <https://post2.larc.nasa.gov/>.

- [20] a. C. Composites. “<http://www.corkcomposites.amorim.com/images/livraria/TPS%20brochure.pdf>”. In: *Consultado em Março de 2014* ().
- [21] Stephen Cook and Uwe Hueter. “NASA’s Integrated Space Transportation Plan 3rd generation reusable launch vehicle technology update”. In: *Acta Astronautica* 53.4-10 (2003), pp. 719–728. ISSN: 00945765. DOI: [10.1016/S0094-5765\(03\)00113-9](https://doi.org/10.1016/S0094-5765(03)00113-9).
- [22] Edward T. Curran. “Scramjet Engines: The First Forty Years”. In: *Journal of Propulsion and Power* 17.6 (2001), pp. 1138–1148. ISSN: 0748-4658. DOI: [10.2514/2.5875](https://doi.org/10.2514/2.5875). URL: <http://arc.aiaa.org/doi/10.2514/2.5875>.
- [23] Edward T. Curran. “Scramjet Engines: The First Forty Years”. In: *Journal of Propulsion and Power* 17.6 (2001), pp. 1138–1148. ISSN: 0748-4658. DOI: [10.2514/2.5875](https://doi.org/10.2514/2.5875).
- [24] E.T. Curran. *Scramjet Propulsion*. Progress in Astronautics and Aeronautics, 2001. ISBN: 978-1-60086-660-9.
- [25] F. Curran et al. “The Benefits of Hypersonic Airbreathing Launch Systems for Access to Space”. In: *39th AIAA/ASME/SAE/ASEE Joint Propulsion Conference and Exhibit* July (2003), pp. 1–14. DOI: [10.2514/6.2003-5265](https://doi.org/10.2514/6.2003-5265). URL: <http://arc.aiaa.org/doi/10.2514/6.2003-5265>.
- [26] Derek Dalle, Sean Torrez, and James Driscoll. “Turn Performance of an Air-Breathing Hypersonic Vehicle”. In: *AIAA Atmospheric Flight Mechanics Conference* August (2011). DOI: [10.2514/6.2011-6300](https://doi.org/10.2514/6.2011-6300). URL: <http://arc.aiaa.org/doi/10.2514/6.2011-6300>.
- [27] Derek J. Dalle et al. “Minimum-Fuel Ascent of a Hypersonic Vehicle Using Surrogate Optimization”. In: *Journal of Aircraft* 51.6 (2014), pp. 1973–1986. ISSN: 0021-8669. DOI: [10.2514/1.C032617](https://doi.org/10.2514/1.C032617). URL: <http://arc.aiaa.org/doi/10.2514/1.C032617>.
- [28] Christopher L. Darby, William W. Hager, and Anil V. Rao. “An hp-adaptive pseudospectral method for solving optimal control problems”. In: *Optimal Control Applications and Methods* 32.3 (2011), pp. 476–502. DOI: [10.1002/oca.957](https://doi.org/10.1002/oca.957). URL: <http://doi.wiley.com/10.1002/oca.957>.
- [29] Christopher L. Darby, William W. Hager, and Anil V. Rao. “Direct Trajectory Optimization Using a Variable Low-Order Adaptive Pseudospectral Method”. In: *Journal of Spacecraft and Rockets* 48.3 (2011), pp. 433–445. ISSN: 0022-4650. DOI: [10.2514/1.52136](https://doi.org/10.2514/1.52136).
- [30] By Alfred J Eggers, H Julian Allen, and Stanford E Neice. “Technical Note 4046”. In: October (1957).
- [31] Thino Eggers. “Aerodynamic Analysis of the Dual-Mode Ramjet Vehicle JAPHAR”. In: *Notes on Numerical Fluid Mechanics and Multidisciplinary Design*. Vol. 115. 2011, pp. 137–140. ISBN: 9783642177699.

- [32] F. Fahroo and I.M. Ross. “Direct trajectory optimization by a Chebyshev pseudospectral method”. In: *Proceedings of the 2000 American Control Conference*. Chicago, IL, 2000, pp. 3860–3864. ISBN: 0-7803-5519-9. DOI: [10.1109/ACC.2000.876945](https://doi.org/10.1109/ACC.2000.876945).
- [33] Fariba Fahroo and I. Michael Ross. “Costate Estimation by a Legendre Pseudospectral Method”. In: *Journal of Guidance, Control, and Dynamics* 24.2 (2001), pp. 270–277. ISSN: 0731-5090. DOI: [10.2514/2.4709](https://doi.org/10.2514/2.4709).
- [34] Rob Falck. *OTIS*. 2016. URL: <https://otis.grc.nasa.gov/index.html>.
- [35] Giorgio Fasano and Janos Pinter. *Modelling and Optimisation in Space Engineering*. New York, NY: Springer, 2013. DOI: [10.1007/978-1-4614-4469-5](https://doi.org/10.1007/978-1-4614-4469-5).
- [36] E. Fitzer and L.M. Manocha. *Carbon Reinforcements and Carbon/Carbon Composites*. Berlin, Heidelberg: Springer Berlin Heidelberg, 1998. ISBN: 3-642-58745-3.
- [37] Kevin W. Flaherty, Katherine M. Andrews, and Glenn W. Liston. “Operability Benefits of Airbreathing Hypersonic Propulsion for Flexible Access to Space”. In: *Journal of Spacecraft and Rockets* 47.2 (2010), pp. 280–287. ISSN: 0022-4650. DOI: [10.2514/1.43750](https://doi.org/10.2514/1.43750). URL: <http://arc.aiaa.org/doi/abs/10.2514/1.43750>.
- [38] Sholto O. Forbes-Spyratos et al. “Trajectory Design of a Rocket-Scramjet-Rocket Multi-Stage Launch System”. In: *Journal of Spacecraft and Rockets - Under Consideration* TBD (2018).
- [39] S.O. Forbes-Spyratos et al. “Trajectory design of a rocket-scramjet-rocket multi-stage launch system”. In: *21st AIAA International Space Planes and Hypersonics Technologies Conference, Hypersonics 2017*. Xiamen, China, 2017. ISBN: 9781624104633.
- [40] Jeff Foust. *SpaceX achievements generate growing interest in reusable launchers*. 2018. URL: <http://spacenews.com/spacex-achievements-generate-growing-interest-in-reusable-launchers/> (visited on 06/21/2018).
- [41] Ronald S. Fry. “A Century of Ramjet Propulsion Technology Evolution”. In: *Journal of Propulsion and Power* 20.1 (2004), pp. 27–58. ISSN: 0748-4658. DOI: [10.2514/1.9178](https://doi.org/10.2514/1.9178). URL: <http://arc.aiaa.org/doi/10.2514/1.9178>.
- [42] D Garg, Ma Patterson, and Ww Hager. “An Overview of Three Pseudospectral Methods for the Numerical Solution of Optimal Control Problems”. In: *Advances in thAstronautical Sciences* 135 (2009), pp. 1–17. URL: <http://vdol.mae.ufl.edu/ConferencePublications/unifiedFrameworkAAS.pdf>.
- [43] Adam Gilmour. *ROCKET STARTUP SHOOTS FOR THE STARS WITH AUD 5 MILLION (USD 3 . 7 MILLION ) SERIES A FUNDING*. 2017.

- [44] Reynaldo Gomez et al. “STS-107 Investigation Ascent CFD Support”. In: *34th AIAA Fluid Dynamics Conference and Exhibit* (2004), pp. 1–15. DOI: [10.2514/6.2004-2226](https://doi.org/10.2514/6.2004-2226). URL: <http://arc.aiaa.org/doi/10.2514/6.2004-2226>.
- [45] Chunlin Gong, Bing Chen, and Liangxian Gu. “Design and Optimization of RBCC Powered Suborbital Reusable Launch Vehicle”. In: *19th AIAA International Space Planes and Hypersonic Systems and Technologies Conference* June (2014), pp. 1–20. DOI: [10.2514/6.2014-2361](https://doi.org/10.2514/6.2014-2361). URL: <http://arc.aiaa.org/doi/abs/10.2514/6.2014-2361>.
- [46] Qi Gong, I. Michael Ross, and Friba Fahroo. “Costate Computation by a Chebyshev Pseudospectral Method”. In: *Journal of Guidance, Control, and Dynamics* 33.2 (2010), pp. 623–628. ISSN: 0731-5090. DOI: [10.2514/1.45154](https://doi.org/10.2514/1.45154).
- [47] William Heiser et al. *Hypersonic Airbreathing Propulsion*. the American Institute of Aeronautics and Astronautics, 1994. ISBN: 978-1-56347-035-6.
- [48] Heiser H. H. and D T Pratt. *Hypersonic Airbreathing Propulsion*. Washington, D.C: American Institute of Aeronautics and Astronautics, 1994, p. 11. ISBN: 1-56347-035-7. DOI: [10.2514/4.470356](https://doi.org/10.2514/4.470356).
- [49] Barry Mark Hellman. *Comparison of Return to Launch Site Options for a Reusable Booster Stage*. Tech. rep. Space Sytems Design Lab, Georgia Institute of technology, 2005, pp. 1–18.
- [50] H. Hindi. “A tutorial on convex optimization II: duality and interior point methods”. In: *2006 American Control Conference* 1 (2006), 11 pp. ISSN: 07431619. DOI: [10.1109/ACC.2006.1655436](https://doi.org/10.1109/ACC.2006.1655436). URL: <http://ieeexplore.ieee.org/document/1655436/>.
- [51] Horizon. *Black Arrow* 2. 2017. URL: <http://www.horizonsas.com/products/> (visited on 12/01/2017).
- [52] B Houska, H.J Ferrau, and M. Diehl. “ACADO Toolkit – An Open Source Framework for Automatic Control and Dynamic Optimization”. In: *Optimal Control Applications and Methods* 32.3 (2011), pp. 298–312.
- [53] Gt Huntington, David Benson, and Av Rao. “A Comparison of Accuracy and Computational Efficiency of Three Pseudospectral Methods”. In: *AIAA Guidance, Navigation and Control Conference and Exhibit* (2007), pp. 1–43. DOI: [10.2514/6.2007-6405](https://doi.org/10.2514/6.2007-6405). URL: <http://arc.aiaa.org/doi/abs/10.2514/6.2007-6405> \$\\backslash\$ <http://arc.aiaa.org/doi/pdf/10.2514/6.2007-6405>.
- [54] Thomas Jazra, Dawid Preller, and Michael K. Smart. “Design of an Airbreathing Second Stage for a Rocket-Scramjet-Rocket Launch Vehicle”. In: *Journal of Spacecraft and Rockets* 50.2 (2013), pp. 411–422. ISSN: 0022-4650. DOI: [10.2514/1.A32381](https://doi.org/10.2514/1.A32381). URL: <http://arc.aiaa.org/doi/abs/10.2514/1.A32381>.

- [55] D. Jezewski. “An Optimal, Analytic Solution to the Linear-Gravity, Constant-Thrust Trajectory Problem”. In: *Journal of Spacecraft and Rockets* July (1971), pp. 793–796.
- [56] *JModelica.org*. URL: <https://jmodelica.org/>.
- [57] Scott Josselyn and I Michael Ross. “Rapid Verification Method for the Trajectory Optimization of Reentry Vehicles”. In: *Notes* 26.3 (2002), pp. 505–508. ISSN: 0731-5090. DOI: [10.2514/2.5074](https://doi.org/10.2514/2.5074).
- [58] Takeshi Kanda and Tetsuo Hiraiwa. “Evaluation of Effectiveness of Periodic Flight by a Hypersonic Vehicle”. In: *Journal of Aircraft* 44.6 (2007), pp. 2076–2077. ISSN: 0021-8669. DOI: [10.2514/1.31143](https://doi.org/10.2514/1.31143).
- [59] Takeshi Kanda and Kenji Kudo. “Payload to Low Earth Orbit by Aerospace Plane with Scramjet Engine Summary”. In: *Journal of Propulsion and Power Technical Notes* 13.1 (1996), pp. 164–166. ISSN: 0748-4658. DOI: [10.2514/2.7641](https://doi.org/10.2514/2.7641).
- [60] Yoshiaki Kawajir, Carl D Laird, and Andreas Waechter. “Introduction to IPOPT: A tutorial for downloading, installing, and using IPOPT .” In: *Most* (2010), pp. 1–68. ISSN: 00981354. DOI: [http://web.mit.edu/ipopt\\\_v3.8/doc/documentation.pdf](http://web.mit.edu/ipopt\_v3.8/doc/documentation.pdf). arXiv: [arXiv:1011.1669v3](https://arxiv.org/abs/1011.1669v3).
- [61] Matthew P Kelly. “Transcription Methods for Trajectory Optimization A beginners tutorial”. In: (2015), pp. 1–14.
- [62] Randy Kendall and Pete Portanova. *Launch Vehicles Then and Now: 50 Years of Evolution*. 2010. URL: <http://www.aerospace.org/crosslinkmag/spring-2010/launch-vehicles-then-and-now-50-years-of-evolution/> (visited on 06/21/2018).
- [63] Andrew D Ketsdever et al. “Overview of Advanced Concepts for Space Access”. In: *Journal of Spacecraft and Rockets* 47.2 (2010), pp. 238–250. ISSN: 0022-4650. DOI: [10.2514/1.46148](https://doi.org/10.2514/1.46148).
- [64] RI Kimmel et al. “HIFiRE-5 flight vehicle design”. In: *AIAA paper* July (2010), pp. 1–17. DOI: [10.2514/6.2010-4985](https://doi.org/10.2514/6.2010-4985). URL: <http://arc.aiaa.org/doi/pdf/10.2514/6.2010-4985>.
- [65] Masatoshi Kodera et al. “Multi-Objective Design and Trajectory Optimization of Space Transport Systems with RBCC Propulsion via Evolutionary Algorithms and Pseudospectral Methods”. In: *52nd Aerospace Sciences Meeting* January (2014), pp. 1–14. DOI: [10.2514/6.2014-0629](https://doi.org/10.2514/6.2014-0629). URL: <http://arc.aiaa.org/doi/10.2514/6.2014-0629>.
- [66] Heinz-Otto Kreiss and Joseph Oliger. “Comparison of accurate methods for the integration of hyperbolic equations”. In: *Tellus A* 1971 (1972). ISSN: 0280-6495. DOI: [10.3402/tellusa.v24i3.10634](https://doi.org/10.3402/tellusa.v24i3.10634).

- [67] *Kuai Zhou (Fast Vessel)*. URL: <https://chinaspacereport.com/launch-vehicles/kuaizhou/> (visited on 12/01/2017).
- [68] Markus Kuhn et al. “Innovative European Launcher Concept SMILE”. In: *21st AIAA International Space Planes and Hypersonics Technologies Conference* March (2017), pp. 1–14. DOI: [10.2514/6.2017-2441](https://arc.aiaa.org/doi/10.2514/6.2017-2441). URL: <https://arc.aiaa.org/doi/10.2514/6.2017-2441>.
- [69] Roger D. Launius. “Assessing the legacy of the Space Shuttle”. In: *Space Policy* 22.4 (2006), pp. 226–234. ISSN: 02659646. DOI: [10.1016/j.spacepol.2006.08.008](https://doi.org/10.1016/j.spacepol.2006.08.008).
- [70] Sarah Lewin. *Blue Origin Announces Big 'New Glenn' Rocket for Satellite & Crew Launches*. 2016. URL: <https://www.space.com/34034-blue-origin-new-glenn-rocket-for-satellites-people.html> (visited on 06/21/2018).
- [71] Huifeng Li et al. “Footprint problem with angle of attack optimization for high lifting reentry vehicle”. In: *Chinese Journal of Aeronautics* 25.2 (2012), pp. 243–251. ISSN: 10009361. DOI: [10.1016/S1000-9361\(11\)60384-1](https://doi.org/10.1016/S1000-9361(11)60384-1). URL: [http://dx.doi.org/10.1016/S1000-9361\(11\)60384-1](http://dx.doi.org/10.1016/S1000-9361(11)60384-1).
- [72] Ping Lu. “Inverse dynamics approach to trajectory optimization for an aerospace plane”. In: *Journal of Guidance, Control, and Dynamics* 16.4 (1993), pp. 726–732. ISSN: 0731-5090. DOI: [10.2514/3.21073](https://arc.aiaa.org/doi/abs/10.2514/3.21073). URL: <http://arc.aiaa.org/doi/abs/10.2514/3.21073>.
- [73] J W Magee Bruno, T.J., Friend, D. G., Huber, M.L., Laesecke, A., Lemmon, E.W., McLinden, M.O., Perkins, R.A., Baranski, J., Widegren, J.A. *Thermophysical Properties Measurements and Models for Rocket Propellant RP-1: Phase I, NIST- IR 6644*, National Institute of Standards and Technology (U.S.) Tech. rep. 2006.
- [74] Unmeel Mehta et al. “Skylon Aerospace Plane and Its Aerodynamics and Plumes”. In: *Journal of Spacecraft and Rockets* 53.2 (2016), pp. 340–353. ISSN: 0022-4650. DOI: [10.2514/1.A33408](https://arc.aiaa.org/doi/10.2514/1.A33408). URL: <http://arc.aiaa.org/doi/10.2514/1.A33408>.
- [75] Unmeel B. Mehta and Jeffrey V. Bowles. “Two-Stage-to-Orbit Spaceplane Concept with Growth Potential”. In: *Journal of Propulsion and Power* 17.6 (2001), pp. 1149–1161. ISSN: 0748-4658. DOI: [10.2514/2.5886](https://arc.aiaa.org/doi/10.2514/2.5886).
- [76] Dave Mosher. *SpaceX faces a growing list of competitors in the new space race*. 2018. URL: <https://www.businessinsider.com.au/spacex-elon-musk-competition-companies-rockets-2018-3> (visited on 06/21/2018).
- [77] Nathan D. Moshman and Ronald J. Proulx. “Range Improvements in Gliding Reentry Vehicles from Thrust Capability”. In: *Journal of Spacecraft and Rockets* 51.5 (2014), pp. 1681–1694. ISSN: 0022-4650. DOI: [10.2514/1.A32764](https://arc.aiaa.org/doi/10.2514/1.A32764). URL: <http://arc.aiaa.org/doi/10.2514/1.A32764>.

- [78] NASA. *U.S. Standard Atmosphere, 1976*. U.S. Government Printing Office, Washington, D.C., 1976, pp. 1–243. URL: <http://ntrs.nasa.gov/archive/nasa/casi.ntrs.nasa.gov/19770009539.pdf>.
- [79] NASA Glenn Research Center. *Euler Equations*. URL: <https://www.grc.nasa.gov/WWW/k-12/airplane/eulereqs.html>.
- [80] Yuanbo Nie, Omar Faqir, and Eric Kerrigan. *ICLOCS2*. 2018. URL: <http://www.ee.ic.ac.uk/ICLOCS/>.
- [81] Carlos Niederstrasser and Warren Frick. “Small Launch Vehicles A 2015 State of the Industry Survey”. In: *Proceedings of the 29th Annual AIAA/USU Conference on Small Satellites* (2015).
- [82] J.R. Olds and I.a. Budianto. “Constant Dynamic Pressure Trajectory Simulation with POST”. In: *Aerospace Sciences Meeting & Exhibit*. Reno, NV, 1998, pp. 1–13. DOI: [10.2514/6.1998-302](https://doi.org/10.2514/6.1998-302). URL: <http://citeserx.ist.psu.edu/viewdoc/download?doi=10.1.1.25.6506&rep=rep1&type=pdf>.
- [83] Orbital Access. *The Orbital 500R*. 2017. URL: <http://www.orbital-access.com/the-orbital-500/> (visited on 12/01/2017).
- [84] DARPA Outreach. *DARPA Picks Design for Next-Generation Spaceplane*. 2017. URL: <https://www.darpa.mil/news-events/2017-05-24> (visited on 11/16/2017).
- [85] Shishir Pandya, Scott Murman, and Michael Aftosmis. “Validation of Inlet and Exhaust Boundary Conditions for a Cartesian Method”. In: *22nd Applied Aerodynamics Conference and Exhibit January* (2004), pp. 1–16. ISSN: 10485953. DOI: [10.2514/6.2004-4837](https://doi.org/10.2514/6.2004-4837). URL: <http://arc.aiaa.org/doi/10.2514/6.2004-4837>.
- [86] A Paull, R.J Stalker, and D Mee. “Thrust Measurements of a Complete Axisymmetric Scramjet in an Impulse Facility”. In: *5TH INTERNATIONAL AEROSPACE PLANES AND HYPERSONICS TECHNOLOGIES CONFERENCE*. 1993.
- [87] Fabrizio Pescetelli et al. “Ascent Trajectory Optimisation for a Single-Stage-to-Orbit Vehicle with Hybrid Propulsion”. In: *18th AIAA/3AF International Space Planes and Hypersonic Systems and Technologies Conference*. September. 2012, pp. 1–18. ISBN: 978-1-60086-931-0. DOI: [10.2514/6.2012-5828](https://doi.org/10.2514/6.2012-5828). URL: <http://arc.aiaa.org/doi/abs/10.2514/6.2012-5828>.
- [88] Harry Pettit. *The galaxy's fastest car*. 2018. URL: <http://www.dailymail.co.uk/sciencetech/article-5361789/Ride-Elon-Musks-Starman-travels-space.html> (visited on 06/21/2018).

- [89] Richard W. Powell et al. “Ascent performance of an air-breathing horizontal-takeoff launch vehicle”. In: *Journal of Guidance, Control, and Dynamics* 14.4 (1991), pp. 834–839. ISSN: 0731-5090. DOI: [10.2514/3.20719](https://doi.org/10.2514/3.20719).
- [90] Dawid Preller. “Multidisciplinary Design and Optimisation of a Pitch Trimmed Hypersonic Airbreathing Accelerating Vehicle”. PhD thesis. University of Queensland, 2018.
- [91] Dawid Preller and Michael Smart. “Reusable Launch of Small Satellites using Scramjets”. In: *Journal of Spacecraft and Rockets* (2017).
- [92] Dawid Preller and Michael K Smart. “Longitudinal Control Strategy for Hypersonic Accelerating Vehicles”. In: *Journal of Spacecraft and Rockets* 52.3 (2015), pp. 1–6. ISSN: 0022-4650. DOI: [10.2514/1.A32934](https://doi.org/10.2514/1.A32934). URL: <http://dx.doi.org/10.2514/1.A32934>.
- [93] Dawid Preller and Michael K. Smart. “Reusable Launch of Small Satellites Using Scramjets”. In: *Journal of Spacecraft and Rockets* 54.6 (2017), pp. 1–13. ISSN: 0022-4650. DOI: [10.2514/1.A33610](https://doi.org/10.2514/1.A33610). URL: <https://arc.aiaa.org/doi/10.2514/1.A33610>.
- [94] Dawid Preller and Michael K. Smart. “Scramjets for Reusable Launch of Small Satellites”. In: *Journal of Spacecraft and Rockets* Advance On (2017), pp. 1–13. ISSN: 0022-4650. DOI: [10.2514/6.2015-3586](https://doi.org/10.2514/6.2015-3586). URL: <http://arc.aiaa.org/doi/10.2514/6.2015-3586>.
- [95] Patrizia Pucci and James B Serrin. *The maximum principle*. Tech. rep. 2007, pp. 80–104.
- [96] Ligy Susan Punnoose, Madan Lal, and V Brinda. “On-Line Trajectory Optimization of a Typical Air-Breathing Launch Vehicle using Energy State Approximation Approach”. In: *Advances in Control and Optimization of Dynamical Systems* (2007), pp. 296–302.
- [97] Anil V. Rao et al. “Algorithm 902”. In: *ACM Transactions on Mathematical Software* 37.2 (2010), pp. 1–39. ISSN: 00983500. DOI: [10.1145/1731022.1731032](https://doi.org/10.1145/1731022.1731032).
- [98] Av Rao. “A survey of numerical methods for optimal control”. In: *Advances in the Astronautical Sciences* 135 (2009), pp. 497–528. URL: <http://vdol.mae.ufl.edu/ConferencePublications/trajectorySurveyAAS.pdf>.
- [99] Richard Webb. “Is It Worth It? The Economics of Reusable Space Transportation”. In: *ICEAA 2016 International Training Symposium, Bristol, UK* (2016), pp. 1–19.
- [100] S. Tauqeer Ul Islam Rizvi, Lin Shu He, and Da Jun Xu. “Optimal trajectory and heat load analysis of different shape lifting reentry vehicles for medium range application”. In: *Defence Technology* 11.4 (2015), pp. 350–361. ISSN: 22149147. DOI: [10.1016/j.dt.2015.06.003](https://doi.org/10.1016/j.dt.2015.06.003). URL: <http://dx.doi.org/10.1016/j.dt.2015.06.003>.
- [101] Joseph M Roche and Daniel N Kosareo. *Structural Sizing of a 25000-Lb Payload , Air-Breathing Launch Vehicle for Single-Stage-To-Orbit*. Tech. rep. January 2001. 2000.

- [102] Rocket Lab. *Electron*. 2016. URL: <https://www.rocketlabusa.com/electron/> (visited on 11/30/2017).
- [103] RocketCrafters. *Intrepid-1*. 2017. URL: <http://rocketcrafters.space/products-services/intrepid-launcher-family/intrepid-1/> (visited on 12/01/2017).
- [104] I M Ross and F Fahroo. “A direct method for solving nonsmooth optimal control problems”. In: *Proceedings of the 2002 {IFAC World Congress}* (2002).
- [105] I. Michael Ross and Fariba Fahroo. “Pseudospectral Knotting Methods for Solving Nonsmooth Optimal Control Problems”. In: *Journal of Guidance, Control, and Dynamics* 27.3 (2004), pp. 397–405. ISSN: 0731-5090. DOI: [10.2514/1.3426](https://doi.org/10.2514/1.3426).
- [106] P E Rutquist and M M Edvall. “PROPT - Matlab Optimal Control Software”. In: *Tomlab Optimization Inc* 260 (2010), pp. –.
- [107] Jeanne Ryba. *Space Shuttle*. 2017. URL: [https://www.nasa.gov/mission\\_pages/shuttle/launch/landing101.html](https://www.nasa.gov/mission_pages/shuttle/launch/landing101.html) (visited on 11/27/2017).
- [108] Denton G. Sagerman et al. “Comparisons of Measured and Modeled Aero-thermal Distributions for Complex Hypersonic Configurations”. In: *55th AIAA Aerospace Sciences Meeting* January (2017), pp. 1–22. DOI: [10.2514/6.2017-0264](https://doi.org/10.2514/6.2017-0264). URL: <http://arc.aiaa.org/doi/10.2514/6.2017-0264>.
- [109] Marti Sarigul-Klijn and Nesrin Sarigul-Klijn. “Flight Mechanics of Manned Sub-Orbital Reusable Launch Vehicles with Recommendations for Launch and Recovery”. In: *41st Aerospace Sciences Meeting and Exhibit, Aerospace Sciences Meetings*. Reno, NV, 2003.
- [110] Corin Segal. *The Scramjet Engine: Processes and Characteristics*. Cambridge, UK: Cambridge University Press, 2009, p. 229. ISBN: 9780521838153.
- [111] John D Shaughnessy, S Zane Pinckney, and John D McMinn. “Hypersonic Vehicle Simulation Configuration Model : Winged-Cone Configuration”. In: (1990).
- [112] M Smart. “Scramjets”. In: 3219 (2007).
- [113] Michael Smart. *Scramjet Inlets*. Tech. rep. 9. The University of Queensland, 2010, pp. 1–24. DOI: [10.2514/5.9781600866609.0447.0511](https://doi.org/10.2514/5.9781600866609.0447.0511).
- [114] Michael K. Smart. “How Much Compression Should a Scramjet Inlet Do?” In: *AIAA Journal* 50.3 (2012), pp. 610–619. ISSN: 0001-1452. DOI: [10.2514/1.J051281](https://doi.org/10.2514/1.J051281). URL: <http://arc.aiaa.org/doi/10.2514/1.J051281>.
- [115] Michael K Smart and Edward G Ruf. “Free-jet testing of a {REST} scramjet at off-design conditions”. In: *Collection of Technical Papers - 25th AIAA Aerodynamic Measurement Technology and Ground Testing Conference* AIAA 2006-2955 (2006), pp. 190–201. DOI: [doi:10.2514/6.2006-2955](https://doi.org/10.2514/6.2006-2955).

- [116] Michael K. Smart and Matthew R. Tetlow. “Orbital Delivery of Small Payloads Using Hypersonic Airbreathing Propulsion”. In: *Journal of Spacecraft and Rockets* 46.1 (2009), pp. 117–125. ISSN: 0022-4650. DOI: [10.2514/1.38784](https://doi.org/10.2514/1.38784).
- [117] Michael K. Smart and Matthew R. Tetlow. “Orbital Delivery of Small Payloads Using Hypersonic Airbreathing Propulsion”. In: *Journal of Spacecraft and Rockets* 46.1 (2009), pp. 117–125. ISSN: 0022-4650. DOI: [10.2514/1.38784](https://doi.org/10.2514/1.38784). URL: <http://arc.aiaa.org/doi/abs/10.2514/1.38784>.
- [118] Thomas J. Sooy and Rebecca Z. Schmidt. “Aerodynamic Predictions, Comparisons, and Validations Using Missile DATCOM (97) and Aeroprediction 98 (AP98)”. In: *Journal of Spacecraft and Rockets* 42.2 (2005), pp. 257–265. ISSN: 0022-4650. DOI: [10.2514/1.7814](https://doi.org/10.2514/1.7814).
- [119] Space Exploration technologies. *Falcon 1 Launch Vehicle Payload Users Guide*. Tech. rep. Hawthorne, CA: Space Exploration Technologies, 2008, p. 65.
- [120] O. Stryk and R. Bulirsch. “Direct and indirect methods for trajectory optimization”. In: *Annals of Operations Research* 37 (1992), pp. 357–373. ISSN: 0254-5330. DOI: [10.1007/BF02071065](https://doi.org/10.1007/BF02071065).
- [121] M Suraweera and M K Smart. “Shock Tunnel Experiments with a Mach 12 {REST} Scramjet at Off-Design Conditions”. In: *Journal of Propulsion and Power* 25.3 (2009), pp. 555–564. ISSN: 0748-4658. DOI: [10.2514/1.37946](https://doi.org/10.2514/1.37946).
- [122] George Sutton and Oscar Biblarz. *Rocket propulsion Elements*. 8th. John Wiley & Sons, 2010, p. 67. ISBN: 978-0470080245. DOI: [10.1017/S0001924000034308](https://doi.org/10.1017/S0001924000034308).
- [123] M R Tetlow et al. “Comparison of Glideback and Flyback Boosters”. In: *Journal of Spacecraft and Rockets* 38.5 (1992), pp. 752–758. ISSN: 0022-4650. DOI: [10.2514/2.3742](https://doi.org/10.2514/2.3742). URL: <http://dx.doi.org/10.2514/2.3742>.
- [124] The MathWorks Inc. *MATLAB and Optimization Toolbox Release 2014b*. Natick, Massachusetts, United States., 2014. URL: [www.mathworks.com](http://www.mathworks.com).
- [125] Bailing Tian and Qun Zong. “Optimal guidance for reentry vehicles based on indirect Legendre pseudospectral method”. In: *Acta Astronautica* 68.7-8 (2011), pp. 1176–1184. ISSN: 0045-765. DOI: [10.1016/j.actaastro.2010.10.010](https://doi.org/10.1016/j.actaastro.2010.10.010). URL: <http://linkinghub.elsevier.com/retrieve/pii/S004576510003899>.
- [126] *To Challenge SpaceX, Rockets Get Wings*. 2016. URL: <http://www.spacesafetymagazine.com/news/to-challenge-spacex-rockets-get-wings/> (visited on 06/21/2018).
- [127] Federico Toso et al. “Optimisation of ascent and descent trajectories for lifting body space access vehicles”. In: *66th International Astronautical Congress*. Jerusalem, 2015.

- [128] Charles Trefny. “An Air-Breathing Concept Launch Vehicle for Single-Stage-to-Orbit”. In: *35th Joint Propulsion Conference and Exhibit*. May. Los Angeles, CA, 1999. DOI: [10.2514/6.1999-2730](https://doi.org/10.2514/6.1999-2730).
- [129] Takeshi Tsuchiya and Takashige Mori. “Optimal Design of Two-Stage-To-Orbit Space Planes with Airbreathing Engines”. In: *Journal of Spacecraft and Rockets* 42.1 (2005), pp. 90–97. ISSN: 0022-4650. DOI: [10.2514/1.8012](https://doi.org/10.2514/1.8012).
- [130] Richard Varvill and Alan Bond. “THE SKYLON SPACEPLANE : PROGRESS TO REALISATION”. In: *Journal of the British Interplanetary Society* 61 (2008), pp. 412–418.
- [131] Vector Space. *Vector Launch Vehicle Family*. 2017. URL: <https://vectorspacesystems.com/technology/> (visited on 12/01/2017).
- [132] VirginOrbit. *LauncherOne*. 2017. URL: <https://virginorbit.com/> (visited on 11/30/2017).
- [133] a Wächter and L T Biegler. *On the Implementation of a Primal-Dual Interior Point Filter Line Search Algorithm for Large-Scale Nonlinear Programming*. Vol. 106. 1. 2006, pp. 25–57. ISBN: 1010700405.
- [134] Mark Wade. *Encyclopedia Astronautica*. 2017. URL: <http://www.astronautix.com/>.
- [135] Dennis Wassel et al. “the Esa Nlp-Solver Worhp Recent Developments and Applications”. In: *Modeling and Optimization in Space Engineering* x (2013).
- [136] Alan W. Wilhite et al. “Technology and staging effects on two-stage-to-orbit systems”. In: *Journal of Spacecraft and Rockets* 31.1 (1991), pp. 31–39. ISSN: 0022-4650. DOI: [10.2514/3.26399](https://doi.org/10.2514/3.26399).
- [137] Shengbo Yang et al. “Trajectory optimization for a ramjet-powered vehicle in ascent phase via the Gauss pseudospectral method”. In: *Aerospace Science and Technology* 67 (2017), pp. 88–95. ISSN: 12709638. DOI: [10.1016/j.ast.2017.04.001](https://doi.org/10.1016/j.ast.2017.04.001). URL: <http://dx.doi.org/10.1016/j.ast.2017.04.001>.
- [138] David Young et al. “Lazarus: A SSTO Hypersonic Vehicle Concept Utilizing RBCC and HEDM Propulsion Technologies”. In: *14th AIAA/AHI Space Planes and Hypersonic Systems and Technologies Conference*. 2006, pp. 1–15. ISBN: 978-1-62410-050-5. DOI: [10.2514/6.2006-8099](https://doi.org/10.2514/6.2006-8099). URL: <http://arc.aiaa.org/doi/10.2514/6.2006-8099>.
- [139] Zero2Infinity. *Bloostar*. 2016. URL: <http://www.zero2infinity.space/bloostar/> (visited on 11/30/2017).
- [140] Jiang Zhao and Rui Zhou. “Reentry trajectory optimization for hypersonic vehicle satisfying complex constraints”. In: *Chinese Journal of Aeronautics* 26.6 (2013), pp. 1544–1553. ISSN: 10009361. DOI: [10.1016/j.cja.2013.10.009](https://doi.org/10.1016/j.cja.2013.10.009). URL: <http://dx.doi.org/10.1016/j.cja.2013.10.009>.

---

---

## APPENDIX A

---

### TRAJECTORY RESULTS

-engine data with trajectory paths

-mesh histories



---

---

## APPENDIX B

---

### CART3D RESULTS

#### B.1 Engine-On Plume Check

-simulate engine-on conditions to check that the plumes do not adversely affect the tail of the vehicle  
(justify that I can just remove engines/boattail)

-Mach 5,7,9 at 50kPa

#### B.2 CART3D Results

-include mesh here

## APPENDIX B. CART3D RESULTS

---

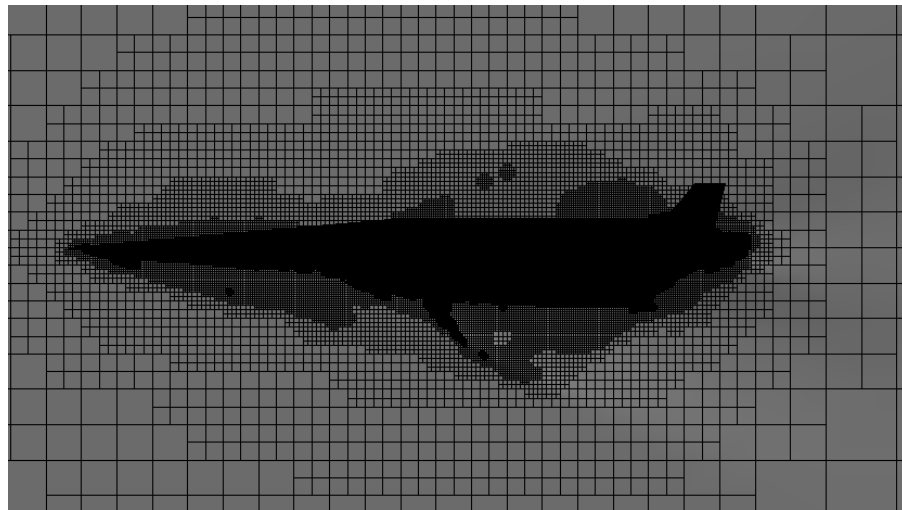


Figure B.1

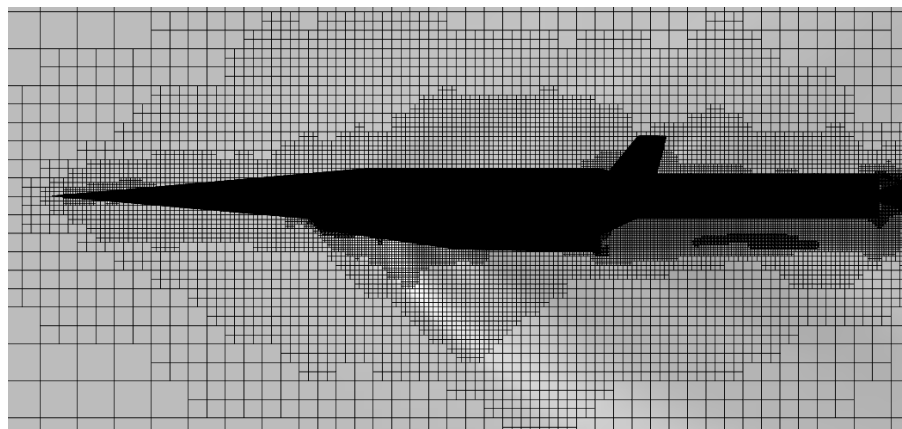


Figure B.2: Mesh generated by CART3D around the SPARTAN and first stage vehicles.

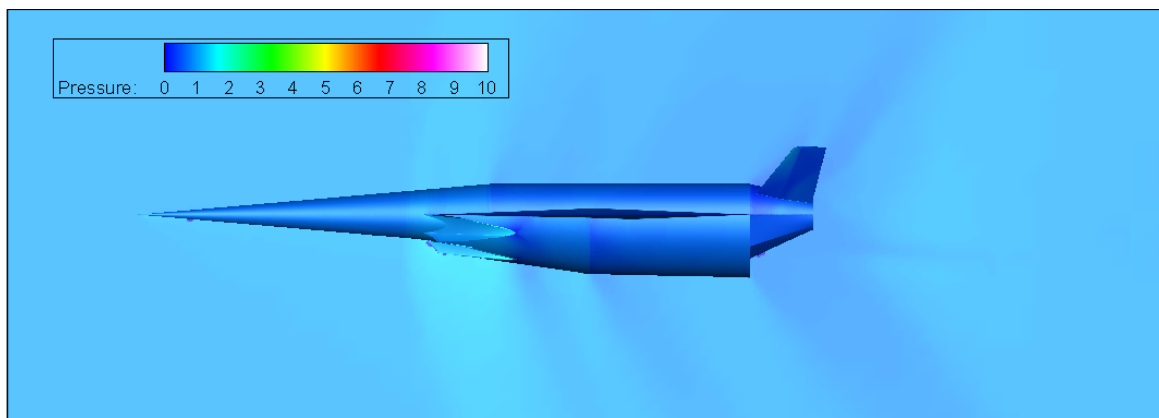


Figure B.3: CART3D flow result for the SPARTAN, at Mach 1.1,  $6^\circ$  angle of attack.

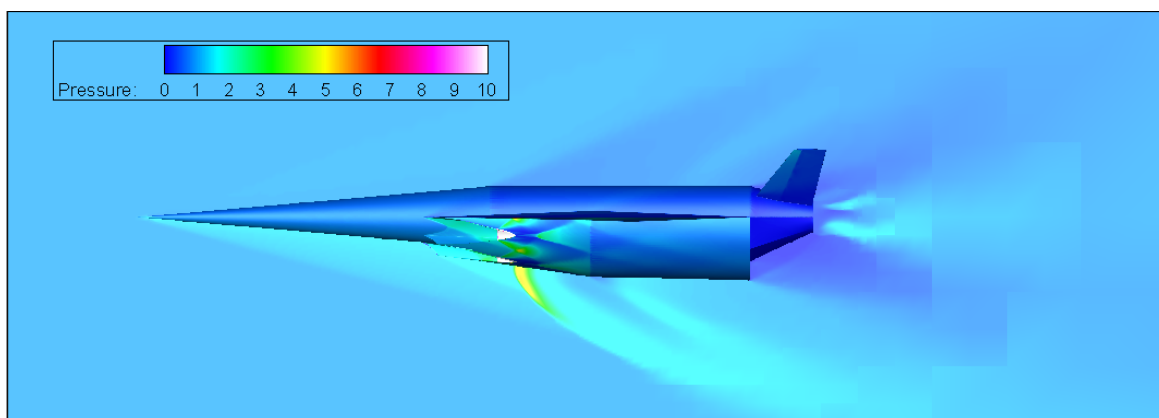


Figure B.4: CART3D flow result for the SPARTAN, at Mach 3,  $6^\circ$  angle of attack.